PE&RS

September 2022 Volume 88, Number 9

Photogrammetric Engineering & Remote Sensing The official journal for imaging and geospatial information science and technology

Landsat's Enduring Legacy

Pioneering Global Land Observations from Space

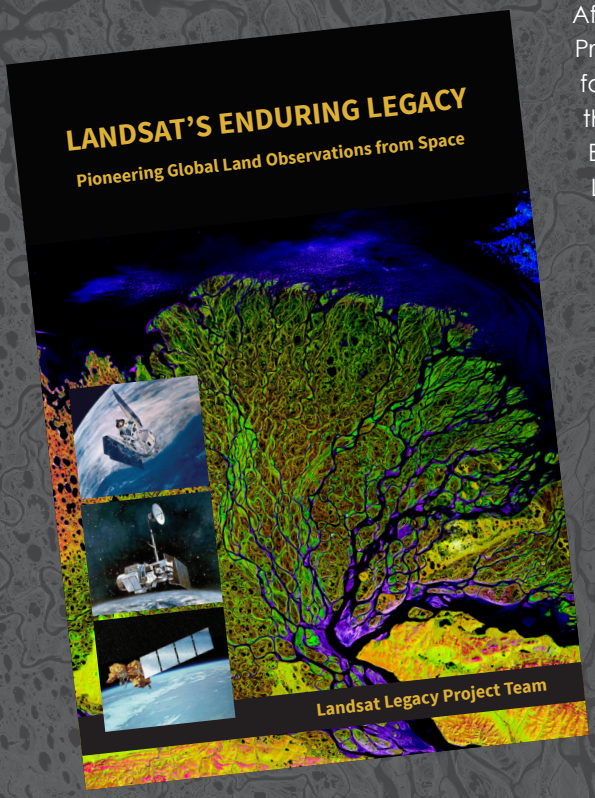

After more than 15 years of research and writing, the Landsat Legacy Project Team published, in collaboration with the American Society for Photogrammetry and Remote Sensing (ASPRS), a seminal work on the nearly half-century of monitoring the Earth's lands with Landsat. Born of technologies that evolved from the Second World War, Landsat not only pioneered global land monitoring but in the process drove innovation in digital imaging technologies and encouraged development of global imagery archives. Access to this imagery led to early breakthroughs in natural resources assessments, particularly for agriculture, forestry, and geology. The technical Landsat remote sensing revolution was not simple or straightforward. Early conflicts between civilian and defense satellite remote sensing users gave way to disagreements over whether the Landsat system should be a public service or a private enterprise. The failed attempts to privatize Landsat nearly led to its demise. Only the combined engagement of civilian and defense organizations ultimately saved this pioneer satellite land monitoring program. With the emergence of 21st century Earth system science research, the full value of the Landsat concept and its continuous 45-year global archive has been recognized and embraced. Discussion of Landsat's future continues but its heritage will not be forgotten.

The pioneering satellite system's vital history is captured in this notable volume on Landsat's Enduring Legacy.

Landsat Legacy Project Team

Samuel N. Goward
Darrel L. Williams
Terry Arvidson
Laura E. P. Rocchio
James R. Irons
Carol A. Russell
Shaida S. Johnston

Landsat's Enduring Legacy

Hardback. 2017, ISBN 1-57083-101-7

Student	$36*
Member	$48*
Non-member	$60*

* Plus shipping

Order online at

www.asprs.org/landsat

asprs THE IMAGING & GEOSPATIAL INFORMATION SOCIETY

To have your press release published in *PE&RS*, contact Rae Kelley, rkelley@asprs.org.

INDUSTRYNEWS

ANNOUNCEMENTS

URISA's Vanguard Cabinet is pleased to announce the results of the 2022 Student and Young Professional Digital Competition. Eligible participants were currently enrolled in a college or university, a recent graduate, or a young or emerging geospatial professional with fewer than five years of experience. The competition was limited to projects that utilize web and mobile platforms, such as ArcGIS Online, Tableau, Mapbox, or Power BI. Projects showcased the visualization functions of these platforms while also demonstrating knowledge and proficiency in spatial analytics, cartographic design, and/or geospatial techniques.

The five finalists selected to present and the titles of their presentations were as follows:

- Naomi Yates, USA/California, Shasta College: *"The California Water Crisis"*
- Ronney Phillips, University of North Texas, USA/Texas: *"Building a Low-Cost Air Quality Sensor Network"*
- Yashi Doshi, CEPT University, Gujarat, India: *"A Study Of Installing EV Charging Station In Gandhinagar"*
- Ishita Singh, CEPT University, Gujarat, India: *"Smart Urban Water Supply System"*
- Vinaya Thakur, CEPT University, Ahmedabad India: "Solar Power….Brightening Up Your World"

All presenters were awarded a complimentary one-year URISA membership.

The top three projects were presented by Naomi Yates, Ishita Singh, and Vinaya Thakur. These three individuals will receive a complimentary registration to GIS-Pro 2022 in Boise, Idaho; a $500 stipend for travel; and the opportunity to present their work live during the Lightning Talks session at the conference.

The full recording of the competition can be viewed at this link: https://youtu.be/bqxM_4WZRDw.

The Vanguard Cabinet appreciates the time, effort, and contribution to the geospatial field made by all competition participants. We enthusiastically look forward to following their careers!

The Vanguard Cabinet (VC) is an advisory board made up of passionate, young (35 years of age or younger) geospatial professionals who strive to engage young practitioners, increase their numbers in the organization, and better understand the concerns facing these future leaders of the geospatial community. The VC's mission is to collaborate with URISA's Board of Directors and URISA committees in creating and promoting programs and policies of benefit to young professionals and to enhance overall innovation, collaboration, networking, and professional development opportunities.

UP42 is collaborating with Trimble to offer automated Trimble® eCognition® software object-based image analysis and change detection solution. The unique, object-based image analysis technology within Trimble eCognition dramatically enhances the accuracy and quality of information extracted from geospatial data. This enables eCognition developers to become UP42 partners, create enriched processing capabilities, and commercialize their algorithms on the UP42 marketplace.

These extensive capabilities allow UP42 partners to extract accurate geospatial information for a wide range of applications, from forestry and land cover sustainability mapping to utility transmission vegetation management and temporal analysis.

"Collaborating with Trimble is a win-win scenario for UP42 and eCognition developers," said UP42 CEO Sean Wiid. "UP42 partners can leverage eCognition to create automated solutions that extract fully quantified insights from imagery—and then affordably scale them to commercial operations with our cloud infrastructure."

For current eCognition developers, Wiid explained, "UP42 makes available dozens of machine learning algorithms and a diverse selection of geospatial data on a single platform, where they can be integrated and exploited with flexible workflow capabilities. UP42 encourages these developers to take advantage of a new revenue channel by showcasing their analytics products on our marketplace."

"The addition of Trimble eCognition to the UP42 platform combines scalable infrastructure, Earth observation data and automated extraction technology to quickly transform data into valued information," said Tim Lemmon, Marketing Director for Trimble Geospatial.

For more information on accessing eCognition via UP42, please visit contact us at partnerships@up42.com.

EVENTS

Accessing and Analyzing Air Quality Data from Geostationary Satellites October 11, 18, & 25, 2022 10:00-12:00 EDT (UTC-4) This will be a three-part webinar series in partnership with the National Oceanic and Atmospheric Administration (NOAA) and the National Institute Of Environmental Research (NIER, South Korea) on air quality (AQ) data analysis from geostationary satellites. The webinar series will a) provide an overview of geostationary capabilities for monitor-

ing air quality around the world; b) introduce geostationary aerosol datasets from GOES-East, GOES-West, Himawari 8, and the Geostationary Environment Monitoring Spectrometer (GEMS); and 3) present data access and python tools to read and analyze the datasets. ARSET empowers the global community through remote sensing training. appliedsciences.nasa.gov/arset

Part 1: Geostationary AQ Observations and AQ Products from Himawari

- Introduction to air quality observations from geostationary satellites
- Differences and similarities between LEO and GEO observations
- GOES & Himawari true color images and loops - Worldview Exercise
- Tour of P-Tree visualization tool for Himawari-8 data
- Future AQ GEO missions
- Introduction to the Tropospheric Emissions: Monitoring of Pollution (TEMPO) Mission

Part 2: AQ Products from GOES

- Introduction to NOAA's GEO aerosol products - algorithms & validation
- Dataset details (files, frequency, parameters), access from NOAA's GOES-R archive on AWS S3
- Python Jupyter notebooks to read, map, and extract aerosol datasets
- Tour of NOAA Aerosol Watch website

Part 3: AQ Products from GEMS

- Introduction to the GEMS mission
- GEMS AQ datasets - algorithms & validation
- GEMS AQ data access
- Python Jupyter notebooks exercise to read, map, and analyze GEMS data

Visit appliedsciences.nasa.gov/arset for more information on this and other ARSET training events.

URISA, in partnership with the Northwest GIS User Group, is pleased to offer comprehensive pre-conference training and workshops during GIS-Pro 2022, taking place October 2-6, 2022. Consider these outstanding opportunities to learn on Sunday and Monday, October 2-3:

Sunday, October 2, 2022

NWGIS Training:

- Introduction to Python Programming (Half-Day)
- Taking Initiative with ArcGIS Hub (Half-Day)
- Getting Started with ArcGIS Arcade (Full-Day)
- Exploring ArcGIS Pro (Half-Day)
- Introduction to ArcGIS Pro Python Tools and Processes Development (Half-Day)

Monday, October 3, 2022

NWGIS Training:

- Introduction To Experience Builder (Half-Day)
- Getting Started with the ArcGIS API for Python (Half-Day)
- Getting Started with the ArcGIS API for javascript 4.x (Full-Day)
- ArcGIS Apps for the Field (Half-Day)
- Automating Map Production with Map Series and Python in ArcGIS Pro (Half-Day)

URISA Certified Workshops:

- Emergency Preparedness for GIS (Half-Day)
- An Overview of Open-Source GIS Software (Full-Day)
- Geospatial Maturity Models (Full-Day)
- GIS Program Management (Full-Day)
- Making Sense out of Social Indices (Full-Day)
- Preparing for GISP Certification (Full-Day)
- Building Community Using Geospatial Tools (Half-Day)

Take some time to learn more about subject matter experts who are instructing and the detailed learning outcomes for each workshop and course. One full-day or half-day URISA Certified Workshop is included with full conference registration. Some of the NWGIS training courses require an additional fee, which are significantly discounted from a normal stand-alone course. Detailed descriptions are posted in the online conference program here: https://gispro2022.sched.com/

Attendance at all courses and workshops, in addition to the conference, earns ample GISP Education Points.

CALENDAR

- 23 September, **ASPRS GeoByte — Allen Coral Atlas: A New Technology for Coral Reef Conservation.** For more information, visit https://www.asprs.org/geobytes.html.
- 2-6 October, **GIS-PRO 2022**, Boise, Idaho. For more information, visit https://www.urisa.org/gis-pro.
- 23-27 October, **Pecora 22**, Denver, Colorado. For more information, visit https://pecora22.org/.
- 31 October - 4 November, **URISA GIS Leadership Academy,** Santa Rosa, California. For more information, visit www.urisa.org/education-events/urisa-gis-leadership-academy/.
- 2-4 November, **AutoCarto 2022— Ethics in Mapping: Integrity, Inclusion, and Empathy**, Redlands, California. For more information, visit https://cartogis.org/autocarto/autocarto-2022/.

PE&RS
PHOTOGRAMMETRIC ENGINEERING & REMOTE SENSING
The official journal for imaging and geospatial information science and technology
September 2022 Volume 88 Number 9

COLUMNS

ANNOUNCEMENTS

DEPARTMENTS

See the Cover Description on Page 552

COVER DESCRIPTION

In satellite images of central Uzbekistan, a large circular cavity stands out amidst fields of sand and dusty plains. It is Muruntau gold mine, one of the world's largest sources of gold.

On July 22, 2022, the Operational Land Imager (OLI) on Landsat 8 acquired this natural-color image of the mine. Hundreds of trucks and a conveyer system are used to transport ore to nearby processing facilities. Workers then use a process called heap leaching to extract gold and other precious metals.

The mine taps into the Muruntau gold deposit, thought to be one of the largest single gold deposits on Earth. The deposit was discovered in 1958, and mining began in 1967. The pit is now 3.5 kilometers (1.8 miles) wide and 600 meters (2,000 feet) deep. In 2021, the mine produced as much as 3 million ounces (85,000 kilograms) of gold.

According to geologists, gold is near the surface in this area due to a chain of events that spanned many millions of years. Among them: the closure of an ancient ocean, a period of mountain building, intrusions of granite and water into key rock formations, and the onset of movement along nearby faults.

Astronomers are investigating how gold ended up on our planet in the first place. While nuclear fusion within the Sun can synthesize many elements, the process does not produce enough energy to create heavy elements like gold. Some astronomers think that collisions between neutron stars and supernova explosions may have provided that energy.

Any gold on the planet early in Earth's history would have sunk toward the core, but intense bombardment by meteorites about 4 billion years ago probably stirred things up and pushed small amounts of the metal into the mantle and toward the surface. By one estimate, gold makes up only 0.000004 percent of Earth's crust. About 80 percent of known gold reserves have already been mined.

To see the entire image, visit https://landsat.visibleearth.nasa.gov/view.php?id=150159.

NASA Earth Observatory image by Joshua Stevens, using Landsat data from the U.S. Geological Survey. Story by Adam Voiland.

asprs

THE IMAGING & GEOSPATIAL INFORMATION SOCIETY

PHOTOGRAMMETRIC ENGINEERING & REMOTE SENSING

JOURNAL STAFF

Publisher ASPRS
Editor-In-Chief Alper Yilmaz
Director of Publications Rae Kelley
Electronic Publications Manager/Graphic Artist
Matthew Austin

Photogrammetric Engineering & Remote Sensing is the official journal of the American Society for Photogrammetry and Remote Sensing. It is devoted to the exchange of ideas and information about the applications of photogrammetry, remote sensing, and geographic information systems. The technical activities of the Society are conducted through the following Technical Divisions: Geographic Information Systems, Photogrammetric Applications, Lidar, Primary Data Acquisition, Professional Practice, Remote Sensing Applications, and Unmanned Autonomous Systems Division. Additional information on the functioning of the Technical Divisions and the Society can be found in the Yearbook issue of *PE&RS*.

Correspondence relating to all business and editorial matters pertaining to this and other Society publications should be directed to the American Society for Photogrammetry and Remote Sensing, 8550 United Plaza Boulevard, Suite 1001, Baton Rouge, LA 70809, including inquiries, memberships, subscriptions, changes in address, manuscripts for publication, advertising, back issues, and publications. The telephone number of the Society Headquarters is 301-493-0290; the fax number is 225-408-4422; web address is www.asprs.org.

PE&RS. *PE&RS* (ISSN0099-1112) is published monthly by the American Society for Photogrammetry and Remote Sensing, 425 Barlow Place, Suite 210, Bethesda, Maryland 20814-2144. Periodicals postage paid at Bethesda, Maryland and at additional mailing offices.

SUBSCRIPTION. For the 2022 subscription year, ASPRS is offering two options to our *PE&RS* subscribers — an e-Subscription and the print edition. e-Subscribers can add printed copies to their subscriptions for a small additional charge. Print and Electronic subscriptions are on a calendar-year basis that runs from January through December. We recommend that customers who choose print and e-Subscription with print renew on a calendar-year basis.

The rate for a Print subscription for the USA is $1105.00 USD, for Canadian* is $1164.00 USD, and for Non-USA is $1235.00 USD.

The rate for e-Subscription (digital) Site License for the USA and Non-USA is $1040.00 USD and for Canadian* is $1089.00 USD.

The rate for e-Subscription (digital) plus Print for the USA is $1405.00 USD, for Canadian* is $1464.00 USD, and for Non-USA is $1435.00 USD.

*Note: e-Subscription, Print subscription, and e-Subscription plus Print for Canada includes 5% of the total amount for Canada's Goods and Services Tax (GST #135123065). **PLEASE NOTE: All Subscription Agencies receive a 20.00 USD discount.**

POSTMASTER. Send address changes to *PE&RS*, ASPRS Headquarters, 8550 United Plaza Boulevard, Suite 1001, Baton Rouge, LA 70809. CDN CPM #(40020812).

MEMBERSHIP. Membership is open to any person actively engaged in the practice of photogrammetry, photointerpretation, remote sensing and geographic information systems; or who by means of education or profession is interested in the application or development of these arts and sciences. Membership is for one year, with renewal based on the anniversary date of the month joined. Membership Dues include a 12-month electronic subscription to *PE&RS*. To receive a print copy of *PE&RS* there is an additional postage fee of $60.00 USD for U.S. shipping; $65.00 USD for Canadian shipping; or $75.00 USD for international shipping per year. Annual Individual Member dues for members residing in the U.S. and Other Foreign Members are $150.00 USD and $158.00 USD for Canadians. Annual Student Member dues for members residing in the U.S. are $50.00 USD; $53.00 USD for Canadian; and $60.00 USD for Other Foreign Members. A tax of 5% for Canada's Goods and Service Tax (GST #135123065) is applied to all members residing in Canada.

GIS Tips & Tricks

Al Karlin, Ph.D. CMS-L, GISP

Which Way is "Up"?

"Which way is up?" may sound like a really simple question to digital cartographers. Of course "up", in our typical American/European culture, on a map is "North". However, as was pointed out by Kelsey Leonard (Esri, ArcNews: Winter 2021), when the indigenous people around the Great Lakes made their highly detailed maps, "up" was the direction that the sun rose; East to us digital map makers! Then even when "up" is "North", the question arises… which North? We frequently forget that North has three separate and distinct meanings and directions.

1. Celestial North (aka "True North"): The north (and south) celestial pole(s) is/are the **(two) point(s) in the sky** where Earth's axis of rotation, indefinitely extended, intersects the celestial sphere. That is, North is defined by the extension of the Earth's axis of rotation. These points shift with the "wobble" or axial precession of the Earth's spin axis every 26,000 years,

2. Magnetic North (aka "Compass North"): This is a **point on the surface** of the Earth's Northern Hemisphere at which the planet's magnetic field points vertically downward. This point is constantly "wandering" as the Earth's rotation and core move, and

3. Grid North: This "North" refers to a navigational (survey) term describing the **direction northwards along the "grid lines" of a map projection** (a whole other topic). This "North" is neither Celestial North nor Magnetic North, but may align with either or neither.

In most GIS Programs (Esri, GlobalMapper, QGIS) the North Arrow is connected to the map layout. If the map layout is rotated, the arrow follows. ***TIP***: Did you know that you can rotate the entire layout? In an ArcGIS Pro Layout Window, all you need to do is click on any of the handles, move off it a little bit to see the rotate icon and move the entire dataframe. In a Map Window, it is even easier, simply use the "a" key to rotate the frame clockwise, and the "d" key to rotate it counter-clockwise.

Inserting a North Arrow is a fairly simple and straightforward task in GIS mapping programs. It usually just involves finding the Insert North Arrow icon, selecting your favorite arrow (or rosette) from a dropdown choice or list, then resizing/repositioning the selected style and you're done! Or are you? Which "North" is it when you put a "North Arrow" onto a map?

Here is an example in ArcGIS Pro (v2.92) on how to control and specify the North Arrow.

Step 1. Insert a North Arrow: From the Insert Tab on the Ribbon select New North Arrow

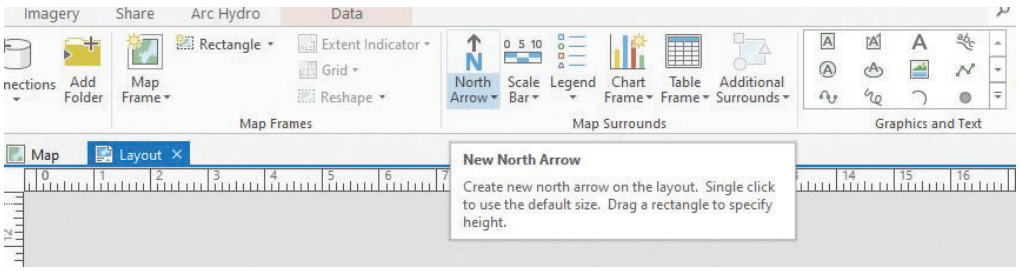

Figure 1. The Project Tab on the Ribbon when a Layout is active.

Step 2. Select the style from the dropdown choices, click and drag/size a box on the layout for the arrow. Using the graphic handles on the display box, move/resize the North Arrow as needed.

Now comes the fun part…

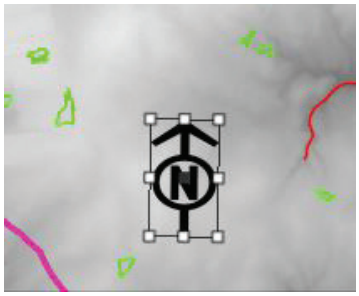

Figure 2. A North Arrow showing graphic handles as displayed after selected from the optional arrows and the graphic box was dragged on the Layout.

Photogrammetric Engineering & Remote Sensing
Vol. 88, No. 9, September 2022, pp. 553-554.
0099-1112/22/553-554

doi: 10.14358/PERS.88.9.553

Step 3. With the North Arrow selected, on the North Arrow Tab on the Ribbon (which you will see once you inset a North Arrow), select the "Design" tab:

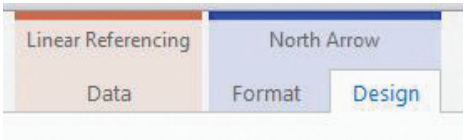

Figure 3. The Design Tab on the North Arrow Tab appears when the North Arrow is selected.

Step 4. On the Design Tab, select the "North" that you want for your map. The Default is Celestial (True) North with a Calibration Angle of "0". Remember… never just accept the defaults without knowing what it is.

Figure 4. The North Arrow Design tab showing the user-selected options.

The dropdown arrow (next to True North) will let you select Magnetic (as below) and/or Map (Grid North) and calculates a calibration angle, that in the case of Magnetic North shows the magnetic declination (deviation) from Celestial (True) North, and you will see the North Arrow rotate to that position, in this case, -7.03 degrees (counterclockwise) from "up".

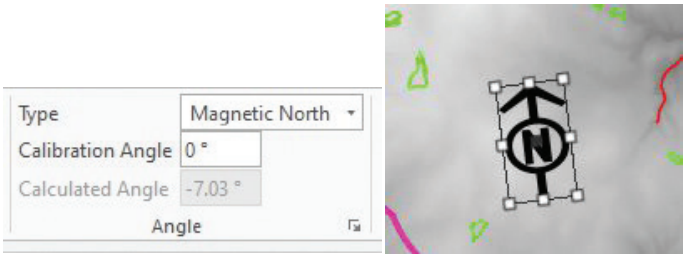

Figure 5. The North Arrow Design Tab after selecting "Magnetic North" and the results showing the rotated North Arrow.

Note: The Calculated Angle value shows the rotation angle of the north arrow based on the orientation and calibration angles. This value cannot be edited by the user.

Of course, if you change the North Arrow to Magnetic North (or Grid North), you should put a note on the map that "North" is Magnetic (or Grid) North), as well as, indicating that declination angle.

There are multiple ways that you can indicate north on your maps, but it is always a good idea to tell your users which North you are displaying on the map and which way is "up".

Send your questions, comments, and tips to GISTT@ASPRS.org.

Al Karlin, Ph.D., CMS-L, GISP is with Dewberry's Geospatial and Technology Services group in Tampa, FL. As a senior geospatial scientist, Al works with all aspects of Lidar, remote sensing, photogrammetry, and GIS-related projects. He also teaches beginning map making at the University of Tampa.

Grids & Datums

BURKINA FASO

BY Clifford J. Mugnier, CP, CMS, FASPRS

The Grids & Datums column has completed an exploration of every country on the Earth. For those who did not get to enjoy this world tour the first time, *PE&RS* is reprinting prior articles from the column. This month's article on Burkina Faso was originally printed in 2005 but contains updates to their coordinate system since then.

During the early part of the 15th century, the Mossi horsemen of Ghana invaded the area and established a long-lived empire. The Mossi maintained a cavalry that successfully defended its West African territory from hostile Muslim neighbors, and as a result the former Upper Volta is not predominately Muslim. The French came to the area in the late 19th century, established a protectorate (1895-1897), and later partitioned former areas of the empire to Mali, Niger and Côte d'Ivoire. Local natives of Upper Volta were "blackbirded" to work on the French plantations of Côte d'Ivoire in the south. For approximately 60 years, the French favored the Côte d'Ivoire at the expense of Upper Volta. Independence from France came in 1960, and a military coup in 1966 was the first of two decades of coups that culminated in Captain Thomas Sankara taking control and changing the name of the country to Burkina Faso which means "country of the incorruptibles" (Lonely Planet, www.lonelyplanet.com).

Landlocked Burkina Faso is bordered by Benin (306 km), Ghana (548 km), Côte d'Ivoire (584 km), Mali (1,000 km), Niger (628), and Togo (126 km). Slightly larger than Colorado, the lowest point is the Mouhoun (Black Volta) River (200 m), and the highest point is Tena Kourou (749 m). The terrain is mostly flat to dissected, undulating plains with hills in the west and southeast (*CIA Factbook*). The major cities are the capital Ouagadougou (Ouaga), and Bobo-Dioulasso.

The French *Institut Géographique National* (IGN) had the initial mapping and geodetic responsibility, and shared that with the *Annexe de l'Institut Géographique National á Dakar* when the federation of the eight territories constituting French West Africa came into being in 1904. At

the time, the IGN Annex, Dakar was known as the *Service Géographique de l'Afrique Occidentale Française* – SGAOF. The IGN later established a network of 200 "Astro" stations (astronomic positions) after 1950 that initially served as the basic control of French West Africa at the scale of 1:100,000 for Burkina Faso. The reference ellipsoid was the Clarke 1880 (IGN) where: a = 6,378,249.2 m, b = 6,356,515.0 m, and computed $^1/_f = 293.4660208$, the projection and grid is the Universal Transverse Mercator (UTM). These compilations were also used to make maps at smaller scales. Earlier mapping of portions of Burkina Faso were compiled by SGAOF from 1923 at a scale of 1:200,000, entitled C*arte de l'Afrique de l'Ouest au 200.000e*. Pre-1952 sheets were compiled from ground surveys or trimetrogon photography; remaining sheets from aerial photography and astronomic control. Final sheets were checked and contoured in the field. Relief

Photogrammetric Engineering & Remote Sensing
Vol. 88, No. 9, September 2022, pp. 555-556.
0099-1112/22/555-556

doi: 10.14358/PERS.88.9.556

was indicated by contours at 40- or 50-meter intervals with some supplementary relief portrayed by escarpment, cliff, rock outcrop, sand, and sand dune symbols. Post-1952 sheets were cast on the UTM Grid, Zones 30 and 31 (*U.S. Army TM-5-248, Foreign Maps*). In 1950, the SGAOF performed the classical triangulation of the capital city, Ouagadougou.

In 1958, the French IGN and the SGAOF established 54 stations throughout the country by classical triangulation. In 1960, IGN and the U.S. Army Map Service established 46 stations along the 12th parallel. This triangulation throughout Africa was along the 12th parallel and it started at the origin of the Blue Nile Datum of 1958 in Egypt, at station Adindan where: $\Phi_o = 22^o\ 10'\ 07.1098''$ N and $\Lambda_o = 31^o\ 29'\ 21.6079''$ East of Greenwich, deflection of the vertical: $\xi = +2.38''$, $\eta = -2.51''$. As I stated in my column on Ethiopia (*PE&RS, March 2003*), "Adindan" is the name of the origin point and it is **not** the name of the datum; an almost universal mistake found in reference works including the DMA/NIMA/NGA *TR 8350.2*.

In 1979, a Doppler satellite survey was undertaken throughout Africa and included the observation of 16 stations in Burkina Faso. The survey was defined on the WGS72 Datum and final results were computed on the Clarke 1880 ellipsoid for collocated points of the 1958 network of stations in Ouagadougou, apparently on the Blue Nile Datum of 1958. In 1997, 55 points were observed with GPS receivers by the *Institut Géographique du Burkina* (IGB) in cooperation with the government of Switzerland. Since 1998, this first-order network of GPS observations has been densified with 217 additional points in the southwestern part of Burkina Faso. Thanks go to Alain Bagre in his report to the FIG for the details of the geodetic history of his country.

The NGA lists transformation parameters for the Blue Nile Datum of 1958 (Adindan) to WGS84 Datum based on a *single point* as: $\Delta a = -112.145$ m, $\Delta f \times 10^4 = -0.54750714$, $\Delta X = -118$ m ± 25 m, $\Delta Y = -14$ m ± 25 m, and $\Delta Z = +218$ m ± 25 m.

Burkina Faso Update

"Three weeks (GPS weeks 1653 to 1655, September 11 to October 1, 2011) of Burkina Faso CORS GPS and Glonass data have been processed together with 52 surrounding IGS stations by means of the Bernese GPS Software (version 5.0). The purpose is the determination of ITRF2008 coordinates for the nine Burkina Faso CORS. The average accuracy within ITRF2008 at observation epoch for the whole network is estimated to be 5 mm in North, 6.3 mm in East, and about 12 mm in Up component. The Burkina Faso CORS network has a slightly better accuracy of approximately 5-6 mm in both horizontal components and around 11 mm in up component. The internal accuracy of the Burkina Faso CORS network is 2-3 mm in horizontal components and around 5 mm in up component."

https://www.academia.edu/4874865/ESTABLISHING_A_LAND_POLICY_REFORM_AND_GPS_TECHNOLOGY_IMPLEMENTATION_IN_BURKINA_FASO

In 2014, Aero Ashai Corporation completed a photogrammetric mapping project in the northern area of Burkina Faso (Digital Topographic Mapping Project in Burkina Faso).

https://openjicareport.jica.go.jp

The contents of this column reflect the views of the author, who is responsible for the facts and accuracy of the data presented herein. The contents do not necessarily reflect the official views or policies of the American Society for Photogrammetry and Remote Sensing and/or the Louisiana State University Center for GeoInformatics (C^{4}G).

This column was previously published in *PE&RS*.

AN INTERVIEW WITH THE 2022-2023 ASPRS PRESIDENT

Recently we interviewed the current ASPRS president, Dr. Chris Parrish, about his experience in ASPRS and how our professional society contributes towards molding students' career pathways. For the past eight years, Dr. Parrish works as an associate professor at Oregon State University. Previously, he served in the Remote Sensing Division of NOAA's National Geodetic Survey (NGS). He is the 2022-2023 ASPRS President. He is also a dad to a fall 2021 U.S. Senate Page, Katherine Parrish and enjoys variety of outdoor activities.

In this interview we asked about his current position and experience gained by being a member with ASPRS, as well as current challenges and the future of ASPRS. With a hope that students will gain directions for knowledgeable action, the interview responses are compiled below.

"A to B" Annual Conference to Board President

When asked about his first involvement with ASPRS, Dr. Parrish mentioned that he attended his first ASPRS Annual Conference in 2000 in Washington, D.C., and had the opportunity to meet and interact with a number of leaders in photogrammetry and remote sensing. He was interested in airborne lidar at that time, and, while those early lidar systems were very primitive compared to what we have today, he remembers being astonished by the speed at which high-accuracy topographic data could be collected. During his time at the ASPRS conference he was welcomed as family, and as a result he joined ASPRS right after the conference.

Around that time, he had a meeting with the Director of NGS and shared his goals of carrying out cutting-edge research in the field of airborne lidar. Although it took nearly a decade, during this time he completed graduate programs at the University of Florida and the University of Wisconsin and gained experience in NGS's Remote Sensing Division, he was eventually able to achieve those goals. He also became increasingly active in ASPRS, serving on the Potomac Region Board and helping organize the Potomac Region's annual GeoTech Conference.

Fast forward to 2014, he joined the faculty of Oregon State University and continued his active involvement in ASPRS. He served as Lidar Division Director from 2014-2016 and was elected Vice President in 2020. The way ASPRS elected officer positions work, the newly-elected VP automatically advances to the position of President-Elect after one year and then President the following year. He stepped into the position of ASPRS President at the ASPRS Annual Conference in Denver in February of this year.

Growth through ASPRS

Dr. Parrish also briefly discussed the role of ASPRS in his professional and personal life. He states that the greatest benefit of being an active member of ASPRS is developing a broad network of professional contacts, extending across government, academia, and industry. He has also benefited from attending outstanding technical presentations and panel discussions at our conferences and asking questions of the presenters and panelists. He shared that, at the current stage of his career, he is more interested in giving back to the society and profession than in personal benefit from his membership and finds it especially rewarding to work with groups such as the Student Advisory Council (SAC) and Early Career Professionals Council (ECPC).

Chris teaching a differential leveling lab in an undergraduate surveying class at Oregon State University.

Common Misconceptions

We wanted to know about his opinion on common misconceptions about volunteer positions at ASPRS and how can these misconceptions be addressed. Dr. Parrish responded by stating that a common misconception is that people often feel they need to wait until they have advanced to a certain stage in their career before running for office or holding a position in ASPRS. This is simply not true. He noted that there are many ways to get involved at any stage in your career, including while still a student. One fairly typical path in ASPRS—although by no means the only one—is to get started by volunteering at conferences and serving as an officer in a student chapter. Then become active in your Region and in the Early Career Professionals Council (ECPC), and then seek opportunities to become involved in ASPRS at the National level.

"...the greatest benefit of being an active member of ASPRS is developing a broad network of professional contacts, extending across government, academia, and industry."

I am Proud of

We asked Dr. Parrish about the accomplishments he is most proud of and he talked about working on new student chapters with Student Advisory Council (SAC). An especially meaningful effort over the past few months has been working with SAC Chair, Lauren McKinney-Wise, on streamlining the procedures for creating new student chapters. His hope is that by facilitating new student chapters, we will be able to introduce many more students from across a broad range of academic institutions to geospatial professions and also help ensure the future success of ASPRS and our field. The recently-formed ASPRS Diversity, Equity, and Inclusion (DEI) Committee, led by Amanda Aragón and Anne Hillyer, is another priority, and he is very glad to see the great momentum of this new committee. Additionally, he notes that our monthly ASPRS Brainstorming-to-action (BAM!) meetings have been a lot of fun, and he is very grateful for all the suggestions that have been put forward for new ASPRS initiatives!


Chris leading a UAS in Transportation Workshop hosted at OSU and sponsored by PacTrans.

Chris with his daughter Katherine on the Oregon coast north of Lincoln City.

Evolution and Future Path

It was important to talk about the evolution within ASPRS and the direction of the professional society and field. Dr. Parrish's response provided assurance that ASPRS has been evolving based on the needs of our field. Today, geospatial data is used in an ever-increasing number of applications, from autonomous cars to computer animation to accident site reconstruction, in addition to a wide range of scientific disciplines. Additionally, new technologies, such as UAS and lidar-equipped smartphones have led to a democratization of geospatial data collection. The increasing use of machine learning and artificial intelligence also opens up many new geospatial application areas. His hope is that, led by the SAC and ECPC, ASPRS will continue to broaden our membership and the range of disciplines we support, while also helping new members benefit from our standards, guidelines, and best practices.

"...by facilitating new student chapters, we will be able to introduce many more students from across a broad range of academic institutions to geospatial professions and also help ensure the future success of ASPRS and our field."

My Inspiration

When asked about his inspiration he mentioned Bobbi Lenczowski. Bobbi's career accomplishments are too numerous to list, but she served as the ASPRS President from 2012-2013, is an ASPRS Fellow, former Executive Director of AmericaView, a recipient of the President's Award for Distinguished Federal Civilian Service, and is very active in K-12 education outreach. What is especially impressive to him is how many current leaders in remote sensing and across the geospatial professions list Bobbi as a mentor and role model: "it's sort of a Who's Who list of our field!"

If Students want to get Involved…

Dr. Parrish mentioned that ASPRS has recently started using the Higher Logic community management platform (https://community.asprs.org/home), and many volunteer opportunities will start to be advertised through Higher Logic Community Boards. He also suggested to reach out to ASPRS Division Directors, Council Chairs, Working Group Chairs, and Board officers to ask about opportunities to get involved.

The entire team of ASPRS SAC expresses their gratitude to Dr. Parrish for taking out time for this interview from his busy schedule. We learned a lot from his responses, and we hope this will be informative for our readers as well.

JOIN US IN WELCOMING ASPRS' NEWEST SUSTAINING MEMBER, NEARMAP!

NEARMAP

10897 S River Front Parkway
Suite 150
South Jordan, Utah 84095
www.nearmap.com/us/en

"As Nearmap continues to grow and expand in the Public sector, embarking on a relationship with ASPRS just made sense", said Shelly Carroll, General Manager of the Government vertical at Nearmap. "We're looking forward to bringing our high resolution aerial imagery and data intelligence to the members of ASPRS and the broader Government community—knowing that our world-leading capabilities and cost-effective solutions are helping to support a multitude of critical services."

Nearmap provides easy, instant access to high resolution aerial imagery, city-scale 3D content, AI data sets, and geospatial tools. Using its own patented camera systems and processing software, Nearmap captures wide-scale urban areas in the United States, Canada, Australia, and New Zealand several times each year, making current content instantly available in the cloud via web app or API integration. Every day, Nearmap helps thousands of users conduct virtual site visits for deep, data-driven insights—enabling informed decisions, streamlined operations and better financial performance. Founded in Australia in 2007, Nearmap is one of the largest aerial survey companies in the world and is publicly listed on the Australian Securities Exchange (ASX:NEA).

NEW ASPRS MEMBERS

ASPRS would like to welcome the following new members!

Conor MacBain Church
Chazz Coleman
James Richard Charles Dalton
Jerry Goodwin
Victor King
Su Leone
Andrew Molchan
Kris Nehmer, PLS
Matthew Noland
Kevin Schmalz
Bechu Kumar Vinwar Yadav, Ph.D.

FOR MORE INFORMATION ON ASPRS MEMBERSHIP, VISIT
HTTP://WWW.ASPRS.ORG/JOIN-NOW

ASPRS ANNOUNCES NEW SECTOR INSIGHT EDITORIAL TEAM!

ASPRS is pleased to announce SectorInsight's new editorial team, Youssef O. Kaddoura, Bob Ryerson, and Hamdy Elsayed.

Youssef O. Kaddoura Ph.D. is the Academic Program Specialist II in the Fort Lauderdale Research and Education Center at the University of Florida (UF). He graduated from the University of Florida with a doctoral degree in Geomatics Science. His research investigates establishing a reproducible methodology to georeference oblique tower-mounted (PhenoCam) images, through applying a multidisciplinary approach that encompasses the fields of photogrammetry, ecology, lidar, conventional surveying techniques and theories. As a member of ASPRS, he served as a Board Member for the period of March 2020 till March 2021. He holds a MS in Computer Engineering from the University of Florida, which included deploying innovative use of technology towards enabling aging seniors to live independently for a longer period of time. This work resulted in a US Patent titled "Remote surveillance and assisted care using a mobile communication device", which served as a catalyst to further pursue remote sensing and photogrammetry. Previously, Youssef worked at Geospatial Consultancy Company, an ESRI partner in Abu Dhabi, United Arab Emirates.

Dr. Bob Ryerson, FASPRS, has been a senior scientist in government and has held senior executive positions in industry and government. His interests are in environmental and natural resource applications of earth observation and the economic benefits of geospatial information to society, with special reference to poverty reduction in developing countries through achievement of sustainable development goals. He has also made contributions to education in Canada, the USA, Australia and India where he has been an adjunct professor and served on various advisory and thesis committees.

Bob is a Fellow of ASPRS and has served as the Director of the Remote Sensing Applications Division of the ASPRS. He is also a Past-President of the Canadian Remote Sensing Society. He has served on the Boards of a number of companies and an industry association as well as on the EO Program Board of ESA. He has worked in more than forty countries in Asia, South America, Africa, Europe and the Pacific.

Bob has won the Canadian Remote Sensing Society's Gold Medal, the Alan Gordon Memorial Award from the ASPRS for Outstanding Service over his career to Remote Sensing, the Roger F. Tomlinson Life-time Achievement Award in 2020 and awards for outstanding contributions to the Public Service of Canada. Several examples of his scientific work have been featured in Canada's National Museum of Science and Technology.

Hamdy Elsayed is a Research Scientist in Lidar Systems at Teledyne Geospatial and Ph.D. Candidate, Researcher, and Teaching Assistant, in Geomatics Engineering at Toronto Metropolitan University (TMU, formerly Ryerson University). Hamdy has been serving as a member of the board of directors of the Canadian Remote Sensing Society since 2020, where he led and chaired several vital initiatives related to student engagement with the industry and building the student and young professional capacity to meet the market job requirements. Also, he served as a TMU Academic Senate member and a Professional Career Mentor.

Academically, Hamdy has a Bachelor of Science (w/Honor) in Electrical Engineering (2006) from Alexandria University and a Master of Science (w/Distinction) in Information Technology Management (2015) from the British University in Dubai. Additionally, he is a certified PMI Project Management Professional and an Advanced-Operations Remotely Piloted Aircraft System (RPAS) Pilot.

Hamdy has over 16 years of international experience leading and managing geomatics, remote sensing, and geospatial engineering projects in governmental and private institutions in North America, Africa, and the Middle East. Hamdy's expertise covers Sensor Integration, aerial photography, lidar scanning, Indoor mapping, digital imaging, GNSS and inertial navigations, and depth sensing technologies. Hamdy was also awarded Mitacs Accelerated fund in 2018 to work on a research project with Teledyne and the Canadian Space Agency to build a new generation of space lidar scanning system. Additionally, he was awarded Cansel Business Award in 2021 and the best research presentation in the Canadian Symposium on remote sensing in 2020.

The SectorInsight Column is a general interest column related to education and professional development in the geospatial community. From the inception of ASPRS, the membership has been a balance of individuals, companies, and institutions from three primary sectors: private industry, government, and academia. SectorInsight seeks to highlight the interaction and importance of this balance. For more information on SectorInsight or *PE&RS*, please contact sectorinsight@asprs.org.

Impact of Spatial Configuration of Urban Green Space and Urban Impervious Surface on Land Surface Temperature: A Multi-Grid Perspective

Ya Zhang, Zhenfeng Shao, Xiao Huang, Xiaoxiao Feng, Zifan Zhou, and Yong Li

Abstract

Urbanization process has a huge impact on vegetation dynamics in urban ecosystems. Ecosystem services provided by urban green space have been increasingly incorporated into city-level measures to address climate change. Understanding the relationship between urban green space (UGS) and urban impervious surface (UIS) as well as land surface temperature (LST) is crucial to the understanding of urban spatial morphology. To better understand the impact of different spatial configurations on the urban heat island effect at different scales, this study constructed the spatial configuration of UIS and UGS on four grids of different scales and explored their relationship with LST in seasonal changes. The results show that different indicators present significant characteristic disparity under the four grid scales, compared with other scales, indicators have a relative stability correlation at 1 km. In addition, trees and grass, as different urban green spaces, have notable negative effects on surface temperature. At grid 3 (G3) scale, grassland had a strong correlation with LST in aggregation index and landscape shape index, which were 0.473 and 0.648, suggesting that fine-scale planning is of great significance to alleviating the urban heat island effect. This study can assist in designing sustainable cities by providing insights into urban green space planning and management.

Introduction

Urban ecosystem is an essential component of the terrestrial ecosystem, with a suite of services that include carbon sequestration, air quality improvement, storm-water attenuation, and energy conservation (Xu *et al.* 2020; Trlica *et al.* 2020). The progress of urbanization is speeding up, and the transformation between different types of land use has brought a huge impact on the environment (Zhuang *et al.* 2022; Shao *et al.* 2020). At the same time, it also modifies the growth pattern of vegetation, making it different from that in the rural. The notable changes in the underlying surface of the city, especially the increase in impervious surface, have led to many problems, such as the urban heat island effect (Jung *et al.* 2021; Shao *et al.* 2019). The change of impervious surface can fundamentally modify the redistribution of precipitation, thereby affecting the urban hydrological environment. The boost of urban population results in an increase in buildings, pavements, and roads while reducing green spaces and waterbody. The contradiction between urban development and urban ecology exists in a dynamic manner. Urban green space (UGS) serves as a main natural factor in the city, playing an important role in the cooling effect of a city (Bowler *et al.* 2010). The ecological effect of urban vegetation can alleviate many negative effects resulting from the urbanization process.

Ya Zhang, Zhenfeng Shao, Xiaoxiao Feng, Zifan Zhou, and Yong Li are with the State Key Laboratory of Information Engineering in Surveying, Mapping and Remote Sensing, Wuhan University, 129 Luoyu Road, Wuhan 430079, China (shaozhenfeng@whu.edu.cn).

Xiao Huang is with the Department of Geosciences, University of Arkansas, Fayetteville, Arkansas 72701.

Contributed by Alper Yilmaz, June 7, 2021 (sent for review October 25, 2021; reviewed by Ji Zhou, Arnaud Le Bris, Davood Akbarl, Yujin Park).

Although the development of cities has brought great convenience to people's life and production, it also has an immeasurable impact on various natural resources and the ecological environment. Urbanization demands a rational use of urban land resources and the construction of sustainable development of the ecological environment. The coverage of UGS is an important indicator of natural elements on the surface, as well as a manifestation of urban ecological civilization (Zhang and Shao 2021). With rapid urbanization and changes in the environment, the distribution of urban green space and its functions are highly valued (Qian *et al.* 2019; Hu *et al.* 2021). In the process of urbanization, attention needs to be paid to realize the sustainable development of urban and to design and build a more balanced urban ecological structure (Song *et al.* 2021).

Changes in land cover composition are a key consequence of urbanization, often increasing land surface temperature (LST). Thus, it is necessary to extract the distribution of UGS and monitor its dynamics connection with the spatial structure of urban impervious surface (UIS) to minimize the impact of urban construction on the ecological environment, aiming to support sustainable urban development. Zheng *et al.* (2014) used a land cover map derived from high-resolution satellite data and ASTER LST data to investigate the effects of composition and spatial pattern of anthropogenic land cover characteristics on LST in Phoenix, Arizona. The results showed that random patterns on the paved surface increased nighttime LST compared to scattered. However, the warming effect was more pronounced when the paved surface was highly clustered. To monitor the spatial configuration in sampling units of different sizes, Zhou *et al.* (2017) conducted a comparative study on two cities with different climatic conditions, using various statistical methods to quantify and compare the relationship between tree and LST. When the analysis unit is relatively small, the spatial autocorrelation may affect the relationship between the landscape indicators with LST, especially as the size of the analysis unit increases, the relationship between the spatial configuration measurement and LST becomes stronger. Masoudi *et al.* (2021) evaluated the relationship between UGS patterns and UGS cooling effects under land use influence in 2005 and 2015. The results showed that over time, the size of land use increased and vegetation disappeared, resulting in an increase in LST. That is, land use not only affects the composition of UGS, but also affects their configuration and cooling effect.

Existing studies in urban ecological evaluation are generally conducted from the perspective of landscape patterns. In landscape pattern analysis, the choice of spatial scale in a landscape is an important factor (Plowright *et al.* 2017; Yang *et al.* 2020; Xu *et al.* 2020). Studies have shown that the relationship differs at different scales between the types of urban land use and land surface temperature (Liu *et al.* 2021; Chen *et al.* 2020). Considering contributions from different types of features in land use classification, Zhang *et al.* (2020) used landscape-level indicators based on area-weighted average to construct landscape

Photogrammetric Engineering & Remote Sensing
Vol. 88, No. 9, September 2022, pp. 563–572.
0099-1112/22/563–572

doi: 10.14358/PERS.21-00034R3

pattern, which improved the classification accuracy of urban land use and demonstrated the impact of landscape pattern on urban land use is greater than building function. Xing and Meng (2020) proposed a novel framework to measure urban landscapes and classify urban functions by quantifying multiple urban landscape elements and their interaction with spatial metrics. The evaluation index from local analysis and analysis of variance proves the adequacy and effectiveness of this method in the classification of urban functions. At the same time, a conditional reasoning random forest method is proposed to establish an automatic city function classification model with spatial measurement. There exists a certain correlation between vegetation carbon storage and the regional environment (Godwin *et al.* 2015). Ren *et al.* (2013) focused on the relationship between landscape heterogeneity and carbon density. Ren's results reveal the quantitative relationship between landscape and vegetation carbon storage at different scales in the development process of Xiamen. At present, however, a standard measurement is lacking to evaluate urban greening functions. Existing indicators tend to overestimate or ignore the typical landscape features that can benefit the evaluation of the ecological functions of urban green space.

In practical applications, multiple land use land cover data sources need to be considered when classifying and mapping urban land use categories. Zhou and Cao (2020) quantified the spatial pattern of forestland in Shanghai at four spatial scales and discussed the relationship between land surface temperature and forestland spatial pattern and seasonal change. The results show that the change of spatial scale has significant influence on the relationship between spatial pattern and LST. Kabisch and Haase (2013) used CORINE 1990, 2000, and 2006 land cover data and city boundaries to analyze 202 European cities, assessing the availability of these data sets by introducing changes in urban green space supply between 1990–2000 and 2000–2006. Nowak and Greenfield (2012) investigated the changes in trees and impervious cover in selected cities in the US using a simple and reproducible measurement with aerial photos provided by Google image and the tree cover. This method determines that the direction and rate of changes in urban trees and impervious cover assist cities in maintaining the required level of tree cover and related ecosystem services. Plowright *et al.* (2017) used the fusion results of multiple data sources to discuss the relationship between impervious surface and tree height at a single wood scale and landscape scale.

In this paper, we conduct a multi-level grid analysis on the landscape pattern of land cover, taking Nantong as a study area (details in the section "Study Area"). Based on the generated multi-level grid, Nantong is divided into multiple blocks. Land surface temperature (LST) of the three seasons of the corresponding year is calculated, and the landscape pattern indicators are used to quantitatively analyze the pattern of the study area. We analyze the spatial pattern of urban land cover based on a multi-level grid and discuss the influence of UGS, UIS, and LST. The main objectives of this research are to (1) compare optimal grid scales based on multi-level grid analysis of urban landscape patterns; and (2) to explore the correlation among UGS, UIS, and LST at different grid scales.

Material and Method

Study Area

Nantong, in the alluvial plain of the lower Yangtze River, is located at 31°41′06″–32°42′44″ N and 120°11′47″–121°54′33″ E. The maximum distance from north to south is 114.2 km, and the maximum distance from east to west is 158.8 km. Nantong belongs to the northern subtropical humid climate zone, with the notable influence of monsoon, four distinct seasons, mild climate, abundant rain, and a long frost-free period. The annual average near surface air temperature is 15.1°C, and the annual precipitation is about 1040 mm. This study selects the urban core area of Nantong, which mainly includes three parts: Chongchuan District (1), Gangzha District (2), and Development District (3). Multispectral data of Sentinel-2 is displayed as a base map; the specific location of the study area is shown in Figure 1.

Data Processing

Remote Sensing Data

In order to estimate the impact of the spatial distribution of UGS and UIS on UHI, three phases of *Landsat 8* Operational Land Imager

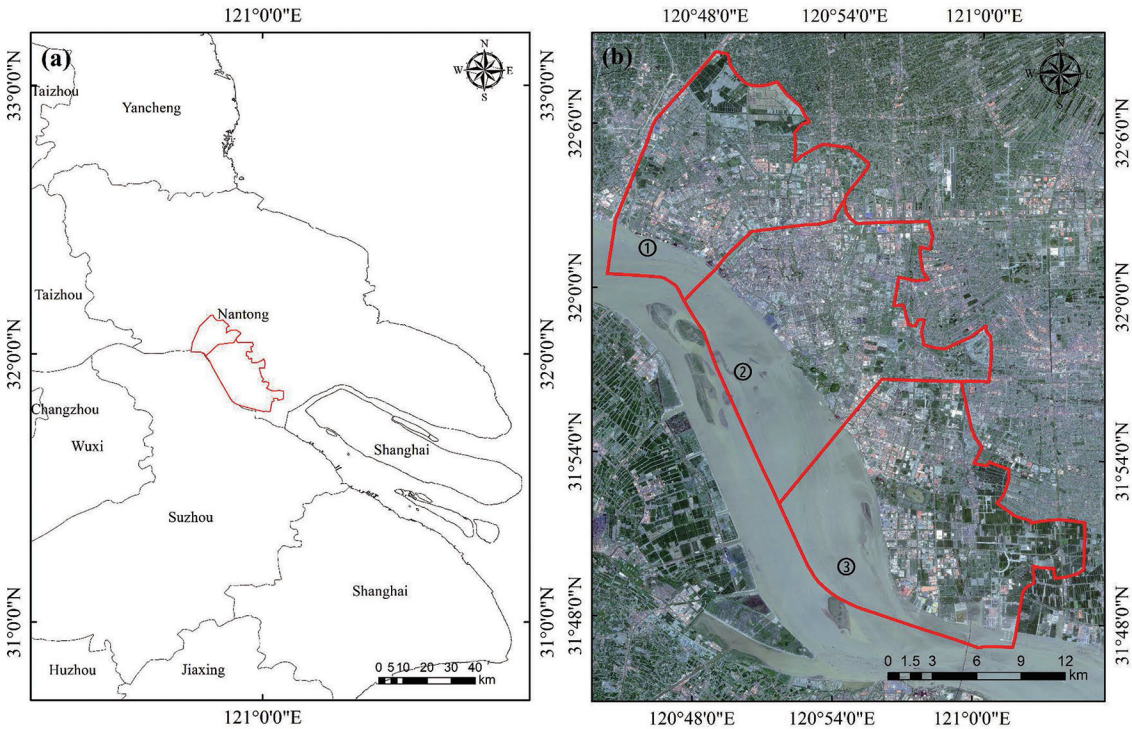

Figure 1. The location of study area and its boundary.

images without clouds under clear sky were obtained from January, April, and August 2016. Preprocessing the images was done through ENVI 5.4, which mainly includes the radiometric calibration of thermal infrared band and the radiometric calibration of multi-spectral data and atmospheric correction. The multispectral data of all the corrected images are converted to the true surface reflectance, and the thermal infrared data is converted to the brightness temperature at the sensor, expressed in degrees Celsius. LST is calculated from the atmospheric corrected *Landsat 8* Thermal Infrared Sensor (Band 10). All equations are derived from the United States Geological Survey. Additional parameters such as atmospheric upward radiance and download radiance are required to calculate the LST. The authors obtained the corresponding parameters on the National Aeronautics and Space Administration (NASA) official website (https://atmcorr.gsfc.nasa.gov) to calculate the radiance of the Blackbody at the same temperature.

$$\mathrm{NDVI} = \frac{\mathrm{NIR} - \mathrm{R}}{\mathrm{NIR} + \mathrm{R}} \tag{1}$$

$$\mathrm{LST} = \frac{K_2}{\ln\left(\frac{K_1}{B(T_s)} + 1\right)} \tag{2}$$

$$B(T_s) = \frac{[L_{\pm} - L_{\uparrow} - \tau(1-\varepsilon) \times L_{\downarrow}]}{\varepsilon\tau} \tag{3}$$

$$L_{\alpha} = \mathrm{gain} \times DN + \mathrm{offset} \tag{4}$$

where K_1 and K_2 are sensor-specific calibration constants, among which Band 10: $K_1 = 774.89$, $K_2 = 1321.08$; Band 11: $K_1 = 480.89$, $K_2 = 1201.14$; $B(T_s)$ is the radiance received by the sensor at a Blackbody with a temperature of T_s; L_{α} is used by the satellite sensor as a radiation calibration coefficient to convert the pixel *DN* value into the received radiance value; $L_{\uparrow}$ and $L_{\downarrow}$ represent the upward and downward radiation parameters of the atmosphere; τ and ε are the atmospheric transmittance and the surface emissivity, respectively; gain and offset are the slopes of the response functions of Bands 10 and 11; *DN* is the original pixel value of the image.

Land Cover Map

To derive the land cover map of the study area, we use the land use survey data in 2016. According to the reference standard "Classification of Land Use Status" GB/T 21010–2017, the authors merge and reclassify the secondary categories using ArcGIS 10.3. Then the 2016 land use type map are divided into six main types, i.e., bare soil, cultivated land, waterbody, woodland, grass, and impervious surface, as shown in Table 1 and Figure 2.

The classification accuracy of land cover is evaluated by randomly selecting sample points on each land cover category and comparing with the corresponding category in the image, using overall accuracy (OA) and Kappa coefficient (Kappa). These indicators are usually used to quantitatively evaluate the accuracy of Land Use/Land Cover classification (Zhang *et al.* 2020). In general, the overall accuracy of land cover classification OA = 78.19% and kappa = 0.71. The main research objective of this article is to explore the impact of ecological benefits between UIS and UGS. In some illustrations, bare soil, water bodies, and cultivated land will be masked without consideration.

Landscape Metrics on Multi-Level Grid

For complex administrative divisions, a uniform rule with a simple expression is beneficial to statistically summarizing the distribution of natural resources. Grids can be used as the carrier, which can express different levels of macro-information related to the spatial location of natural resources and social variables to better reflect their spatial distribution given an appropriately defined grid size. Considering the size of the study area and the rules of grid division, we divided the grid scale in this study according to the 14–17 standard grid division

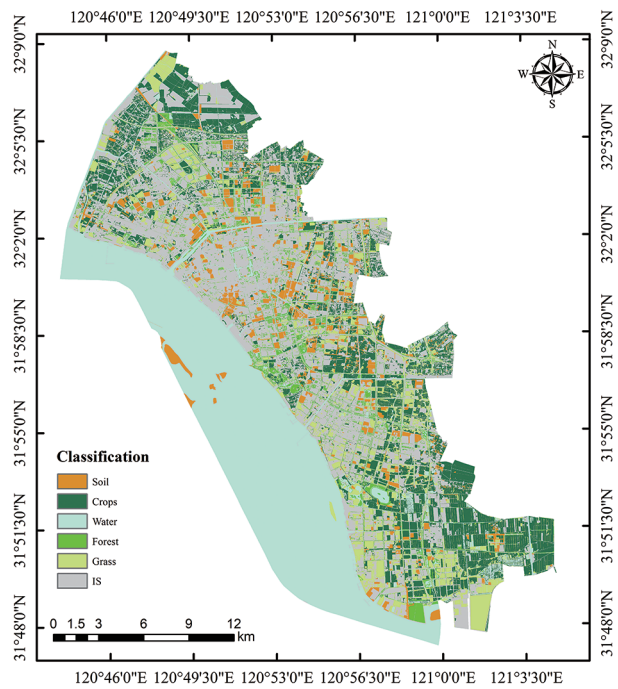

Figure 2. Land use classification in the study area.

Table 1. Land cover categories in the study area.

Category	Description
Soil	Construction site to be built, artificial excavation site, bare ground, etc.
Crops	Growing food, crops, vegetable fields, orchards, paddy fields, etc.
Water	Canals, lakes, reservoirs, ponds, river surface, etc.
Forest	Open forest, dense forest, street trees, other woodlands, etc.
Grass	Lawn, sparse grass, dense grass
Urban Impervious Surface	Built-up areas, residential areas, industrial and commercial areas, squares, roads, railways, other impervious surface, etc.

scale. The authors select four different levels: G1 (grid 1) = 500 m, G2 (grid 2) = 1000 m, G3 (grid 3) = 2000 m, and G4 (grid 4) = 5000 m. Specifically, four sizes of analysis elements are used: (1) 500 m × 500 m, (2) 1000 m × 1000 m, (3) 2000 m × 2000 m, and (4) 5000 m ×5000 m, for each analysis unit (i.e., grid unit), we calculate the average LST as the response variable of the statistical analysis.

To describe the landscape pattern and better explain and understand the landscape function, choosing a suitable landscape index and establishing the relationship between the landscape structure of the object element and the process are essential (Peng *et al.* 2010). The selection of the landscape indices should follow certain rules: (1) as comprehensive as possible to reflect the overall landscape; (2) as less correlation as possible. In this study, following existing studies (Schindler *et al.* 2015; Plexida *et al.* 2014) and considering the situation of the study area, the authors select ten landscape metrics. The authors calculate these landscape metrics at class-level and landscape-level for different grids centered on each site. The calculation for all landscape metrics calculations is performed in Fragstats 4.2 (McGarigal 2015). Table 2 presents the specific characteristics of selected landscape metrics.

Due to the complexity of cities' surface, the distribution of vegetation in cities is usually presented in a disordered manner. We aim to determine the relationship between UIS and UGS types and LST at different grid scales. The temperature response variable of the study area is calculated using the ground temperature value of each grid cell (corresponding to the multi-level grid scales). Subsequent analysis

uses grid cells corresponding to the vegetation and impervious surface categories in the urban land cover. We aim to investigate how the spatial configuration of urban impervious surface and vegetation types at different scales affects urban surface temperature, as assessing this issue is essential to the spatial allocation in urbanization as well as reducing the heat island impact caused by urbanization (Jung *et al.* 2021; Ouyang *et al.* 2020). The research method and process are shown in Figure 3.

Results

Interrelationships Among Multi-Level Grids on Landscape Metrics

In a landscape system, the richer the land use categories, the higher the degree of fragmentation, and the greater the information content of uncertainty, and the higher the calculated Shannon's diversity index (SHDI) value. Table 3 presents average values and standard deviation of the landscape metrics at four different grid scales. The authors observe that SHDI increases along with the increase of the grid scale. At larger grid scales, abundant types of features tend to manifest. In the G1 grid (a very small grid scale), situations might occur when a certain type of ground object occupies a large geographical area, leading to a large CONTAG value (suggesting the existence of dominant types with high connectivity in the landscape). While in the G4 grid, the overall landscape has a higher degree of fragmentation, leading to a small CONTAG value (suggesting the existence of many small patches in the landscape).

A high degree of sprawl indicates that a certain type of superior splicing in the landscape presents considerably high connectivity. On the contrary, a low degree of sprawl suggests a fragmented landscape pattern. Largest patch index (LPI) represents the abundance of dominant species and internal species in the landscape, with a similar changing trend as CONTAG. The authors observe that large-scale

Table 2. Ten selected landscape metrics and their descriptions.

Landscape Metrics	Scale Level	Unit	Description
Patch density (PD)	Class/Landscape	/100ha	$\mathrm{PD} = \frac{n_i}{A}(10{,}000)(100)$
Landscape shape index (LSI)	Class/Landscape	None	$\mathrm{LSI} = \frac{e_i}{\mathrm{mine}_i}$
Percentage of landscape (PLAND)	Class	（0,100]%	$\mathrm{PLAND} = P_i = \frac{\sum_{j=1}^{n} a_{ij}}{A}(100)$
Aggregation index (AI)	Class/Landscape	（0,100]	$\mathrm{AI} = \left[\frac{g_{ik}}{\max \rightarrow g_{ik}}\right](100)$
Edge density (ED)	Class/Landscape	m/ha	$\mathrm{ED} = \frac{\sum_{k=1}^{m} e_{ik}}{A}(10{,}000)$
Shannon's diversity index (SHDI)	Landscape	None	$\mathrm{SHDI} = -\sum_{i=1}^{m}(p_i * \ln p_i)$
CONNECT	Class	%	$\mathrm{CONNECT} = \left[\frac{\sum_{j=k}^{n} c_{ijk}}{\frac{n_i(n_i-1)}{2}}\right](100)$
Area_mean (MN)	Class/Landscape	ha	$\mathrm{Area\_MN} = \frac{\sum_{i=1}^{m}\sum_{j=1}^{n} a_{ij}}{A}$
Largest patch index (LPI)	Class/Landscape	（0,100]%	$\mathrm{LPI} = \frac{\max(a_{ij})}{A}(100)$
CONTAG	Class	（0,100]%	$\mathrm{CONTAG} = \left[1 + \frac{\sum_{i=1}^{m}\sum_{k=1}^{m}\left[(p_i)\left(\frac{g_{ik}}{\sum_{k=1}^{m} g_{ik}}\right)\right]\left[\ln(p_i)\left(\frac{g_{ik}}{\sum_{k=1}^{m} g_{ik}}\right)\right]}{2\ln n_i}\right](100)$

n_i = number of patches in the landscape of patch type (class) I; A = total landscape area (m^2); e_i = total length of edge (or perimeter) of class i in terms of number of cell surfaces; includes all landscape boundary and background edge segments involving class i; mine_i = minimum total length of edge (or perimeter) of class i in terms of number of cell surfaces; P_i = proportion of the landscape occupied by patch type(class) i; a_{ij} = area (m^2) of patch ij; max − g_{ik} = maximum number of like adjacencies (joins) between pixels of patch type (class) i (see below) based on the single-count method; e_{ik} = total length (m) of edge in landscape involving patch type (class) i; c_{ijk} = joining between patch j and k (0 = unjoined, 1 = joined) of the corresponding patch type (i), based on a user specified threshold distance; g_{ik} = number of like adjacencies (joins) between pixels of patch type (class) i based on the single-count method.

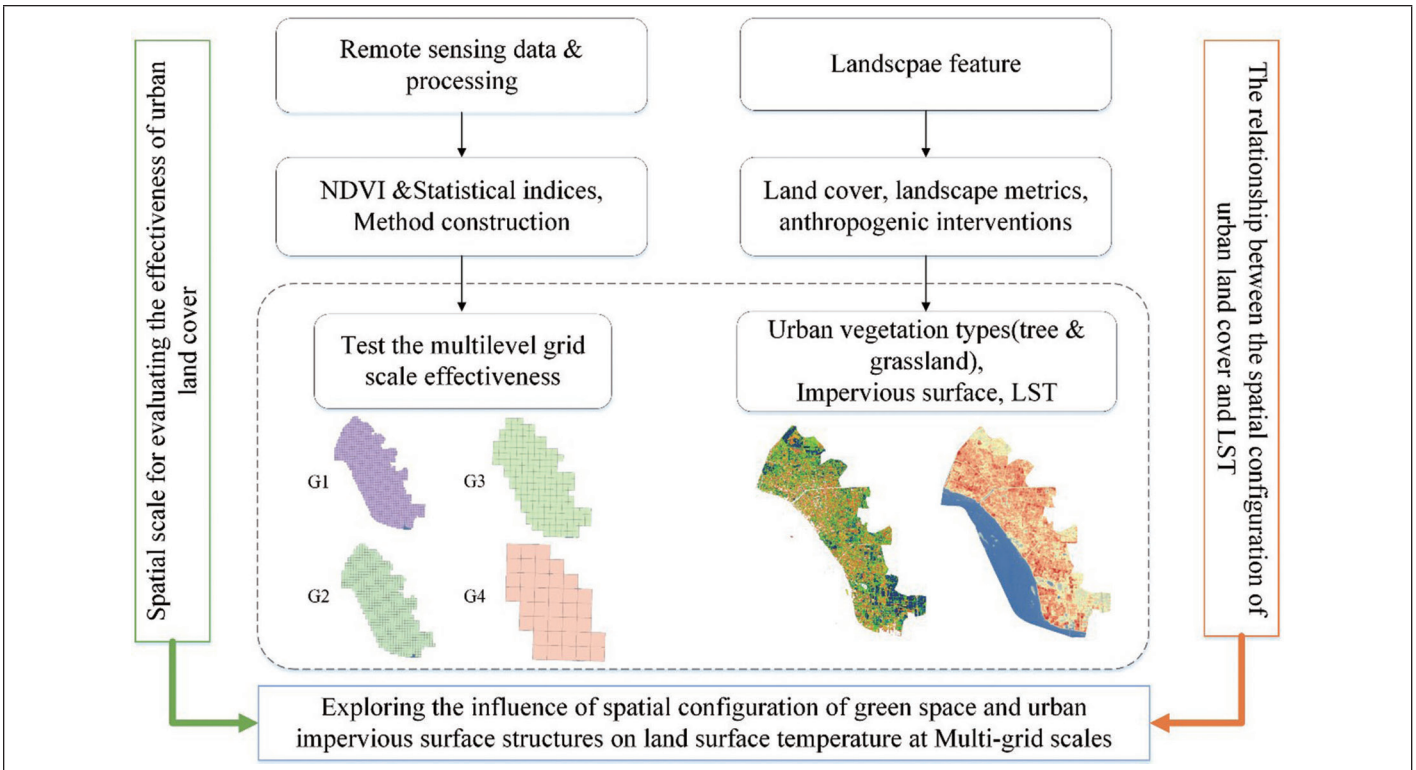

Figure 3. Implementation process and method schematic diagram.

Table 3. Average values and standard deviation of the landscape metrics at four different grid scales.

Metrics	G1	G2	G3	G4
PD	142.65 ± 61.18	114.97 ± 42.07	110.71 ± 22.19	124.46 ± 16.16
AREA_MN	0.90 ± 0.67	1.00 ± 0.40	0.94 ± 0.20	0.82 ± 0.12
LSI	4.53 ± 1.20	7.98 ± 1.67	15.35 ± 2.03	37.56 ± 3.92
PLAND	83.85 ± 4.78	85.04 ± 3.34	85.15 ± 2.03	84.50 ± 1.53
AI	87.13 ± 4.81	86.82 ± 3.38	86.09 ± 2.03	84.90 ± 1.53
ED	282.98 ± 95.67	279.13 ± 66.83	286.96 ± 40.50	305.12 ± 30.34
CONNECT	5.13 ± 4.85	1.79 ± 1.15	0.49 ± 0.14	0.09 ± 0.02
LPI	47.67 ± 19.18	41.17 ± 17.28	34.45 ± 16.67	24.48 ± 10.71
SHDI	1.11 ± 0.28	1.28 ± 0.21	1.42 ± 0.18	1.53 ± 0.11
FRAC_AM	1.16 ± 0.05	1.20 ± 0.04	1.23 ± 0.04	1.25 ± 0.01
CONTAG	50.84 ± 10.85	44.67 ± 13.75	44.74 ± 6.40	40.24 ± 4.19

PD = patch density; AREA_MN = area_mean; LSI = large-scale integration; PLAND = percentage of landscape; AI = aggregation index; ED = edge density; LPI = largest patch index; SHDI = Shannon's diversity index; FRAC_AM =Fractal dimension index_Area-weighted Mean.

integration (LSI) presents an increasing pattern when the grid scale increases. When the shape of the landscape becomes more irregular and the length of the inner edge of the landscape of the corresponding patch type increases, the growth of LSI occurs, as a large-scale network in the grid contains more abundant feature types. The authors also observe that aggregation index (AI) and CONNECT changed in a similar manner across the four grid scales.

The scale effect is an important issue in landscape research, although the concept of scale may differ in various studies. In order to quantify the impact of scale on the landscape pattern index, the authors use a multi-scale grid by dividing the area according to different grid schemes. To estimate the most suitable size of subareas in the landscape, five random grids in each landscape were created. The authors selected five subset grids (Figure 4.random grid) of multi-scale sizes (5 km, 2 km, 1 km, 0.5 km) and calculated landscape indicators. We further plot four metrics, i.e., percentage of landscape (PLAND), patch density (PD), AI, and LPI against the size of the sample area to determine the average area over which most curves are asymptotic (Figure 4). The authors observe that values of almost all indicators level between 2 km and 1 km.

As most of the index values are stable at the size of 1 km, it is selected as the appropriate size for each subregion. The stability level is preferred because the ability to compare different locations is affected by the way data is collected and reported. With the increase of spatial scale, the filtering effect unavoidably makes small patches merge, leading to decreased number of patches and increased average patch size in the landscape.

Analysis of Landscape Indicators in Function Zone

For each level of grid, three levels of landscape indicators were introduced. In the subsequent index selection, we conducted further screening and regional evaluation according to the correlation of each

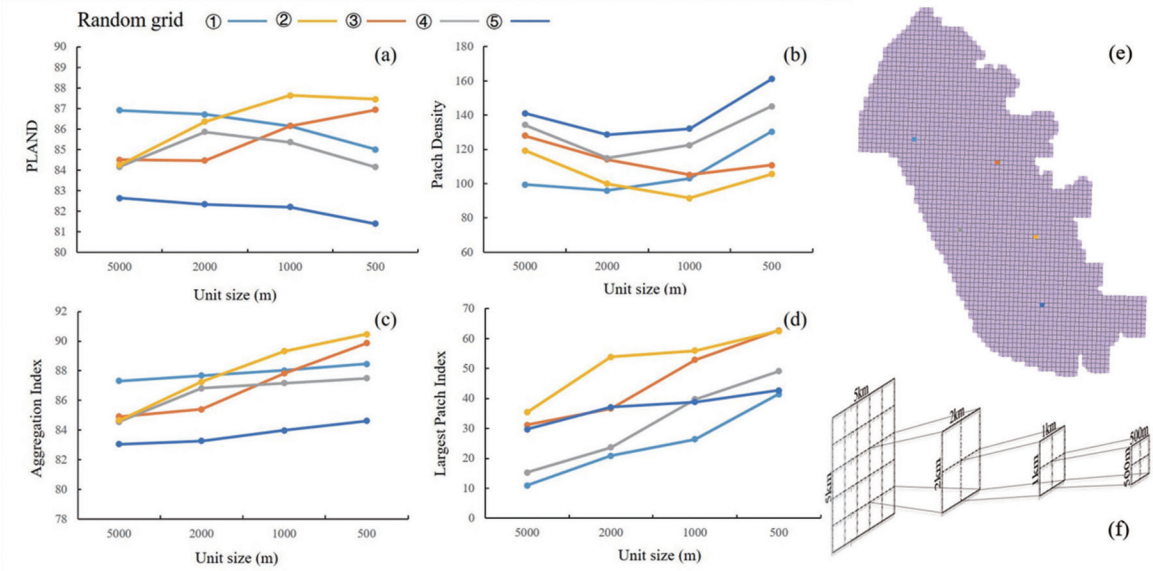

Figure 4. Parameter comparison at different grid scales.

Table 4. Landscape-level indices in different districts of the study area.

District	PLAND(%)			SHDI	Area_MN	ED	LSI	CONNECT	AI
	IS	Forest + Grass + Crops	Forest + Grass						
Study_area	30.54	32.73	15.43	1.57	1.33	205.6	125.03	0.005	78.24
Chongchuan	34.28	17.36	11.42	1.42	1.67	168.7	55.99	0.025	78.01
Gangzha	39.58	37.58	15.25	1.55	1.07	256	80.41	0.015	77.54
Kaifaqu	22.79	39.80	18.21	1.57	1.38	197.8	80.46	85.44	80.55

PLAND = percentage of landscape; IS = impervious surface; SHDI = Shannon's diversity index; AREA_MN = area_mean; ED = edge density; LSI = large-scale integration; AI = aggregation index.

landscape index. According to the administrative divisions included in the study area, landscape-level indices in each administrative area are shown in Table 4. The overall vegetation ratio in the study area is 15.43%, with Chongchuan District of 11.42%, Gangzha District of 15.25%, and Kaifaqu District of 18.21%. SHDI is an index unique to the landscape level, reflecting the complexity of the landscape. The larger the SHDI value, the more diverse the components in the landscape. We notice that the diversity reflected from SHDI in these three districts is ranked as: Kaifaqu District > Gangzha District > Chongchuan District.

The Kaifaqu District is a district that experienced and is still experiencing intensive urban development. Its landscape proportion is the highest with low patch density, suggesting the lowest fragmentation degree of its green space. The diversity and aggregation degree are the highest in the Kaifaqu District, indicating that the vegetation types are rich and concentrated with intact green landscape features. Chongchuan District and Gangzha District, with a high percentage of impervious surface, are the administrative regions that have been developed in earlier years. Their vegetation distribution is largely restricted by existing land use. As a result, the patches of vegetation are fragmented, evidenced by the low proportion of green landscape and low edge density. Its diversity and degree of aggregation are also lower than the overall level of the entire study area.

Further, we use the 1 km grid (the optimal grid size) for functional area division analysis. We refer the classification standard of functional areas to the classification standard of Local Climate Zones (LCZ) (Stewart and Oke 2012). A total of five areas are selected for analysis: urban green spaces, residential areas, agricultural land, industrial areas, and commercial office areas (Figure 5).

The landscape indices are further calculated for the study area and each functional zone (Figure 6). We notice that there exist dominant land-use types in each functional zone. The proportion of the urban green landscape is higher than that of other functional zones that include residential areas, office areas, and commercial areas (Figure 6a). In general, the vegetation landscape of these districts is considerably lower than other landscapes, and the industrial area is found to lack vegetation landscape the most. PD, average patch size, and ED can inform the degree of landscape fragmentation (Ren *et al.* 2013). From Figure 6b–d, the average patch area and AI of the grass are generally larger in the commercial office area. The industrial zone has a small average patch area and a high edge density of the forest, indicating that the open land in industrial areas is mostly used for construction. In residential and industrial areas, impervious surfaces form the dominant land use category on this grid scale.

Spatial Effects of Urban Impervious Surface and Vegetation Types on Land Surface Temperature

In this section, we analyze the spatial effects of the urban impervious surface and vegetation types and their distribution on LST. The LST was derived from *Landsat 8* in January (ranging from –6.40 to 22.14°C), April (ranging from 11.67 to 51.33°C), and August (ranging from 10.57 to 46.73°C) 2016. As shown in Table 5, in winter, spring, and summer, the urban impervious surface is primarily positively correlated with LST at three different grid scales (G1, G2, G3). Forest and grass at three different grid scales (G1, G2, G3) are negatively correlated with LST. Among them, the correlation between forest and grass and LST fluctuates with different seasons and spatial scales. Still, the correlation between grass and LST is more than that of forest in general.

The strength of correlation between LST and UIS increases as the grid-scale increases and the seasons change from January to August. The correlation between forest and LST is more notable at the small grid-scale. In comparison, the correlation between grassland and LST was different in season and not significant in small grid scale.

Figure 5. Schematic diagram of urban functional zoning.

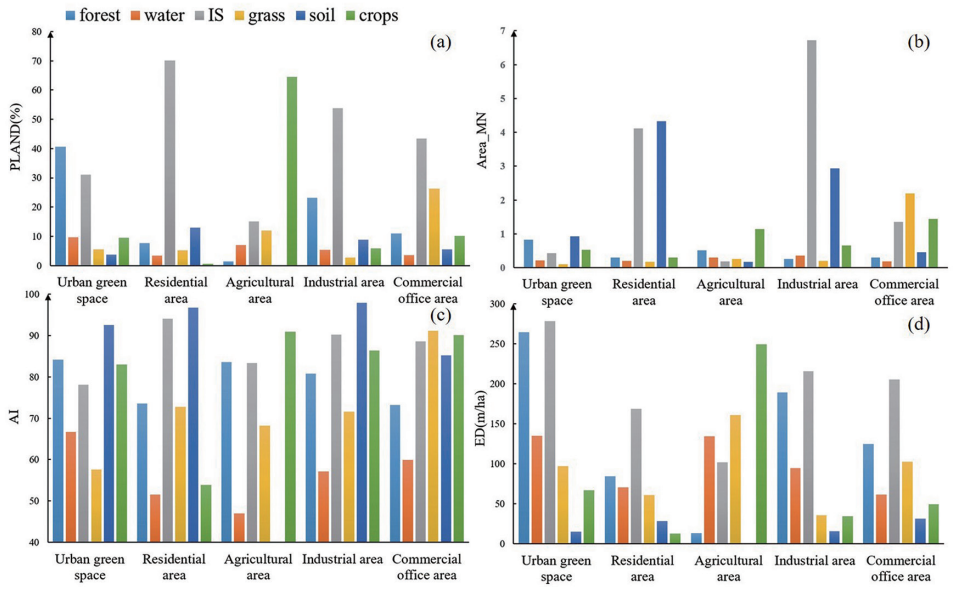

Figure 6. Landscape indicators of different land use categories in different functional zones. IS = impervious surface; PLAND = percentage of landscape; Area_MN = area_mean; AI = aggregation index; ED = edge density.

Table 5. Correlation between Land Surface Temperature (LST) and landscape metrics.

Date	Grid–Level	UIS			Forest			Grass		
		PD	LPI	AI	PD	LPI	AI	PD	LPI	AI
LST–Jan	G1	–0.05	0.216	0.065	0.015	–0.202	–0.363	–0.064	–0.131	–0.145
	G2	–0.315	0.077	0.105	–0.072	0.108	0.096	–0.012	0.152	0.339
	G3	–0.225	–0.161	–0.317	–0.066	0.209	–0.025	0.166	0.275	0.069
LST–Apr	G1	–0.098	0.152	0.000	0.025	–0.194	–0.334	0.164	0.208	–0.008
	G2	–0.433*	0.482*	0.458*	0.068	0.187	–0.102	–0.346	0.205	0.421*
	G3	–0.152	–0.234	–0.295	–0.178	–0.016	0.066	–0.082	0.473*	0.648**
LST–Aug	G1	–0.015	0.268	0.052	–0.050	–0.384	–0.326	0.096	–0.211	–0.320
	G2	–0.568**	0.585**	0.670**	0.092	–0.025	–0.255	–0.503*	–0.188	0.442*
	G3	–0.357	0.187	0.165	–0.073	–0.029	0.131	–0.306	0.225	0.678**

**Significantly correlated at the 0.01 level; *significantly correlated at the 0.05 level. UIS = urban impervious surface; PD = patch density; largest patch index (LPI); AI = aggregation index.

Grass and LST present a weak correlation in winter and spring, with a strengthened correlation presented at larger grid scales. In April and August, the LPI and AI of grassland at the large scale (G3) showed a strong correlation, mainly because grassland can reach the maximum growth and aggregation state in summer, and because the aggregation effect is strong, and the cooling effect on LST will exceed that of trees. The results of previous studies have shown that grass is not as effective as tree canopy in LST cooling (Myint *et al.* 2015), and its cooling effect may be more affected by different management methods such as irrigation. Trees mainly lower the temperature by evapotranspiration and providing shade.

Discussion

Impact of Scale on Urban Landscape Pattern

The intensified urbanization process has complicated various urban infrastructures such as buildings and road networks (Wei and Ye 2014). Due to the requirements of climate and landscape planning, the composition of tree communities in cities is usually dominated by only a few species. Meanwhile, the proportion of urban green space is likely to be reduced given the urban expansion. Small and isolated patches of vegetation tend to replace the previous large, continuous patches. Such a decrease in diversity usually implies an increase in the coverage of dominant types and a decrease in nondominant types. When the number of landscape categories remains unchanged, diversity from the inter-changes of landscape categories becomes notable. As the monitoring scales increase, a decrease in diversity implies that the dominance from the dominant type becomes more prominent, while the nondominant type tends to disappear. At the land use and land cover level, different types of coverage have different degrees of impact, largely depending on the monitoring scales.

Our results of landscape pattern show that scale diversity is directly reflected in the characteristics and relationships of various variables, indicating that scale selection is necessary in landscape pattern research. For ecological problems, translation must be pushed across the scales, as small-scale polymerization explores the laws of information, and data information transfer between the various scales must be studied (Wu 2004; Zhao *et al.* 2019). Therefore, studies on the scale effect have essential practical significance. Besides, a better understanding of scale effect on landscape characteristics is also beneficial to arriving at a better selection of strong representations of landscape indices.

Scale Affects Relationship Between LST and Spatial Pattern of Urban Cover

This study investigated the impact of landscape patterns and the spatial configuration of vegetation patches on the surface temperature in Nantong. Our results show that the impact of different types of vegetation and impervious surface space configuration on LST varies with the different landscape indicators. The correlation coefficient between LST and landscape metrics is highly linked to irregularly shaped vegetation patterns, patch size, and green margins. The vegetation landscape scale is significantly correlated with LST. Different landscape patterns and configurations (such as size, connectivity, and edge density) affect the heat exchange between vegetation and its surrounding environment, leading to the changing dynamics of warming and cooling effects (Aram *et al.* 2019).

In a fixed relative number of land cover elements, the surface temperature can be significantly increased or decreased through different spatial arrangements of the elements. This is because the spatial scale affects the energy flow or energy exchange between land cover elements (Tan *et al.* 2020). Compared with previous studies, this study analyzes the landscape pattern index at different scales. In general, the correlation between surface temperature and land cover variables can be found on a coarser scale, which may indicate that the correlation between surface temperature and land cover layout is different. At a smaller scale, there are fewer factors to consider. Increasing coverage types need to consider more factors to better predict LST. Our results also reveal that grass can play a role at appropriate planning scales in reducing urban heat island problem, which is consistent with the studies by Zhou *et al.* (2011) and by Yao *et al.* (2020) who indicate that dominated greenspace offers the greatest heat stress relief.

Limitations and Recommendations for Future Studies

Our study shows that the types and degrees of landscape fragmentation in cities lead to different scale and regional characteristics that might give rise to different ecological effects. In regional planning and management, a strict boundary definition of urban growth can effectively mitigate uncontrolled city growth and thus slow down the loss of woodland. On the other hand, when carrying out regional habitat restoration and functional enhancement, it is necessary to consider landscape characteristics of different regions, such as the role played by the spatial structure of woodland and construction land. As the development level of different cities is not consistent, the influence of the layout of internal ground objects in different cities also needs to be considered, that is, the comparative study between multiple cities.

In this study, we used data that covers one year for analysis. Thus, we encourage a comparative analysis of the time series when data that cover longer temporal periods are involved. In addition, urban monitoring data with higher resolution (e.g., worldview series) can be considered. Lidar point clouds can also be used to characterize the vertical dimension of vegetation. Due to the continuous acceleration of urbanization around the world, the fragmentation problem in the urban ecosystem is expected to be aggravated, leading to challenges for traditional methods in ecological diversity monitoring. In the process of urban construction, special attention should be paid to the construction of green corridors and designing multi-functional greenways, aiming to make cities eco-friendly.

Conclusion

As urban green space becomes limited given rapid urban development, understanding the relationship between land surface temperature and urban green space as well as urban impervious surfaces is critical. To better understand the impact of different configurations on the urban heat island effect at different scales, this study distinguishes the effects of UIS and UGS in urban areas at multi-grid scales and explores their relationship with land surface temperature. Our results indicate that: (1) different indicators present significant characteristic disparity under the four grid scales; compared with other scales, indicators have the relatively stability correlation at 1 km; (2) different urban green spaces have notable negative effects on surface temperature. At G3 scale, grassland had a strong correlation with LST in AI and LPI, which were 0.473 and 0.648, and the role of grass is more prominent during the growing season. It suggested that fine-scale planning is of great significance to alleviating the urban heat island effect. However, this study has limitations and room for improvement. For example, in light of the size of the study area, we select four scales for the grid setting. Future studies can consider more grid settings and involve more indicators.

Acknowledgments

This research is supported by the National Key Research and Development Program of China with grant number 2018YFB2100501, the National Natural Science Foundation of China with grant numbers 41890820, 42090012, 41771452 and 41771454, and the Key Research and Development Program of Yunnan province in China with grant number 2018IB023. No potential conflict of interest was reported by the authors.

References

Aram, F., E. H. García, E. Solgi and S. Mansournia. 2019. Urban green space cooling effect in cities. *Heliyon* 5(4):e01339. https://doi.org/10.1016/j.heliyon.2019.e01339.

Bowler, D. E., L. Buyung-Ali, T. M. Knight and A. S. Pullin. 2010. Urban greening to cool towns and cities: A systematic review of the empirical evidence. *Landscape and Urban Planning* 97(3):147–155. https://doi.org/10.1016/j.landurbplan.2010.05.006.

Chen, J., S. Jin and P. Du. 2020. Roles of horizontal and vertical tree canopy structure in mitigating daytime and nighttime urban heat island effects. *International Journal of Applied Earth Observation and Geoinformation* 89, 102060.

https://doi.org/10.1016/j.jag.2020.102060.

Godwin, C., G. Chen and K. K. Singh. 2015. The impact of urban residential development patterns on forest carbon density: An integration of lidar, aerial photography and field mensuration. *Landscape and Urban Planning* 136, 97–109.

https://doi.org/10.1016/j.landurbplan.2014.12.007.

Hu, Y., Z. Dai and J. M. Guldmann. 2021. Greenspace configuration impact on the urban heat island in the Olympic Area of Beijing. *Environmental Science and Pollution Research* 1–12. https://doi.org/10.1007/s11356-020-12086-z.

Jung, M. C., K. Dyson and M. Alberti. 2021. Urban landscape heterogeneity influences the relationship between tree canopy and land surface temperature. *Urban Forestry & Urban Greening* 57:126930. https://doi.org/10.1016/j.ufug.2020.126930.

Kabisch, N. and D. Haase. 2013. Green spaces of European cities revisited for 1990–2006. *Landscape and Urban Planning* 110:113–122. https://doi.org/10.1016/j.landurbplan.2012.10.017.

Liu, Y., X. Huang, Q. Yang and Y. Cao. 2021. The turning point between urban vegetation and artificial surfaces for their competitive effect on land surface temperature. *Journal of Cleaner Production* 292:126034. https://doi.org/10.1016/j.jclepro.2021.126034.

Masoudi, M., P. Y. Tan and M. Fadaei. 2021. The effects of land use on spatial pattern of urban green spaces and their cooling ability. *Urban Climate* 35: 100743. https://doi.org/10.1016/j.uclim.2020.100743.

Myint, S. W., B. Zheng, E. Talen, C. Fan, S. Kaplan, A. Middel and A. Brazel. 2015. Does the spatial arrangement of urban landscape matter? Examples of urban warming and cooling in Phoenix and Las Vegas. *Ecosystem Health and Sustainability* 1(4):1–15. https://doi.org/10.1890/EHS14-0028.1.

McGarigal, K. 2015. *FRAGSTATS Help*. Amherst, Mass.: University of Massachusetts.

Nowak, D. J. and E. J. Greenfield. 2012. Tree and impervious cover change in U.S. cities. *Urban Forestry & Urban Greening* 11(1):21–30. https://doi.org/10.1016/j.ufug.2011.11.005.

Ouyang, W., T. E. Morakinyo, C. Ren and E. Ng. 2020. The cooling efficiency of variable greenery coverage ratios in different urban densities: A study in a subtropical climate. *Building and Environment* 174:106772. https://doi.org/10.1016/j.buildenv.2020.106772.

Peng, J., Y. Wang, Y. Zhang, J. Wu, W. Li and Y. Li. 2010. Evaluating the effectiveness of landscape metrics in quantifying spatial patterns. *Ecological Indicators* 10(2):217–223. https://doi.org/10.1016/j.ecolind.2009.04.017.

Plexida, S. G., A. I. Sfougaris, I. P. Ispikoudis and V. P. Papanastasis. 2014. Selecting landscape metrics as indicators of spatial heterogeneity—A comparison among Greek landscapes. *International Journal of Applied Earth Observation and Geoinformation* 26:26–35. https://doi.org/10.1016/j.jag.2013.05.001.

Plowright, A. A., N. C. Coops, C. M. Chance, S. R. Sheppard and N. W. Aven. 2017. Multi-scale analysis of relationship between imperviousness and urban tree height using airborne remote sensing. *Remote Sensing of Environment* 194:391–400. https://doi.org/10.1016/j.rse.2017.03.045.

Qian, Y., Z. Li, W. Zhou and Y. Chen. 2019. Quantifying spatial pattern of urban greenspace from a gradient perspective of built-up age. *Physics and Chemistry of the Earth, Parts A/B/C* 111:78–85. https://doi.org/10.1016/j.pce.2019.05.001.

Ren, Y., X. Wei, D. Wang, Y. Luo, X. Song, Y. Wang, Y. Yang and L. Hua. 2013. Linking landscape patterns with ecological functions: A case study examining the interaction between landscape heterogeneity and carbon stock of urban forests in Xiamen, China. *Forest Ecology and Management* 293:122–131. https://doi.org/10.1016/j.foreco.2012.12.043.

Stewart, I. D. and T. R. Oke. 2012. Local climate zones for urban temperature studies. *Bulletin of the American Meteorological Society* 93(12):1879–1900. https://doi.org/10.1175/BAMS-D-11-00019.1.

Schindler, S., H. von Wehrden, K. Poirazidis, W. M. Hochachka, T. Wrbka and V. Kati. 2015. Performance of methods to select landscape metrics for modelling species richness. *Ecological Modelling* 295:107–112. https://doi.org/10.1016/j.ecolmodel.2014.05.012.

Shao, Z., L. Ding, D. Li, O. Altan, M. Huq and C. Li. 2020. Exploring the relationship between urbanization and ecological environment using remote sensing images and statistical data: A case study in the Yangtze River Delta, China. *Sustainability* 12(14):5620. https://doi.org/10.3390/su12145620.

Shao, Z., H. Fu, D. Li, O. Altan and T. Cheng. 2019. Remote sensing monitoring of multi-scale watersheds impermeability for urban hydrological evaluation. *Remote Sensing of Environment* 232:111338. https://doi.org/10.1016/j.rse.2019.111338.

Song, D. X., C. Huang, T. He, J. O. Sexton, A. Li, S. Li and J. R. Townshend. 2021. Improved modeling and analysis of the patch size–frequency distribution of forest disturbances in China based on a Landsat forest cover change product. *International Journal of Digital Earth* 14(2):181–201. https://doi.org/10.1080/17538947.2020.1810337.

Tan, J., D. Yu, Q. Li, X. Tan and W. Zhou. 2020. Spatial relationship between land-use/land-cover change and land surface temperature in the Dongting Lake area, China. *Scientific Reports* 10(1):1–9. https://doi.org/10.1038/s41598-020-66168-6.

Trlica, A., L. R. Hutyra, L. L. Morreale, I. A. Smith and A. B. Reinmann. 2020. Current and future biomass carbon uptake in Boston's urban forest. *Science of the Total Environment* 709:136196. https://doi.org/10.1016/j.scitotenv.2019.136196.

Wei, Y. D. and X. Ye. 2014. Urbanization, urban land expansion and environmental change in China. *Stochastic Environmental Research and Risk Assessment* 28(4):757–765.

https://doi.org/10.1007/s00477-013-0840-9.

Wu, J. 2004. Effects of changing scale on landscape pattern analysis: scaling relations. *Landscape Ecology* 19(2):125–138. https://doi.org/10.1023/B:LAND.0000021711.40074.ae.

Xing, H. and Y. Meng. 2020. Measuring urban landscapes for urban function classification using spatial metrics. *Ecological Indicators* 108:105722. https://doi.org/10.1016/j.ecolind.2019.105722.

Xu, C., S. Zhao and S. Liu. 2020. Spatial scaling of multiple landscape features in the conterminous United States. *Landscape Ecology* 35(1):223–247. https://doi.org/10.1007/s10980-019-00937-1.

Xu, X., T. Tong, W. Zhang and L. Meng. 2020. Fine-grained prediction of PM2. 5 concentration based on multisource data and deep learning. *Atmospheric Pollution Research* 11(10):1728–1737. https://doi.org/10.1016/j.apr.2020.06.032.

Yang, J., S. Li, J. Xu, X. Wang and X. Zhang. 2020. Effects of changing scales on landscape patterns and spatial modeling under urbanization. *Journal of Environmental Engineering and Landscape Management* 28(2):62–73. https://doi.org/10.3846/jeelm.2020.12081.

Yao, L., T. Li, M. Xu and Y. Xu. 2020. How the landscape features of urban green space impact seasonal land surface temperatures at a city-block-scale: An urban heat island study in Beijing, China. *Urban Forestry & Urban Greening* 52:126704. https://doi.org/10.1016/j.ufug.2020.126704.

Yin, C. L., F. Meng and Q. R. Yu. 2020. Calculation of land surface emissivity and retrieval of land surface temperature based on a spectral mixing model. *Infrared Physics & Technology* 108:103333. https://doi.org/10.1016/j.infrared.2020.103333.

Zhang, D., H. Wang, X. Wang and Z. Lü. 2020. Accuracy assessment of the global forest watch tree cover 2000 in China. *International Journal of Applied Earth Observation and Geoinformation* 87:102033. https://doi.org/10.1016/j.jag.2019.102033.

Zhang, Y., K. Qin, Q. Bi, W. Cui and G. Li. 2020. Landscape patterns and building functions for urban land-use classification from remote sensing images at the block level: A case study of Wuchang District, Wuhan, China. *Remote Sensing* 12(11):1831. https://doi.org/10.3390/rs12111831.

Zhang, Y. and Z. Shao. 2021. Assessing of urban vegetation biomass in combination with LiDAR and high-resolution remote sensing images. *International Journal of Remote Sensing* 42(3): 964–985. https://doi.org/10.1080/01431161.2020.1820618.

Zhao, S. M., Y. F. Ma, J. L. Wang and X. Y. You. 2019. Landscape pattern analysis and ecological network planning of Tianjin City. *Urban Forestry & Urban Greening* 46:126479. https://doi.org/10.1016/j.ufug.2019.126479.

Zheng, B., S. W. Myint and C. Fan. 2014. Spatial configuration of anthropogenic land cover impacts on urban warming. *Landscape and Urban Planning* 130:104–111. https://doi.org/10.1016/j.landurbplan.2014.07.001.

Zhengming, W. and J. Dozier. 1989. Land-surface temperature measurement from space: Physical principles and inverse modeling. *IEEE Transactions on Geoscience and Remote Sensing* 27(3):268–278. https://doi.org/10.1109/36.17668.

Zhou, W. and F. Cao. 2020. Effects of changing spatial extent on the relationship between urban forest patterns and land surface temperature. *Ecological Indicators* 109:105778. https://doi.org/10.1016/j.ecolind.2019.105778.

Zhou, W., G. Huang and M. L. Cadenasso. 2011. Does spatial configuration matter? Understanding the effects of land cover pattern on land surface temperature in urban landscapes. *Landscape and Urban Planning* 102(1):54–63. https://doi.org/10.1016/j.landurbplan.2011.03.009.

Zhou, W., J. Wang and M. L. Cadenasso. 2017. Effects of the spatial configuration of trees on urban heat mitigation: A comparative study. *Remote Sensing of Environment* 195:1–12. https://doi.org/10.1016/j.rse.2017.03.043.

Zhuang, Q., Z. Shao, D. Li, X. Huang, B. Cai, O. Altan and S. Wu. 2022. Unequal weakening of urbanization and soil salinization on vegetation production capacity. *Geoderma* 411:115712. https://doi.org/10.1016/j.geoderma.2022.115712.

Zhuang, Q., Z. Shao, X. Huang, Y. Zhang, W. Wu, X. Feng and O. Altan. 2021. Evolution of soil salinization under the background of landscape patterns in the irrigated northern slopes of Tianshan Mountains, Xinjiang, China. *Catena* 206:105561. https://doi.org/10.1016/j.catena.2021.105561.

Long-Term Changes of Land Use and Land Cover in the Yangtze River Basin from 1990–2020 Landsat Data

Junyuan Yao and Shuanggen Jin

Abstract

Economic development and climate change drive the land use and land cover (LULC) change globally. Annual robust maps of LULC are critical for studying climate change and land–climate interaction. However, the current existing methods for optimizing and expanding the publicly available China land cover data set (CLCD) are limited. In this article, 30-m annual LULC changes are obtained from 1990 to 2020 in the Yangtze River basin (YRB). The results show an overall accuracy rate of 82.66% and better performances on Geo-Wiki test samples when compared to similar products. Based on our 30-m annual LULC data set, the drastic LULC changes are found in YRB over a 30-year period, where impervious surface area more than tripled, cropland area decreased by 6.12%, and water area decreased by 6.09%. In addition, through the geographically and temporally weighted regression method, a fitting model with a goodness of fit of 0.91 well reveals that human activity plays a driving role in the LULC change of YRB.

Introduction

Land use and land cover (LULC) change has a close relationship with social and economic development, ecosystem carrying capacity, surface energy balance, and material circulation (Foley *et al.* 2005; Gibbard *et al.* 2005; Vorosmarty *et al.* 2010; Houghton *et al.* 2012; Haddeland *et al.* 2014; Findell *et al.* 2017). The Yangtze River basin (YRB) covers several major cities and nature reserves in China, which is of great importance in economic development and ecological conservation. Recently, there have been serious problems in YRB in terms of water environment pollution and ecological damage due to excessive reclamation and economic development (Yang *et al.* 2021a). Therefore, it is essential to map the LULC change in YRB to explore the processes and drivers within the basin over the past 30 years. Effective environmental governance and development planning depends heavily on accurate LULC products and effective quantitative analysis of LULC changes.

Remote sensing is the most efficient way to monitor large-scale LULC change. In recent years, the free access to a huge volume of remote sensing satellite data (e.g., AVHRR, MODIS, Landsat, and Sentinel-2) and high-performance cloud computing platforms such as Google Earth Engine (GEE) have greatly promoted large-scale and long-term remote sensing studies on LULC (Gorelick *et al.* 2017; Zhu *et al.* 2019). With the GEE platform, Qu *et al.* (2021) used the k-means method to optimize the sample quality and generated LULC products from 1992 to 2015 for three provinces in the Yangtze River delta region using the random forest (RF) classification method. Liu *et al.* (2020a) built a training sample based on OpenStreetMap data and used classifiers of RF and the classification and regression tree (CART) for LULC mapping in the middle YRB from 1987 to 2017. However, these works have built completely new training sample sets to train the classifiers, which was certainly a huge amount of work (Jin and Zhang 2016). In addition, these results are difficult to apply directly in our region due to uncertain stability.

In addition, a number of open-access LULC data sets were used in YRB LULC change. Chen *et al.* (2020) used the LULC map data from the Resource and Environment Data Cloud Platform of the Chinese Academy of Sciences and reclassified it for the same 20 LULC categories as IGBP-MODIS to examine the influence of land urbanization on meteorology and air quality in the Yangtze River delta. Yang *et al.* (2021b) selected the MOD12Q1 data product from 2001 to 2018 with a spatial resolution of 500 m and reclassified the LULC maps into eight dominant categories to analyze the influence of LUCC on net primary production in YRB and its causes. However, the spatial resolution of 1000 or 500 m is relatively coarse, which is not sufficient for fine-scale LULC monitoring due to the uncertainty inherent of coarse-resolution data (Sulla-Menashe *et al.* 2019). Recently, Landsat data, with their high resolution and long history, have been widely used in large-scale LULC mapping (Liu *et al.* 2020b). Leveraging the data and computing power of the GEE platform, many global land cover products have been released, such as FROM_GLC30 (finer-resolution observation and monitoring of global land cover) (Gong *et al.* 2013), GlobeLand30 (global land cover mapping) (Chen *et al.* 2015), and GLC_FCS30 (global land cover product with fine classification system) (Zhang *et al.* 2021). Compared to these global LULC products, the China Land Cover Dataset (CLCD) (Yang and Huang 2021) provided longer-time-series and higher-precision-validated LULC in the China's region for each year. Since its training samples are sufficient and reliable by combining stable samples extracted from China's land use/cover data sets (Liu *et al.* 2014), the accuracy of CLCD reaches a high level by both visual interpretation sample and third-party sample accuracy tests.

Despite the high-accuracy performance of CLCD, there are still several problems when applying it to the YRB. Considerable siltation occurs in the middle YRB and results in riverbed uplift and mudflats in many places that are more pronounced after the numerous construction of dams and water diversion for agriculture in the upper YRB (Chen *et al.* 2001; Yang *et al.* 2015). Unfortunately, the LULC in these areas is mostly misclassified as impervious surfaces in the CLCD. Further, Dongting Lake, Poyang Lake, and Middle River Bay are important wetland distribution areas in YRB formed by sediment accumulation due to the action of water flow and indirect coverage by water in different hydrological periods (Yang *et al.* 2005; Yang *et al.* 2018). These were also not represented well in the CLCD, in large part because it used the 50th-percentile value of each spectral band as the basic data

Junyuan Yao is with the School of Communication and Information Engineering, Shanghai University, Shanghai 200444, People's Republic of China; and Shanghai Astronomical Observatory, Chinese Academy of Sciences, Shanghai 200030, People's Republic of China.

Shuanggen Jin is with Shanghai Astronomical Observatory, Chinese Academy of Sciences, Shanghai 200030, People's Republic of China; and the School of Surveying and Land Information Engineering, Henan Polytechnic University, Jiaozuo 454000, People's Republic of China (sg.jin@yahoo.com)..

Contributed by Prasad S. Thenkabail, February 14, 2022 (sent for review April 13, 2022; reviewed by Nagesh Kumar D., Prasad S. Thenkabail).

Photogrammetric Engineering & Remote Sensing
Vol. 88, No. 9, September 2022, pp. 573–581.
0099-1112/22/573–581

doi: 10.14358/PERS.22-00050R2

for training and classification, which made the classification results based on combinations of image elements at different times throughout the year. This approach undermined the recognition of land types like wetlands with varying within 1 year. In addition, there was also some misclassification in the mountain shadows of western Sichuan and northern Chongqing. Although the CLCD work flow can improve the overall classification accuracy, there are still some challenges for high-precision mapping of LULC in YRB. Therefore, it is necessary to correct the CLCD and obtain the high-accuracy LULC maps for large-scale YRB. This reclassification process should be an effective, efficient, economic, and operational approach.

In this article, 30-m annual LULC changes are obtained and analyzed in YRB, including (1) obtaining the 30-m annual LULC mapping of YRB from 1990 to 2020 by intercomparing the CLCD with thematic-class products (GFC global forest change, GSW global surface water, and GISA global impervious surface area) (Hansen *et al.* 2013; Pekel *et al.* 2016; Huang *et al.* 2021) and detecting and reclassifying the disputed areas of the CLCD in YRB by using the RF classifier with a smaller number of visually interpreted samples on GEE, (2) analyzing the process and trend of LULC change in YRB over 30 years with explaining the causes of change, and (3) proposing a time-series model of land use degree and exploring the drivers of the LULC change in YRB by using the geographically and temporally weighted regression (GTWR) model (Huang *et al.* 2010). The changes and drivers of the LULC in YRB can provide valuable information for local decision makers and stakeholders.

Data and Methods

Study Area

The Yangtze River Basin (about 1.8 million km2) is located between 90°33′ and 122°19′ E and 24°27′ and 35°54′ N in China, starting from the Qinghai-Tibet Plateau and going eastward into the East China Sea (Figure 1). Most areas in YRB belong to the subtropical monsoon climate zone with the average annual rainfall from 692 to 1611 mm and the average air temperature ranges from 9°C to 18°C (Zhang *et al.* 2019). Suitable climatic conditions have created a rich variety of vegetation types, and the differences in sea–land and elevation have resulted in many topographic features in the basin, such as mountains, plateaus, basins, hills, and plains. The large areas of plain and basin, as well as the rich water resource, have led to rapid industrial and agricultural development in YRB. Large cities in the basin, such as Shanghai, Nanjing, Wuhan, and Chongqing, have experienced rapid economic development in the past three decades, and urban expansion has brought about frequent land use modifications (Li *et al.* 2021). Human activities and climate change have threatened the unique ecological structure and have polluted water quality, which has led to the national policies of a 10-year ban on fishing and environmental remediation in the basin (Sun *et al.* 2017; Wu *et al.* 2021).

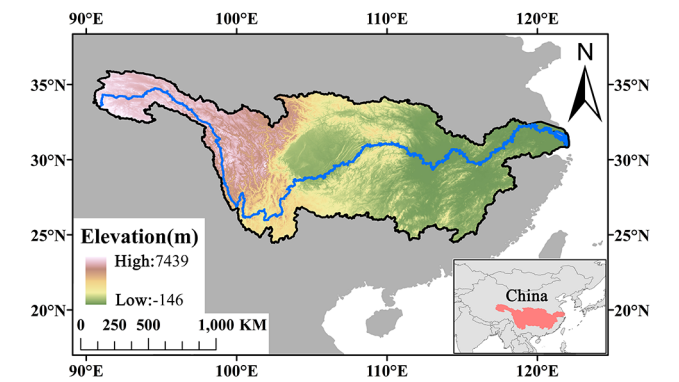

Figure 1. Study area of the Yangtze River basin.

Data

CLCD

The CLCD contains 30-m annual LULC in China from 1990 to 2019. CLCD's classification system includes nine major LULCs: cropland, forest, shrub, grassland, water, snow and ice, barren, impervious, and wetland. CLCD used sufficient training samples from combining stable samples extracted from China's land use/cover data sets and visually interpreted samples from satellite time-series data. The classification method was stable because they used spectrum, spectral index, phenology, and geographic location as input features to the RF classifier, and a postprocessing process was proposed incorporating spatial-temporal filtering and logical reasoning. The overall accuracy reached 79.31%, and two third-party verifications (Geo-Wiki and GLCVSS) achieved 54.57% and 65.46% accuracy, proving its superiority over similar products. The data of YRB were directly downloaded from https://doi.org/10.5281/zenodo.4417810, and the results in 2020 were obtained using the 2019 data as training.

Remote Sensing Data Sources

The GEE platform (https://earthengine.google.com) provides the Landsat data set of the U.S. Geological Survey (USGS, https://www.usgs.gov), and the Landsat surface reflectance data used in this study have conducted systematic atmospheric and terrain correction. Considering the quality of the Landsat data, we chose the Landsat 8 OLI data after 2013 and combined TM and ETM+ data before 2013. Images from June to September of each year were used to filter the production of training data. There are 157×8 Landsat scenes per year for the entire study area, and in practice, it will be less than this amount because of missing images. The Normalized Difference Vegetation Index (NDVI), Normalized Difference Built Index (NDBI), and Modified Normalized Difference Water Index (MNDWI) (Xu 2007; Szabó *et al.* 2016) are all calculated based on the original band, and elevation and slope are computed from digital elevation model (NASA Shuttle Radar Topography Mission Digital Elevation 30 m) data in GEE. The thematic-class products (GFC global forest change, GSW global surface water, and GISA global impervious surface area) are obtained on GEE and from http://irsip.whu.edu.cn. These thematic-class products are based on global Landsat data with a spatial resolution of 30 m with continuous updating. Among them, GISA uses a machine learning classification framework and postprocessing of luminous data to ensure the accuracy of the product. Similarly, GFC and GSW are calculated with the different spectral indices and fully take into account the influence of seasons.

Table 1. Definition of each category and sample distribution.

Class	Definition	Number
Cropland	Orchards and cropland, including paddy fields and dry fields	620
Forest	Forestry land used for growing trees and bamboo etc.	580
Shrub	Low shrubs and areas with low vegetation cover	137
Grass	All kinds of grasslands that grow mainly herbaceous plants, including shrub grassland and sparse forest grassland	102
Water	Land used for natural terrestrial waters and water conservancy facilities	680
Snow/ice	Land covered with snow year-round	140
Barren	Land that has not yet been used or that is difficult to use	304
Impervious	Urban and rural residential areas and other industrial, mining, and transportation land	496
Wetland	Land with flat and low-lying terrain, seasonal or year-round accumulation of water, and growing wet plants on the surface	146

Sample Data

The classification system in this article is the same as CLCD's classification system, including cropland, forest, shrub, grassland, water, snow and ice, barren, impervious, and wetland. Due to the excellent basis of CLCD, only a small number of samples are needed as training data. High-quality training and validation samples are evenly distributed in the study area and provided for supervised classification by combining the Google Earth HD map and GEE platform sample-making tools. In total, 1700 training samples and 1505 validation samples were selected independently in 1995, 2005, and 2015.

Anthropomorphic and Natural Data

Natural and social factors have a profound impact on LULC change. Seven major potential factors were selected in this study to test their impact on LULC change in YRB (Table 2), including population density (POP), gross domestic product (GDP), annual average precipitation (PRE), annual average temperature (TEM), net primary productivity (NPP), Normalized Difference Vegetation Index (NDVI), and digital elevation model (DEM). The data were downloaded from the Resource and Environmental Science Data Center of the Chinese Academy of Sciences (https://www.resdc.cn).

Method

The process was implemented on the GEE platform and ArcGIS, shown in Figure 2. First, the categories of forest, water, and impervious surface in CLCD were compared with GFC, GSW, and GISA data year by year to derive the disputed area. Then the Landsat data of the disputed area were used to reclassify by the RF classifier. Next, through using visually interpreted and third-party validation samples, the classification accuracy was calculated and compared to verify the reliability of our LULC results; LULC change is also analyzed by quantifying the individual changes and interconversions of each category. Finally, through the process of the time-series analysis of land use degree, we transformed the LULC categories into 5-year land use degree data, and the natural and social drivers are analyzed by using GTWR model on ArcGIS.

Table 2. Anthropomorphic and natural data*.

Data Name	Time	Spatial Resolution (m)
POP	1990, 1995, 2000, 2005, 2010, 2015	1000
GDP	1990, 1995, 2000, 2005, 2010, 2015	1000
PRE	1990, 1995, 2000, 2005, 2010, 2015	1000
TEM	1990, 1995, 2000, 2005, 2010, 2015	1000
NPP	2000, 2005, 2010	500
NDVI	1990, 1995, 2000, 2005, 2010, 2015	500
DEM	2000	30

POP= population density; GDP = gross domestic product; PRE = annual average precipitation; TEM = annual average temperature; NPP = net primary productivity; NDVI = Normalized Difference Vegetation Index; DEM = digital elevation model.

Data Processing and Classification

Image data sets and computing services on the GEE platform make the cloud removal process easy and efficient to execute by the CFmask algorithm (Zhu and Woodcock 2012). We selected data from June to September of each year because it is the vegetation growing season and the hydrological conditions are stable (Guo *et al.* 2008).

RF classification algorithm is used for processing large-scale and complex data (Belgiu and Drăguţ 2016) and has been widely used in LULC classification because it is good at overcoming the noise in the data and the overfitting problem of training (Na *et al.* 2010). Zhang *et al.* (2020) compared the contribution of the auxiliary feature vectors for RF classification in LULC studies (Zhang and Yang 2020) and showed that the accuracy of RF classification can be improved more by adding auxiliary feature vectors, such as spectral indices and elevation information. Taking into account the classification target category of this study and the physical geography of the study area, five auxiliary feature vectors (NDVI, MNDWI, NDBI, DEM, and slope) and the original spectral band are added as the input features to the RF classifier (Hoshikawa and Umezaki 2014). After experimental comparison, stable classification performance can be obtained when the number of decision trees of the RF classifier is set to 200.

Accuracy Assessment

To assess the accuracy of our results, we use a visually interpreted test set (1505 in total) and a third-party test set (Geo-Wiki) (4226 in total). Based on our results, the data (CLCD, GFC, GISA, and GSW) are verified to be very stable each year. The accuracy validation in 1995, 2005, and 2015 proves the stability of our products, which allows the comparison with other data products in 2015. In addition, we also validated our results with CLCD, FROM_GLC, and GLCFCS30 on the validation sample of Geo-Wiki. Furthermore, the accuracy of our results was validated by confusion matrixes, including producer's accuracy (PA), user's accuracy (UA), overall accuracy (OA), and kappa coefficients.

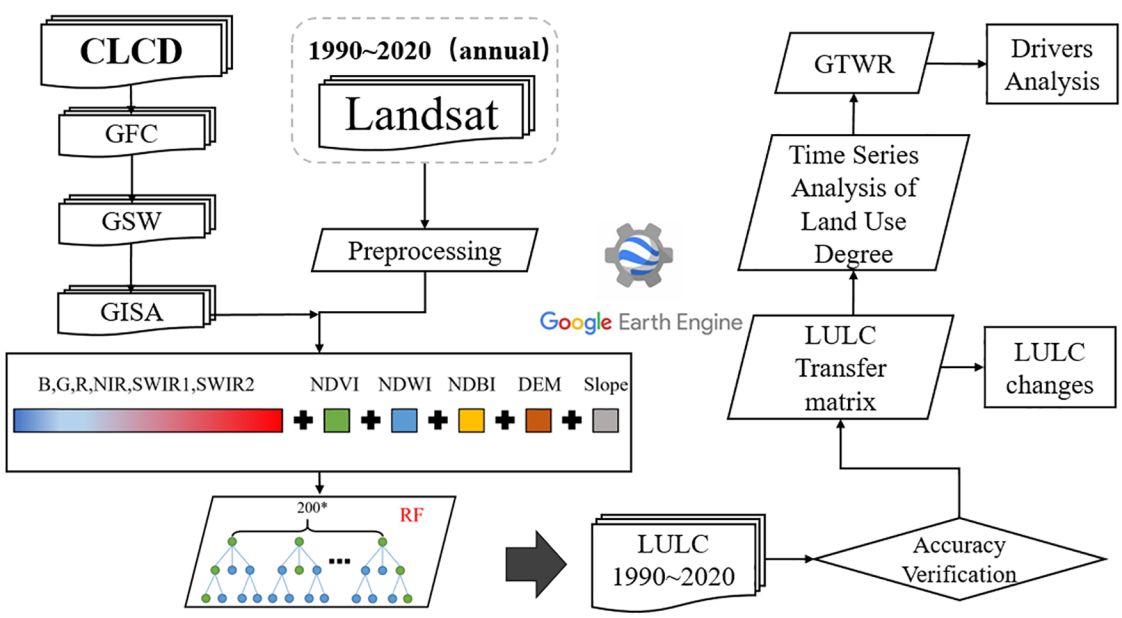

Figure 2. Methodology and flowchart.

Time-Series Model of Land Use Degree

The land use degree model is commonly used in LULC change analysis, which was developed from the original cropland use intensity model by Wang *et al.* (2010). Liu *et al.* (2020c) proposed a new quantitative analysis method for land use degree that has been applied in China (Liu *et al.* 2020c). This method divides the land use degree into four levels according to the balance state of the land cover under the influence of natural/social factors. The setting of the land use degree index is shown in Table 3.

The quantitative model of land use degree distinguishes the natural land cover and man-made land use by assigning different weight values to different land types so that the disordered LULC categories become orderly (Liu *et al.* 2020d). As shown in Figure 3, the LULC results within every 5 years (corresponding to the natural/social factors data) are considered as a whole. The land use degree indices over the five years are summed up to represent the overall contribution of different LULCs over the five years with reducing the effect of classification errors. In addition, our method provides more information when compared to the direct use of the land use index data for a single year since five to 20 indexes have more details than one to four indexes.

GTWR Model

The GTWR model is a classical model for the study of spatial heterogeneity in long time series. The GTWR model incorporates the time dimension into the geo-weighted regression model, which can obtain a better fit and make the estimation results more effective (Ma *et al.* 2018). Correlation calculations and multicollinearity tests are indispensable processes before being input into the GTWR model (Ran *et al.* 2019). Therefore, we calculated the Spearman correlation coefficients between the drivers and the land use degree data, which can respond to the degree of correlation between land use data and other spatial attribute data (Myers and Sirois 2004; Tran *et al.* 2010). In addition, due to different natural/social factors that exist with different temporal and spatial resolutions, the uniformization process is done before the correlation analysis. Finally, we select the factors with higher correlations and then exclude those with variance inflation factor (VIF) over 5 as dependent variables into the GTWR model. In this article, the base distance is set to the Chinese municipal administrative divisions of YRB considering the stability of the GTWR model. The GTWR model developed in this study depicts the quantitative spatial-temporal relationships of the LULC drivers, and its overall structure is described as follows:

$$y_i = \beta_0(u_i, v_i, t_i) + \sum_k \beta_k(u_i, v_i, t_i)\, x_{ik} + \varepsilon_i \tag{1}$$

where i (i = 1, 2, …, n) denotes a city region; the dependent variable y_i refers to the LUD for each city; x_{ik} represents the driver factors; u_i, v_i, t_i are the longitude, latitude, and time, respectively; β_0 is the intercept value; β_k denotes a set of parameter values; and is the random error.

Table 3. Classification values of land use degree.

Types of Land	Uncultivated Land	Ecological Land	Agricultural Land	Construction Land
LULC	Barren, snow	Forest, shrub, grassland, wetland and water	Cropland	Impervious, including urban, residential area, and traffic land
Index value	1	2	3	4

LULC = c.

Results and Analysis

Classification Results and Accuracy Assessment

Partial LULC results are shown in Figure 4, and the study area was dominated mainly by forest (46.23%), cropland (28.40%), and grassland (18.18%). As in Figure 4, most of the natural forests in the basin are located in the middle and upper parts. The Sichuan Basin, the Central Plain, and the Yangtze River delta plain are the main agricultural areas. The grassland, barren, and snow land are located in the alpine areas of the Qinghai-Tibet Plateau in China. The downstream is rich in water resources, and the cities are scattered, with the largest urban agglomeration in the Yangtze River delta, including Shanghai and Nanjing. Finally, most of the wetlands are located near Taihu Lake, Poyang Lake, and Dongting Lake.

Good accuracy of the LULC classification results is an important prerequisite for subsequent computational analysis. Based on the validation sample of visual interpretation in 1995, 2005, and 2015, the overall accuracy of this study reached 80%–83%, and the kappa coefficient of this study is about 0.79, which proves that the validation results are stable and reliable. For each category, forest, snow/ice, and barren have the highest classification accuracy of around 90%, while cropland, shrubs, water, impervious surface, and grassland are relatively high with all accuracy of above 70% as well. The classification of wetland categories has also improved considerably after our efforts and reached 60.71%, which makes up for the lack of other data in this area. In the comparison with CLCD, the accuracy of some categories of our product remains similar, while the accuracy in cropland, barren, impervious surface, and wetland are all improved. Therefore, our results have advantages and make up for the shortcomings of the other products.

To verify the effect of our method on CLCD enhancement, we intercepted part of the result of CLCD and this study, shown in Figure 5. It can be seen by comparison with the Google HD map that there is an obvious misclassification of mountain shadows into the water in CLCD (Figure 5d). By the method of this article (after intercomparison and reclassification with GSW), the misclassified part is completely removed. On the Google HD map in Figure 5b, we can see that there

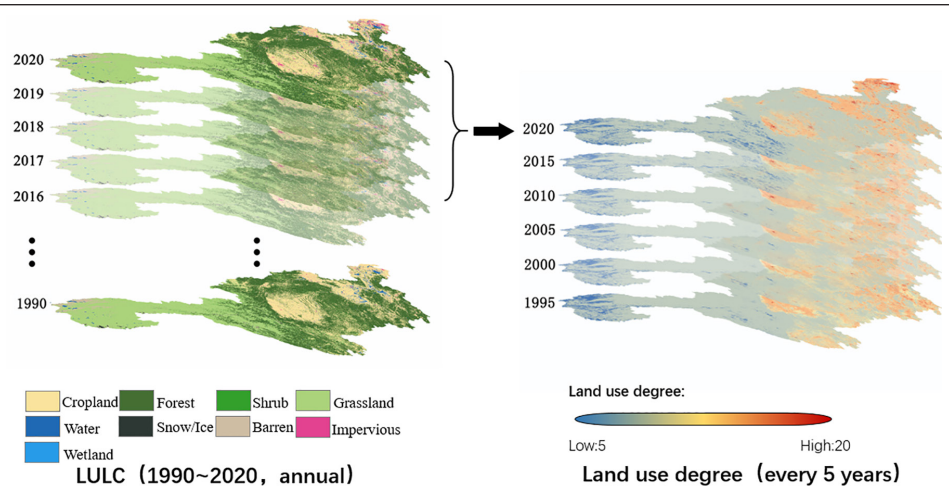

Figure 3. Time-series analysis of land use degree.

is a large intermittent wetland area that occurs during the dry seasons and is inundated during the wet seasons in the middle of the shoreline and the lake inundation area (Yang *et al.* 2020). This area was not well classified in the CLCD and was misclassified as cropland, which was partially corrected after our reclassification. However, it is still a bit flawed because some areas were not involved in the intercomparison, and, on the other hand, the spectral characteristics of wetlands are easily confused with the spectra of other land types (Mahdavi *et al.* 2018). Furthermore, by adding the sample of the exposed riverbed, it is also easy to see in Figure 5f that the area that was originally misclassified as impervious surface is well identified as barren. These comparisons show that our work has trustworthy accuracy and effectively improves the accuracy of CLCD in YRB.

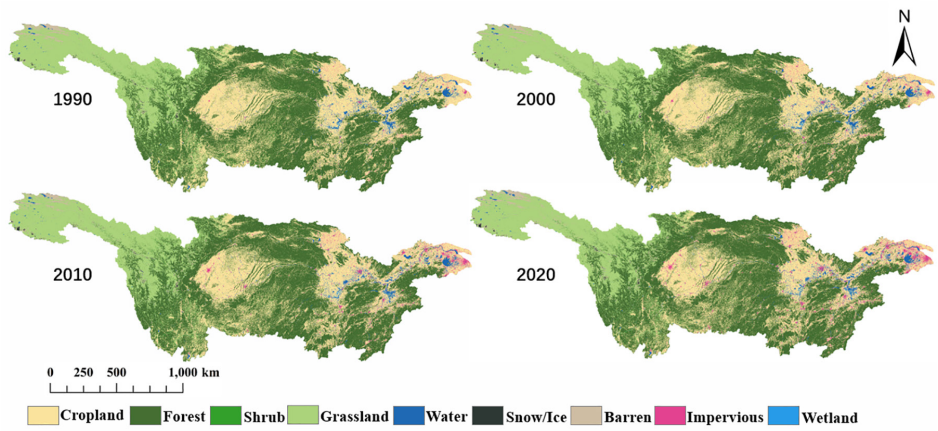

Figure 4. Land use and land cover mapping of the Yangtze River basin in 1990, 2000, 2010, and 2020.

Table 4. Validation of the results in this article based on visually interpreted test samples in 1995, 2005, and 2015.

	Cropland	Forest	Shrub	Grassland	Water	Snow/Ice	Barren	Impervious	Wetland	OA (%)
1995										
PA (%)	71.64	87.35	91.3	67.42	74.17	90.91	90.32	88.73	1	79.55
UA (%)	94.3	94.57	48.38	94.9	96.43	50	47.73	63	12.09	
2005										
PA (%)	80.39	86.95	89.29	70.1	76.16	95.24	91.59	85.86	96.67	82.31
UA (%)	93.45	96.38	40.32	94.91	93.57	50	55.68	85	31.87	
2015										
PA (%)	82.19	89.02	88	71.92	74.71	92	94.78	73.81	60.71	82.66
UA (%)	92.02	96.38	35.48	92.41	90.71	57.5	61.93	93	30.77	

PA = producer's accuracy; UA = user's accuracy; OA = overall accuracy.

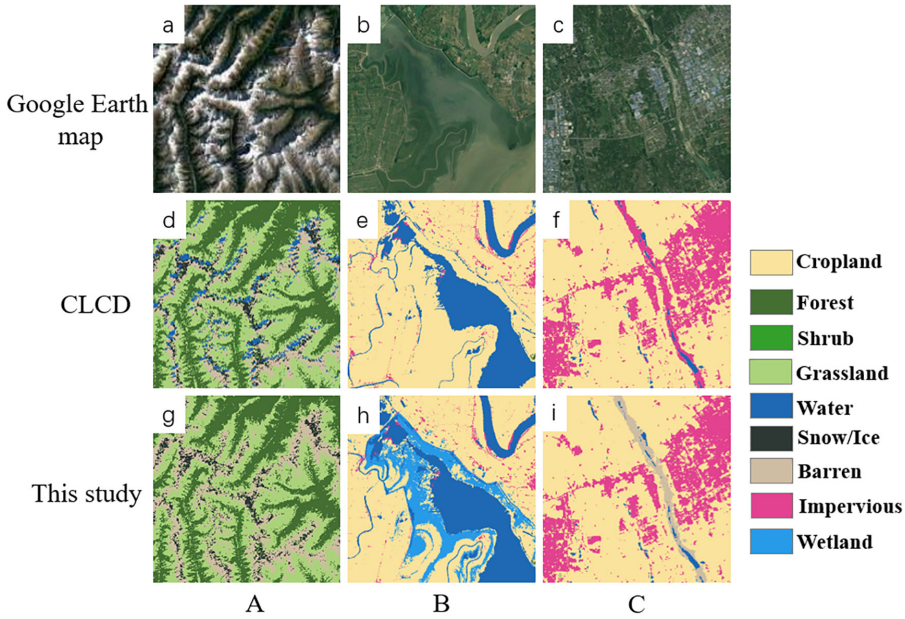

Figure 5. Google HD maps, China land cover data set (CLCD), and land use and land cover classification of this study.

Long-Time Spatial-Temporal Change Characteristics

The process and trend of LULC change are calculated for each category from 1990 to 2020 based on the LULC generated in this study (Figure 6). Impervious areas covered 4.28 million ha in 2020, sprawling unprecedentedly over the past 30 years and increasing more than three times relative to that in 1990, which is also consistent with GISA data. In general, impervious areas far exceed other categories in terms of the magnitude of change. Cropland area was dropped to 54.65 million ha in 2020 with a decrease of 6.12% when compared to 1990. The significant increase in forest land area by 4.04% (3.22 million ha) was due to China's positive response to the Grain for Green program (Robbins and Harrell 2014), especially in the middle and upper streams, while the lower stream remained stable (Xu *et al.* 2020). The area of surface water increased by 6.09% (0.2 million ha), especially after 1995, when the development of hydropower was proposed by the Ninth Five-Year Plan of China. The increasing reservoir and dam construction were some of the reasons accounting for the surface water extension (Ali *et al.* 2019). Barren declined slightly by about 9.00% until 1997, then trended steadily upward about 38.11% and grew significantly faster after 2015. After the adjustment, the area of the exposed riverbank upstream was classified in the barren category. YRB was flowing fast between 1990 and 2000, when a large amount of sediment was carried downstream by the current. With the construction of the water conservancy facilities afterward, the river flow velocity decreased, which reduced the amount of sand transported by the river (Chen *et al.* 2001). In particular, the completion of the Three Gorges Dam after 2015 caused more than 90% of the sediment to be retained in the upper basin of the Yangtze River (Yang *et al.* 2018), thus creating an elevated riverbed and increased barren. The wetlands have experienced dramatic changes (some of the fluctuations may also come from classification errors), with an increase of 0.03 million ha overall. The fragmentation of the wetland landscape in the basin is significant (Rui *et al.* 2017), and the construction of some wetland parks may account for some of the increase. Shrub decreased significantly by 50%, and the snow/ice land varied in a regular undulating pattern, covering an average of 0.33 million ha. Grassland continued to decline by 6.99% to 36.54 ha in 2020. Since grassland is located mainly on the Tibetan Plateau with less effect by human activities, the impact of climate change on vegetation in vulnerable areas is the main cause.

The years 1990, 2000, 2010, and 2020 are chosen to study the land transfer process, and 100 major transformations are selected to make Sankey diagrams (Figure 10). The vegetation cover area (forest, cropland, shrub, and grassland) remained largely unchanged over the years, but its internal transformations were frequent. There is a large mutual transfer of cropland and forestland, and large deforestation and afforestation occur during this time. Also, the imaging period error of the image itself and the different image quality (Landsat-8 has better image quality) have some influence. It can be observed that the main origin of impervious surface area growth is cropland, as is the case with water, which explains the decrease of cropland. This is due to the urban development that continues to occupy the surrounding cropland, and the policy of returning farmland to forests and lakes implemented in China is also a reason. The wetland area is small and relatively independent, and its transformation is not within the top 100, so it is not reflected in the figure.

Driving Force Analysis

LULC change is a complex process influenced by natural and social factors (Fox and Vogler 2005). In this article, the correlations between natural/social factors and land use degree were calculated with little overall fluctuation, and their average values are shown in Table 5. Among them, Correlation coefficients above 0.3 were considered to be relevant, while those above 0.6 were considered to be high. Then POP, TEM, PRE, and DEM were selected as independent variables input to the GTWR model because of the high correlation coefficients, where GDP was excluded due to its VIF value being greater than 5 in Table 6. Finally, our GTWR is set with land use degree as the dependent variable; POP, TEM, PRE, and DEM as the independent variables; the spatial dimension as the location of each municipality mass center; and the temporal dimensions as 1990, 1995, 2000, 2005, 2010, and 2015.

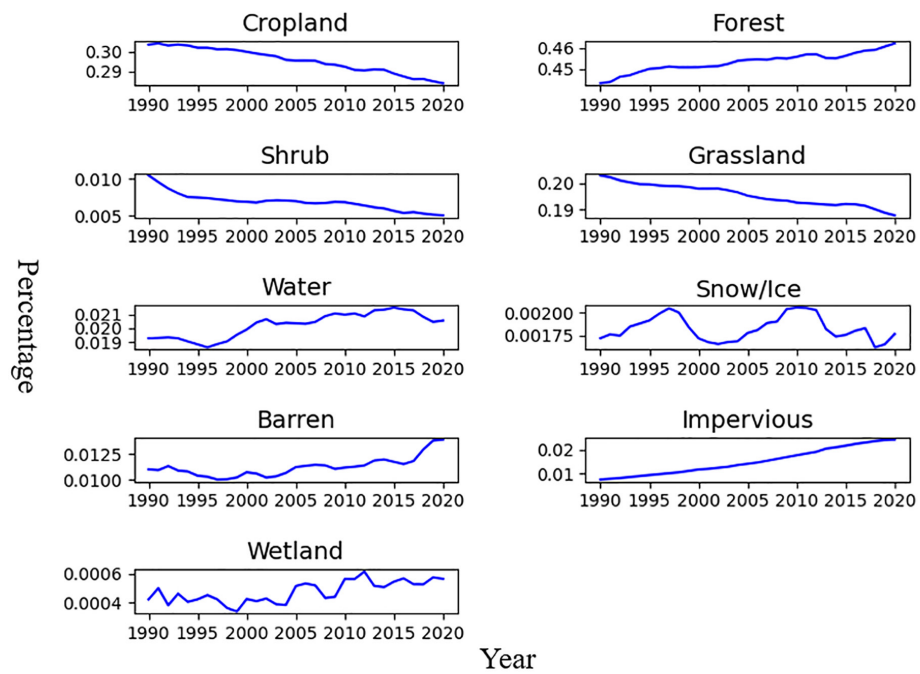

Figure 6. Statistics of land use and land cover changes in each class.

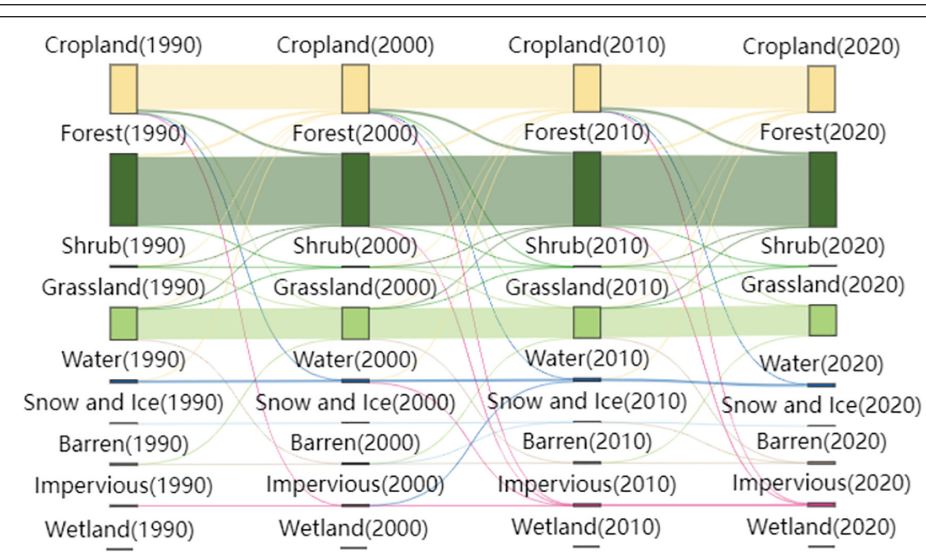

Figure 7. Sankey diagram of land use transfer flows from 1990 to 2020.

Table 5. Average of coefficients between all the factors.

	LUD	GDP	POP	NPP	TEM	PRE	NDVI	DEM
LUD								
GDP	0.58							
POP	0.63	0.93						
NPP	0.15	0.43	0.38					
TEM	0.51	0.77	0.78	0.45				
PRE	0.33	0.52	0.52	0.44	0.64			
NDVI	0.04	0.01	−0.06	0.04	0.01	−0.20		
DEM	−0.57	−0.84	−0.84	−0.44	−0.87	−0.60	−0.03	

LUD = Land use degree; GDP = gross domestic product; POP = population density; NPP = net primary productivity; TEM = annual average temperature; PRE = annual average precipitation; NDVI = Normalized Difference Vegetation Index; DEM = digital elevation model. The *p*-values for all significance tests are much less than 0.001.

Table 6. Variance inflation factor validation for different factors.

Factors	GDP	POP	NPP	TEM	PRE	NDVI	DEM
VIF	5.04	3.81	1.13	1.15	2.82	1.04	2.95

GDP = gross domestic product; POP = population density; NPP = net primary productivity; TEM = annual average temperature; PRE = annual average precipitation; NDVI = Normalized Difference Vegetation Index; DEM = digital elevation model; VIF = variance inflation factor.

We finally obtained a GTWR model with a goodness of fit of 0.91, an Akaike information criterion of 1281.36, and a spatial-temporal distance ratio of 0.2688. After a comparison of goodness of fit, the model outperformed the geographically weighted regression model (0.81) and the ordinary least squares model (0.79).

Using the university kriging interpolation, the GTWR fitting results are presented visually, and the coefficients of the respective variables are selected for the earliest year (1990) and the latest year (2015), as shown in Figure 8. From the distribution of POP coefficient values, we can see that human activity plays a driving role in the LULC of YRB, being the most obvious especially in the middle region, and the no-man's-land in the highland region can be disregarded. This result is also consistent with the results of the driving analysis of LULC changes in the Savannah River and Muga watersheds (Zurqani *et al.* 2018; Belay and Mengistu 2019). Meanwhile, natural factors also have a strong influence on LULC changes by affecting the growth of natural vegetation (Hu and Hu 2019). The DEM, on the contrary, is negatively correlated with land use degree in YRB, indicating that the plains at low elevation are suitable for land development and utilization, while the higher the elevation is, the more difficult it is to develop the area. However, the effect of PRE on land use degree is more complex, with a large amount of rainfall occurring in the middle and lower reaches of YRB, so, on the one hand, PRE explains well the development of urban areas in the middle and lower reaches, while, on the other, the forested land with lower land use degree within these areas shows a negative drive. The TEM shows an overall positive drive, but there is some counter-drive in the downstream and mid-basin regions, and the negative drive has expanded in the mid-basin.

Discussion

Accuracy Comparison with Other LULC Products

To better validate the accuracy of our results, we intercompared with CLCD, FROM_GLC, and GLCFCS30 using the Geo-Wiki validation samples. Since Geo-Wiki does not include water and wetland in the validation points of YRB, we excluded the statistics of these two in the table. As with the visual interpretation sample validation, the overall accuracy of our results in Geo-Wiki was higher than that of the other three products (CLCD: 57.91%; FROM_GLC: 54.76%; GLCFCS30: 52.72%) at 62.45%. In general, it appears that the accuracy of our results is better than that of the other products in all categories. Although

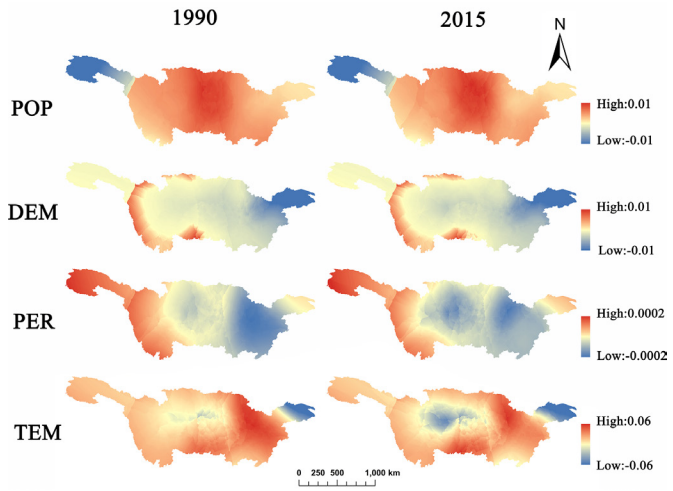

Figure 8. Coefficient distributions of the respective variables in the geographically and temporally weighted regression model.

the accuracy is lacking in shrubs and grasses, it is still excellent when compared to FROM_GLC and GLCFCS30.

Trends in LULC Change

Landsat images in 1990 and 2020 were selected and did change area coloring to highlight the change areas and to show the trends of LULC changes in YRB. As shown in Figure 9, five typical LULC changes are compared. Figure 9A illustrates the urban expansion of Shanghai, which has tripled in size in 20 years, with the rapid expansion of its main urban area and surrounding satellite cities taking over areas of previously cropland. Figure 9B shows the rapid development of fisheries around Chaohu Lake, which is an important component of the new cropland. Figure 9C illustrates the open-pit mines from 2011 and shows the spatial detail at the 30-m resolution scale. Figure 9D is the transformation of cropland in the bend of the Yangtze River, which occupies the original mudflats and wetlands. Figure 9E shows the increase in water surface area upstream of the dam before and after the Three Gorges Water Conservancy Project.

Limitations and Future Work

With the GEE platform, we made improvements to the CLCD in YRB using three thematic products (GFC, GISA, and GSW). This method has been proven to greatly reduce the workload when compared to retraining the classifier for the whole basin and to obtain good

Table 7. Comparison of mapping accuracy based on Geo-Wiki test samples for this study, CLCD, FROM_GLC, and GLCFCS30.

	Geo-Wiki							
	Cropland	Forest	Shrub	Grassland	Snow/ Ice	Barren	Impervious	OA (%)
	This study							
PA (%)	60.65	72.86	33.33	25.33	100	72.72	69.15	62.45
UA (%)	76.50	84.33	2.17	28.02	3.85	2.95	51	
	CLCD							
PA (%)	58.83	68.93	33.33	25.32	100	72.72	65.90	57.81
UA (%)	78.99	82.61	2.45	29.67	3.84	3.21	49.57	
	FROM_GLC							
PA (%)	62.24	66.57	11.11	18.46	100	50	61.71	54.76
UA (%)	54.02	79.86	4.80	28.99	1.92	11.44	41.5	
	GLCFCS30							
PA (%)	45.71	73.06	5.88	19.60	66.67	75	60.12	52.72
UA (%)	70.41	64.49	0.44	30.82	3.85	4.46	49	

CLCD = China land cover data set; OA = overall accuracy; PA = producer's accuracy; UA = user's accuracy.

accuracy. However, CLCD data are missing for products from 1986 to 1989 due to the commercial preorder acquisition plan of Landsat 5 before 1990, which further limited its availability in China before 1990 (Loveland and Dwyer 2012). In addition, based on the higher classification accuracy of the results in this article, we derived a more credible land distribution and change in YRB from 1990 to 2020. However, some driver data are not openly available, which will be the main work of our next study. In general, in the future, we would like to complement and expand the pre-1990 LULC products by combining other sensor data and collect more detailed driving factors to deeply understand the driving forces of LULC changes in YRB.

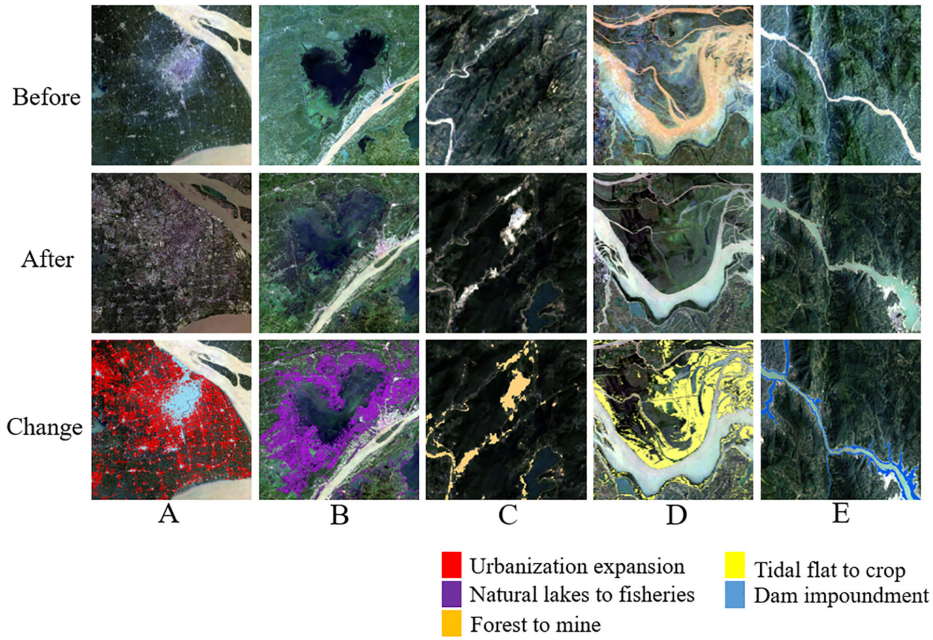

Figure 9. Land use and land cover change sample of the Yangtze River basin.

Conclusions

The YRB is of great ecological and economic significance to China. Continuous and accurate LULC mapping of YRB is important for both fine-resolution monitoring and sustainable development within the basin, and it is also a basic parameter for studying the ecological environment and climate change in the basin. In this article, we propose an optimization algorithm based on the open-access CLCD data set and produce annual 30-m LULC maps of YRB from 1990 to 2020. The results show an improvement of accuracy of about 82.66%, which is higher than CLCD's 77.21% and two other global LULC products. Similarly, in the third-party validation sample, Geo-Wiki, the results of this article also achieved higher precision when compared to the other three LULC products. In addition, the LULC changes dramatically in YRB between 1990 and 2020. The impervious surface has more than tripled, and cropland is decreasing and converting to the impervious surface, forestland, and water. Using the GTWR model, we found that anthropogenic activities play an important role in driving LULC change within YRB, while natural factors do the opposite, with both DEM and PRE factors limiting the improvement of land use degree. Therefore, it is necessary to develop a rational way for sustainable development. Finally, the annual 30-m LULC data from 1990 to 2020 in this article will be well combined with hydrological data for deeper exploration of the environment and climate change for YRB.

Acknowledgments

This work was supported by the Strategic Priority Research Program Project of the Chinese Academy of Sciences under grant XDA23040100, the Jiangsu Natural Resources Development Special Project under grant JSZRHYKJ202002, and the Shanghai Leading Talent Project under grant E056061. The data used in this study are available in Science Data Bank at https://www.scidb.cn/s/nIrqUf (doi:10.11922/sciencedb.j00116.00008).

References

Ali, R., A. Kuriqi, S. Abubaker and O. Kisi. 2019. Hydrologic alteration at the upper and middle part of the Yangtze River, China: Towards sustainable water resource management under increasing water exploitation. *Sustainability* 11(19):5176..

Belay, T. and D. A. Mengistu. 2019. Land use and land cover dynamics and drivers in the Muga watershed, Upper Blue Nile basin, Ethiopia. *Remote Sensing Applications: Society and Environment* 15:100249.

Belgiu, M. and L. Drăguţ. 2016. Random forest in remote sensing: A review of applications and future directions. *ISPRS Journal of Photogrammetry and Remote Sensing* 114:24–31.

Chen, J., J. Chen, A. Liao, X. Cao, L. Chen, X. Chen, C. He, G. Han, S. Peng, M. Lu, W. Zhang, X. Tong and J. Mills. 2015. Global land cover mapping at 30m resolution: A POK-based operational approach, *ISPRS Journal of Photogrammetry and Remote Sensing* 103:7–27.

Chen, T., M. Li, L. Luo, S. Deng, R. Zhou and D. Chen. 2020. Simulating the effects of land urbanization on regional meteorology and air quality in Yangtze River Delta, China. *Applied Geography* 120:102228.

Chen, Z., J. Li, H. Shen and W. Zhanghua. 2001. Yangtze River of China: Historical analysis of discharge variability and sediment flux. *Geomorphology* 41(2–3):77–91.

Findell, K. L., A. Berg, P. Gentine, J. P. Krasting, B. R. Lintner, S. Malyshev, J. A. Santanello Jr and E. Shevliakova. 2017. The impact of anthropogenic land use and land cover change on regional climate extremes. *Nature Communications* 8(1):989.

Foley, J. A., R. DeFries, G. P. Asner, C. Barford, G. Bonan, S. R. Carpenter, F. S. Chapin, M. T. Coe, G. C. Daily and H. K. Gibbs. 2005. Global consequences of land use. *Science* 309(5734):570–574.

Fox, J. and J. B. Vogler. 2005. Land-use and land-cover change in montane mainland southeast Asia. *Environmental Management* 36(3):394–403.

Gibbard, S., K. Caldeira, G. Bala, T. J. Phillips and M. Wickett. 2005. Climate effects of global land cover change. *Geophysical Research Letters* 32(23):1–4.

Gong, P., J. Wang, L. Yu, Y. Zhao, Y. Zhao, L. Liang, Z. Niu, X. Huang, H. Fu and S. Liu. 2013. Finer resolution observation and monitoring of global land cover: First mapping results with Landsat TM and ETM+ data. *International Journal of Remote Sensing* 34(7):2607–2654.

Gorelick, N., M. Hancher, M. Dixon, S. Ilyushchenko, D. Thau and R. Moore. 2017. Google Earth Engine: Planetary-scale geospatial analysis for everyone. *Remote Sensing of Environment* 202:18–27.

Guo, H., Q. Hu and T. Jiang. 2008. Annual and seasonal streamflow responses to climate and land-cover changes in the Poyang Lake basin, China. *Journal of Hydrology* 355(1–4):106–122.

Haddeland, I., J. Heinke, H. Biemans, S. Eisner, M. Florke, N. Hanasaki, M. Konzmann, F. Ludwig, Y. Masaki, J. Schewe, T. Stacke, Z. D. Tessler, Y. Wada and D. Wisser. 2014. Global water resources affected by human interventions and climate change. *Proceedings of the National Academy of Sciences* 111(9):3251–3256.

Hansen, M. C., P. V. Potapov, R. Moore, M. Hancher, S. A. Turubanova, A. Tyukavina, D. Thau, S. V. Stehman, S. J. Goetz and T. R. Loveland. 2013. High-resolution global maps of 21st-century forest cover change. *Science* 342(6160):850–853.

Hoshikawa, K. and M. Umezaki. 2014. Effects of terrain-induced shade removal using global DEM data sets on land-cover classification. *International Journal of Remote Sensing* 35(4):1331–1355.

Houghton, R. A., J. I. House, J. Pongratz, G. R. van der Werf, R. S. DeFries, M. C. Hansen, C. Le Quéré and N. Ramankutty. 2012. Carbon emissions from land use and land-cover change. *Biogeosciences* 9(12):5125–5142.

Hu, Y. and Y. Hu. 2019. Land cover changes and their driving mechanisms in Central Asia from 2001 to 2017 supported by Google Earth Engine. *Remote Sensing* 11(5):554.

Huang, B., B. Wu and M. Barry. 2010. Geographically and temporally weighted regression for modeling spatio-temporal variation in house prices. *International Journal of Geographical Information Science* 24(3):383–401.

Huang, X., J. Li, J. Yang, Z. Zhang, D. Li and X. Liu. 2021. 30 m global impervious surface area dynamics and urban expansion pattern observed by Landsat satellites: From 1972 to 2019. *Science China Earth Sciences* 64(11):1922–1933.

Jin, S. and T. Zhang. 2016. Terrestrial water storage anomalies associated with drought in southwestern USA from GPS observations. *Surveys in Geophysics* 37(6):1139–1156.

Li, W., L. Li, J. Chen, Q. Lin and H. Chen. 2021. Impacts of land use and land cover change and reforestation on summer rainfall in the Yangtze River basin. *Hydrology and Earth System Sciences* 25(8):4531–4548.

Liu, C., W. Li, G. Zhu, H. Zhou, H. Yan and P. Xue. 2020d. Land use/land cover changes and their driving factors in the northeastern Tibetan Plateau based on geographical detectors and Google Earth Engine: A case study in Gannan Prefecture. *Remote Sensing* 12(19):3139.

Liu, D., N. Chen, X. Zhang, C. Wang and W. Du. 2020a. Annual large-scale urban land mapping based on Landsat time series in Google Earth Engine and OpenStreetMap data: A case study in the middle Yangtze River basin. *ISPRS Journal of Photogrammetry and Remote Sensing* 159:337–351.

Liu, H., P. Gong, J. Wang, N. Clinton, Y. Bai and S. Liang. 2020b. Annual dynamics of global land cover and its long-term changes from 1982 to 2015. *Earth System Science Data* 12(2):1217–1243.

Liu, H., M. Zheng, J. Liu and X. Zheng. 2020c. Sustainable land use in the trans-provincial marginal areas in China. *Resources, Conservation and Recycling* 157:104783.

Liu, J., W. Kuang, Z. Zhang, X. Xu, Y. Qin, J. Ning, W. Zhou, S. Zhang, R. Li and C. Yan. 2014. Spatiotemporal characteristics, patterns, and causes of land-use changes in China since the late 1980s. *Journal of Geographical Sciences* 24(2):195–210.

Loveland, T. R. and J. L. Dwyer. 2012. Landsat: Building a strong future. *Remote Sensing of Environment* 122:22–29.

Ma, X., J. Zhang, C. Ding and Y. Wang. 2018. A geographically and temporally weighted regression model to explore the spatiotemporal influence of built environment on transit ridership. *Computers, Environment and Urban Systems* 70:113–124.

Mahdavi, S., B. Salehi, J. Granger, M. Amani, B. Brisco and W. Huang. 2018. Remote sensing for wetland classification: A comprehensive review. *GIScience and Remote Sensing* 55(5):623–658.

Myers, L. and M. J. Sirois. 2004. Spearman correlation coefficients, differences between. In *Encyclopedia of Statistical Sciences*, edited by Myers, L. and M. J. Sirois., 1–2. New York: Wiley.

Na, X., S. Zhang, X. Li, H. Yu and C. Liu. 2010. Improved land cover mapping using random forests combined with Landsat thematic mapper imagery and ancillary geographic data. *Photogrammetric Engineering and Remote Sensing* 76(7):833–840.

Pekel, J. F., A. Cottam, N. Gorelick and A. S. Belward. 2016. High-resolution mapping of global surface water and its long-term changes. *Nature* 540(7633):418–422.

Qu, L. A., M. Li, Z. Chen and J. Zhi. 2021. A modified self-adaptive method for mapping annual 30-m land use/land cover using Google Earth Engine: A case study of Yangtze River Delta. *Chinese Geographical Science* 31(5):782–794.

Ran, Q., Y. Hao, A. Xia, W. Liu, R. Hu, X. Cui, K. Xue, X. Song, C. Xu, B. Ding and Y. Wang. 2019. quantitative assessment of the impact of physical and anthropogenic factors on vegetation spatial-temporal variation in northern Tibet. *Remote Sensing* 11(10):1183.

Robbins, A. S. and S. Harrell. 2014. Paradoxes and challenges for China's forests in the reform era. *China Quarterly* 218:381–403.

Rui, S., P. Yao, W. Wen, B. Yue and L. Gang. 2017. Assessment of wetland ecosystem health in the Yangtze and Amazon River Basins. *International Journal of Geo-Information* 6(3):81.

Sulla-Menashe, D., J. M. Gray, S. P. Abercrombie and M. A. Friedl. 2019. Hierarchical mapping of annual global land cover 2001 to present: The MODIS Collection 6 Land Cover product. *Remote Sensing of Environment* 222:183–194.

Sun, R., P. Yao, W. Wang, B. Yue and G. Liu. 2017. Assessment of wetland ecosystem health in the Yangtze and Amazon River Basins. *ISPRS International Journal of Geo-Information* 6(3):81.

Szabó, S., Z. Gácsi and B. Balázs. 2016. Specific features of NDVI, NDWI and MNDWI as reflected in land cover categories. *Landscape and Environment* 10(3–4):194–202.

Tran, C. P., R. W. Bode, A. J. Smith and G. S. Kleppel. 2010. Land-use proximity as a basis for assessing stream water quality in New York State (USA). *Ecological Indicators* 10(3):727–733.

Vorosmarty, C. J., P. B. McIntyre, M. O. Gessner, D. Dudgeon, A. Prusevich, P. Green, S. Glidden, S. E. Bunn, C. A. Sullivan, C. R. Liermann and P. M. Davies. 2010. Global threats to human water security and river biodiversity. *Nature* 467(7315):555–561.

Wang, S. -Y., J. -S. Liu, and T. -B. Ma. 2010. Dynamics and changes in spatial patterns of land use in Yellow River Basin, China. *Land Use Policy* 27(2):313–323.

Wu, J., S. Zeng, L. Yang, Y. Ren and J. Xia. 2021. Spatiotemporal characteristics of the water quality and its multiscale relationship with land use in the Yangtze River Basin. *Remote Sensing* 13(16):3309.

Xu, H. 2007. Modification of normalised difference water index (NDWI) to enhance open water features in remotely sensed imagery. *International Journal of Remote Sensing* 27(14):3025–3033.

Xu, L., G. Yu, Z. Tu, Y. Zhang and N. E. Tsendbazar. 2020. Monitoring vegetation change and their potential drivers in Yangtze River Basin of China from 1982 to 2015. *Environmental Monitoring and Assessment* 192(10):642.

Yang, H. F., S. L. Yang, K. H. Xu, J. D. Milliman, H. Wang, Z. Yang, Z. Chen and C. Y. Zhang. 2018. Human impacts on sediment in the Yangtze River: A review and new perspectives. *Global and Planetary Change* 162:8–17.

Yang, H., X. Zhong, S. Deng and H. Xu. 2021b. Assessment of the impact of LUCC on NPP and its influencing factors in the Yangtze River basin, China. *Catena* 206:105542.

Yang, H. F., S. L. Yang, K. H. Xu, J. D. Milliman, H. Wang, Z. Yang, Z. Chen and C. Y. Zhang. 2018. Human impacts on sediment in the Yangtze River: A review and new perspectives. *Global and Planetary Change* 162:8–17.

Yang, J. and X. Huang. 2021. The 30 m annual land cover dataset and its dynamics in China from 1990 to 2019. *Earth System Science Data* 13(8):3907–3925.

Yang, L., L. Wang, D. Yu, R. Yao, Q. He, S. Wang and L. Wang. 2020. Four decades of wetland changes in Dongting Lake using Landsat observations during 1978–2018. *Journal of Hydrology* 587:124954.

Yang, S. L., K. H. Xu, J. D. Milliman, H. F. Yang and C. S. Wu. 2015. Decline of Yangtze River water and sediment discharge: Impact from natural and anthropogenic changes, *Scientific Reports* 5:12581.

Yang, S. L., J. Zhang, J. Zhu, J. P. Smith, S. Dai, A. Gao and P. Li. 2005. Impact of dams on Yangtze River sediment supply to the sea and delta intertidal wetland response. *Journal of Geophysical Research: Earth Surface* 110(F3):1–12.

Yang, X., F. Meng, P. Fu, Y. Zhang and Y. Liu. 2021a. Spatiotemporal change and driving factors of the eco-environment quality in the Yangtze River Basin from 2001 to 2019. *Ecological Indicators* 131:108214.

Zhang, D., X. Liu and P. Bai. 2019. Assessment of hydrological drought and its recovery time for eight tributaries of the Yangtze River (China) based on downscaled GRACE data. *Journal of Hydrology* 568:592–603.

Zhang, F. and X. Yang. 2020. Improving land cover classification in an urbanized coastal area by random forests: The role of variable selection. *Remote Sensing of Environment* 251:112105.

Zhang, X., L. Liu, X. Chen, Y. Gao, X. Xie and J. Mi. 2021. GLC_FCS30: Global land-cover product with fine classification system at 30 m using time-series Landsat imagery. *Earth System Science Data* 13(6):2753–2776.

Zhu, Z. and C. E. Woodcock. 2012. Object-based cloud and cloud shadow detection in Landsat imagery. *Remote Sensing of Environment* 118:83–94.

Zhu, Z., M. A. Wulder, D. P. Roy, C. E. Woodcock, M. C. Hansen, V. C. Radeloff, S. P. Healey, C. Schaaf, P. Hostert, P. Strobl, J. -F. Pekel, L. Lymburner, N. Pahlevan and T. A. Scambos. 2019. Benefits of the free and open Landsat data policy. *Remote Sensing of Environment* 224:382–385.

Zurqani, H. A., C. J. Post, E. A. Mikhailova, M. A. Schlautman and J. L. Sharp. 2018. Geospatial analysis of land use change in the Savannah River Basin using Google Earth Engine. *International Journal of Applied Earth Observation and Geoinformation* 69:175–185.

IN-PRESS ARTICLES

Bhaskar Dubey, B. Kartikeyan. A novel residual attitude estimation approach using georeferenced satellite imagery.

Edmond Lo, En-Kai Lin, Velautham Daksiya, Kuo-Shih Shao, Yi-Rung Chuang, Tso-Chien Pan. Efficient Building Inventory Extraction from Satellite Imagery for Megacities.

Xiaohua Li, Zhaolin Duan, Hao Chen, Jiliu Zhou, Professor, Yuan Wang. A Semi-Supervised Learning Method for Hyperspectral Image Open Set Classification.

Fei Yang, Jun Li, Tianyu Guo, Chengye Zhang, Xiao Sang. The fractional vegetation cover (FVC) and associated driving factors modelling in mining areas.

Sunil Kumar Pundir, Rahul Dev Garg. Development of technique for Vehicle specific off-road trafficability assessment using soil cone index, water index & geospatial data.

Weidong Li, Fanqian Meng, Yongbo Yu. The use of indices and modified U-Net network in improving the classification of planting structures.

Weiwei Liu. Managing earth hazards using deep reinforcement learning algorithm for industrial IoT network.

Itiya Aneece, Prasad S. Thenkabail. New generation hyperspectral sensors DESIS and PRISMA provide improved agricultural crop classifications.

Yanzhe Shi, Yumin Tan, Yunxin Li, Bo Xu. Automatic registration method of multi-source point clouds based on building facades matching in urban scenes.

A Boundary-Based Ground-Point Filtering Method for Photogrammetric Point-Cloud Data

Seyed Mohammad Ayazi and Mohammad SaadatSeresht

Abstract

Ground-point filtering from point-cloud data is an important process in remote sensing and the photogrammetric map-production line, especially in generating digital elevation models from airborne lidar and aerial photogrammetric point-cloud data. In this article, a new and simple boundary-based method is proposed for ground-point filtering from the photogrammetric point-cloud data. The proposed method uses the local height difference to extract the boundaries of objects. Then the extracted boundary points are traced to generate polygons around the borders of any objects on the ground. Finally, the points located inside these polygons, which are classified as non-ground points, are filtered. The experimental results on the photogrammetric point cloud show that the proposed method can adapt to complex environments. The total error of the proposed method is about 8.96%, which is promising in these challenging data sets. Moreover, the proposed method is compared with cloth simulation filtering, multi-scale curvature classification, and gLiDAR methods and gives better results.

Introduction

Ground-point filtering is an important step for generating a digital elevation model from a point cloud. Having a digital elevation model is a prerequisite for many application, including urban planning, 3D change detection, land use classification, and object extraction (Shan and Toth 2018). Currently, lidar and optical images are mostly used to generate point clouds, which are called lidar and image-based point clouds, respectively. Usually, a lidar point cloud contains the first and last pulses with sharp discontinuities around the borders of 3D objects (Axelsson 2000). However, an image-based point cloud contains only a single response for each position, with a smoothing effect around the borders of 3D objects. Most existing point-cloud filtering methods are developed for lidar point clouds. However, there are a few methods focused on image-based point clouds (Serifoglu Yilmaz *et al.* 2018; Zeybek and Şanlıoğlu 2019).

The current ground-point cloud filtering methods can be divided into four categories: morphological filtering methods, surface-based methods, slope-based methods, and machine-learning methods. Each of them solves a specific point-cloud filtering challenge. These challenges include the study-area type (flat, relief, or mountainous), object size, the height difference, object type (constructed or natural), and point density (Shan and Toth 2018).

The first category is mathematical morphological filtering methods on a lidar point cloud (Chen *et al.* 2007; Li *et al.* 2013; Pingel *et al.* 2013; Hui *et al.* 2016). The basic operations in these methods include opening, dilation, and erosion, or a combination of them. These methods can perfectly remove non-ground objects in flat areas, but they are sensitive to object size in relief or mountainous areas. Sometimes these methods remove small hills when the structure element selected is larger than the hill size. As an alternative to basic morphological methods, the geodesic dilation method (Arefi and Hahn 2005) can solve the problem of window size. Although geodesic dilation works well in lidar point clouds with all area types, it does not work well for non-sharp 3D objects such as buildings and trees in photogrammetric point clouds. In addition, morphological filtering methods do not work well in photogrammetric point clouds from large forest areas. Particularly if these forest areas are located in mountainous areas, the ground-point filtering challenges are intensified.

An alternative approach for ground-point cloud filtering is surface-based methods. These methods—such as the triangulated irregular network (TIN) model (Axelsson 2000; Shi *et al.* 2018), the active shape model (Elmqvist 2002), weighted iterative least-squares interpolation (Qin *et al.* 2017), thin plate spline (Cheng *et al.* 2019), and the cloth simulation model (W. Zhang *et al.* 2016)—extract the ground points by approximating the bare earth using a parametric surface. Generally, these methods select or extract ground seed points. Then these points are iteratively densified to generate a DEM, which gradually refines the ground surface by using a certain threshold. These methods depend on the size of the grid for selecting ground seed points and the angle thresholds for grouping other ground points. However, object size affects the performance of these methods. In order to obtain the ground surface, the grid size used must be larger than the object size. Although surface-based methods are suitable for forest areas, they fail in photogrammetric point clouds due to the lack of last pulses for selecting the lowest pulses.

The second alternative solution for ground-point cloud filtering is slope-based methods (Vosselman 2000). For identifying ground points (low points) and non-ground points (high points), these methods use the local height differences of adjacent points. Accordingly, Sithole and Vosselman (2001) improved them by applying a certain threshold for terrain slopes. In addition, Meng *et al.* (2009) used a slope-based method for selecting adjacent points by selecting the direction of the scanning. These methods do not work well with low-density point clouds, smooth objects, or steep terrains.

Another alternative approach for separating non-ground points from ground points is the application of machine learning. Support vector machines, random forests, and artificial neural networks have been used for this task (Chehata *et al.* 2009; Niemeyer *et al.* 2012; J. Zhang *et al.* 2013). Recently, deep-learning methods have been developed for point-cloud filtering (Hu and Yuan 2016; Gevaert *et al.* 2018; Rizaldy *et al.* 2018; Jin *et al.* 2020). Although these machine-learning methods have good outcomes in lidar point clouds, they are not generalizable for photogrammetric point clouds. Moreover, deep-learning methods require big data sets with different area types as well as a large variety of 3D objects; however, such data sets are not available for photogrammetric point clouds.

Generally, ground-point cloud filtering methods have been found promising in lidar point clouds but have not yet been sufficiently developed for photogrammetric point clouds. Particularly, challenges such as mountainous areas, large forests, and a lack of the last pulse have led to the failure of most existing methods in filtering ground points from photogrammetric point clouds. In this article, a new boundary-based method is presented for ground-point filtering from photogrammetric

Seyed Mohammad Ayazi and Mohammad SaadatSeresht are with the School of Surveying and Geospatial Engineering, College of Engineering, University of Tehran, Tehran, Iran (msaadat@ut.ac.ir).

Contributed by Zhenfeng Shao, October 8, 2021 (sent for review March 24, 2022; reviewed by Nana Yaw Danquah Twumasi and Junhak Lee).

Photogrammetric Engineering & Remote Sensing
Vol. 88, No. 9, September 2022, pp. 583–591.
0099-1112/22/583–591

doi: 10.14358/PERS.21-00084R2

point clouds. This method can be classified as a slope-based method. The proposed method can filter non-ground points in a complex mountainous data set, whereas most previous methods cannot completely filter non-ground points from a photogrammetric point cloud.

The Proposed Method

Overview

This article presents a new boundary-based method for filtering ground points from photogrammetric point clouds. Figure 1 illustrates the workflow of the proposed method. The proposed method assumes that there is a height jump (step) between ground points and non-ground points in a certain local neighborhood. In addition, this method removes the noises from the point cloud in the preprocessing step. In the next step, the proposed method computes the appropriate dimensions of a window which will move over all the points to find neighborhood points. After the window size is obtained, neighboring points are selected to compute the height differences. Higher points are labeled as object points (trees and buildings, among others). This process classifies only the non-ground points which are located in the boundaries of objects. After the boundary object points are extracted, a polygonal mask is generated from these non-ground points. The points of this polygonal mask are determined using the TIN. Finally, all the points located inside the polygonal mask are selected as non-ground points and all the other ones are labeled as ground points.

Preprocessing

The proposed method uses object boundaries and the local height differences of the adjacent points that are located around the borders of the objects. Hence, the noises affect the results, especially if these points are close to the borders of the objects. It should be noted that isolated and non-contiguous noises do not affect the results, because these points are grouped into segments. Very small segments are not taken into account (this will be discussed later). Therefore, CloudCompare software is used to remove noises. This software uses the statistical outlier removal method to remove noises, which uses the average of distances between adjacent points.

Window Dimension Determination

The neighborhood points are selected using a square window (Figure 2). The dimensions w of the window depend on the point-cloud density. One of the advantages of a photogrammetric point cloud is that the horizontal point spacing is approximately equal to the ground sample distance of the images. The ground sample distance of the photogrammetric point cloud is used to find the maximum distance between the neighborhood points, which is denoted by d_{max}. Since the window moves above the point cloud, the maximum point-to-point distance d_{max} is used for obtaining the window size. According to Figure 2, in order to consider all the points, the dimensions w of the window are selected as double the maximum distance ($2d_{max}$).

Extraction of the Boundary Object Points

Now, for each point in the point cloud, its adjacent points are extracted in 2D space. If the height difference between the highest point and the lowest point is greater than a certain height threshold T_h, then these points are labeled as boundaries for the non-ground points (Figure 3). The height threshold is set based on the heights of existing objects. For example, the minimum height of the buildings is about 3 m. The minimum height of cars is about 1.5 m. For trees, the heights are much greater. Figure 3 presents some examples of the extracted boundary objects of the buildings (c) and tree objects (b).

Mask Generation

The previously extracted points are the boundaries of the non-ground objects. Since the extracted boundary points are similarly labeled as non-ground points, they should be uniquely labeled based on their homogeneity. Therefore, the boundary points are segmented using the region-growing method such that the boundary points of an individual object are grouped in a unique segment. For this step, a certain distance r equal to two times (or more) the distance of d_{max} is used. However, some boundary points might be missed during this process. This problem appears when low-rise objects such as cars and trees are located

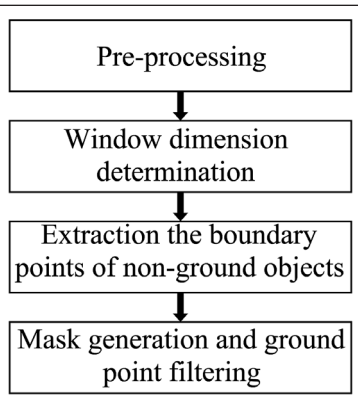

Figure 1. Workflow of the proposed method.

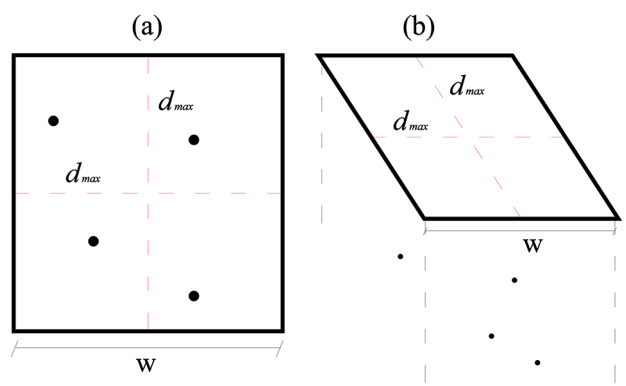

Figure 2. Window size: (a) 2D space and (b) 3D space.

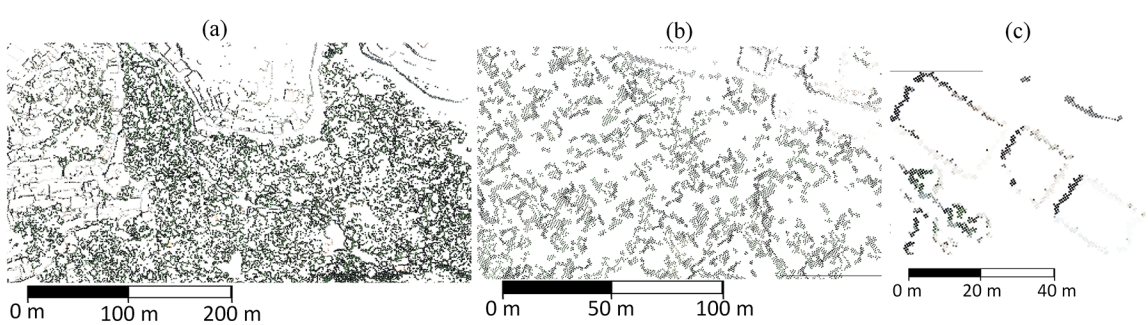

Figure 3. Examples of the extracted boundary points of non-ground objects: (a) all non-ground boundary objects, (b) tree boundaries, and (c) building boundaries.

around the borders of buildings. Therefore, the height difference between the building roof and the neighborhood object may be less than the height threshold. Due to this problem, the boundary points are not completely extracted. The proposed method therefore uses a distance equal to at least two times the maximum distance d_{max}.

After the boundary-segmentation process, a TIN is generated for each segment (Figure 4b). Now, we can create a polygon (mask) for each segment by using its TIN (Figure 4d). Awrangjeb (2016) used the same method to trace building boundary points. He used a distance threshold d_{th} equal to two times the maximum distance to remove unwanted triangle sides, where a TIN generates a convex polygon for the given point set (Figure 4b). Therefore, d_{th} is used to generate a more realistic shape (a concave shape, as shown in Figure 4c).

The triangle sides belonging to one triangle are located on the boundary. Then the points of these sides are extracted and traced by using the correlations between the points in the TIN, as each side connects two consecutive points. In this way, the points of the polygon are extracted in the form of a series of consecutive points behind each other (red line in Figure 4d). From the previous sections, we find that segments of fewer than three points are not taken into account because the TIN will not be generated from them. These points may be noise (see "Preprocessing" earlier).

Ground-Point Labeling

Finally, point labeling is done according to the extracted polygonal masks. So after all polygons are extracted for all objects, the points that are located inside these polygons are labeled as non-ground points (Figure 4e). This process selects entire points within the polygons as non-ground points. The remaining points in the point cloud are considered as ground points.

Comparison Methods

The performance of the proposed method is compared here with that of some popular ground-point cloud filtering methods that are available

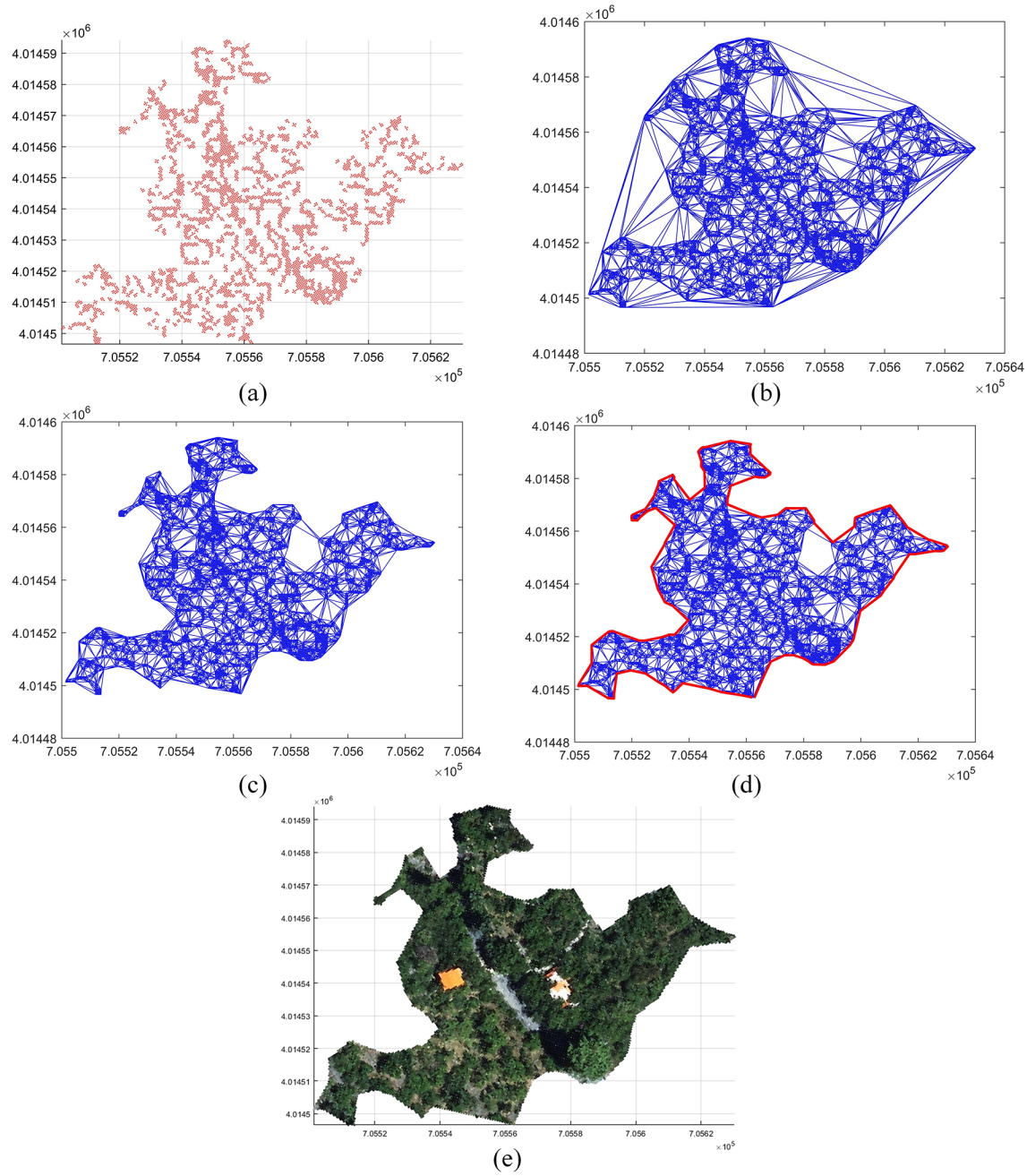

Figure 4. Mask generation: (a) a segment of points, (b) TIN, (c) mask generation, and (d) non-ground point detection. TIN = triangulated irregular network.

for comparison studies: cloth simulation filtering (CSF), multi-scale curvature classification (MCC), and gLiDAR.

The MCC method is applied by the MCC-LiDAR open-source command-line tool (Hudak and Shrestha 2013). This method generates a raster surface through thin plate spline interpolation. It uses curvature and a scale threshold in three scale domains *t*: 0.5, 1, and 1.5. If the method model converges in a scale domain, then the scale and curvature are changed and the process continues with the next scale domain until a convergence threshold value is achieved (Evans and Hudak 2007).

The gLiDAR method is applied by the non-commercial gLiDAR software (GeMMA Lab 2013). This method uses thin plate spline interpolation to determine non-ground points and ground points. The gLiDAR method has two major steps. In the first step, a maximum size parameter is used to remove points that belong to the largest object. In the second step, the filtered ground points are refined using three parameters k, n, and b, where k is the height difference between the digital terrain model and the point that is considered the ground, n is the height threshold used to decide if a point belongs to an object, and b is the ratio between the size of above-ground objects and their responses in the top-hat scale space (Serifoglu Yilmaz *et al.* 2018).

The CSF method is applied by the open-source CloudCompare software (CloudCompare 2022). This method turns the point cloud upside down (W. Zhang *et al.* 2016). Then it assumes that a piece of sticky cloth is dropped over the terrain after the terrain is turned upside down.

Experimental Results and Discussion

Two photogrammetric point-cloud data sets are used in the experiments, which cover many point-cloud filtering challenges (trees, forests, buildings, steep mountains, and similar challenges).

Data Sets

The two data sets are named Dehbar and Canopy Forest. Dehbar is a village with the same name in Khorasan province, Iran. Canopy Forest refers to a forest area in Gilan province, Iran. The Dehbar data set covers mountainous areas along with forest, non-forest, and residential areas. UltraCam-D was used to capture aerial images with a standard photogrammetric stereo mode (60% forward overlap and 30% lateral overlap) in both data sets. The ground sample distance of the captured aerial images is 0.1 m. These covered images are prepared through digital photogrammetric processing, and finally a colored point cloud is generated for each data set. The semi-global matching algorithm (Hirschmüller 2008), implemented in Inpho software (Match-T module), is used as the stereo-matching algorithm. Currently, this method is one of the well-known stereo-matching methods for point-cloud generation from aerial images in forest areas (Melin *et al.* 2017; Goodbody *et al.* 2019).

The interest area of the Dehbar data set covers approximately 1000×1000×205.6 m^3. The dimensions of the Canopy Forest data set are about 600×400×36.26 m^3. The interest area of both data sets is shown in Figure 5. Moreover, the Dehbar data set contains low-rise buildings with various shapes and dimensions. The density of the point cloud in the data sets is approximately 4 and 9 points/m^2, respectively. Hence, the point spacing is about 0.5 and 0.3 m, respectively.

In order to evaluate the results, the ground-truth points were manually extracted by an expert operator. This operation is done by selecting non-ground points of constructed and natural objects. Since the aerial images are taken in stereo mode, the polygons of constructed objects such as buildings are directly extracted by stereo-plotting. In this case, the stereo images serve as input for Inpho software, and then the expert agent directly extracts the polygons of constructed objects. After all

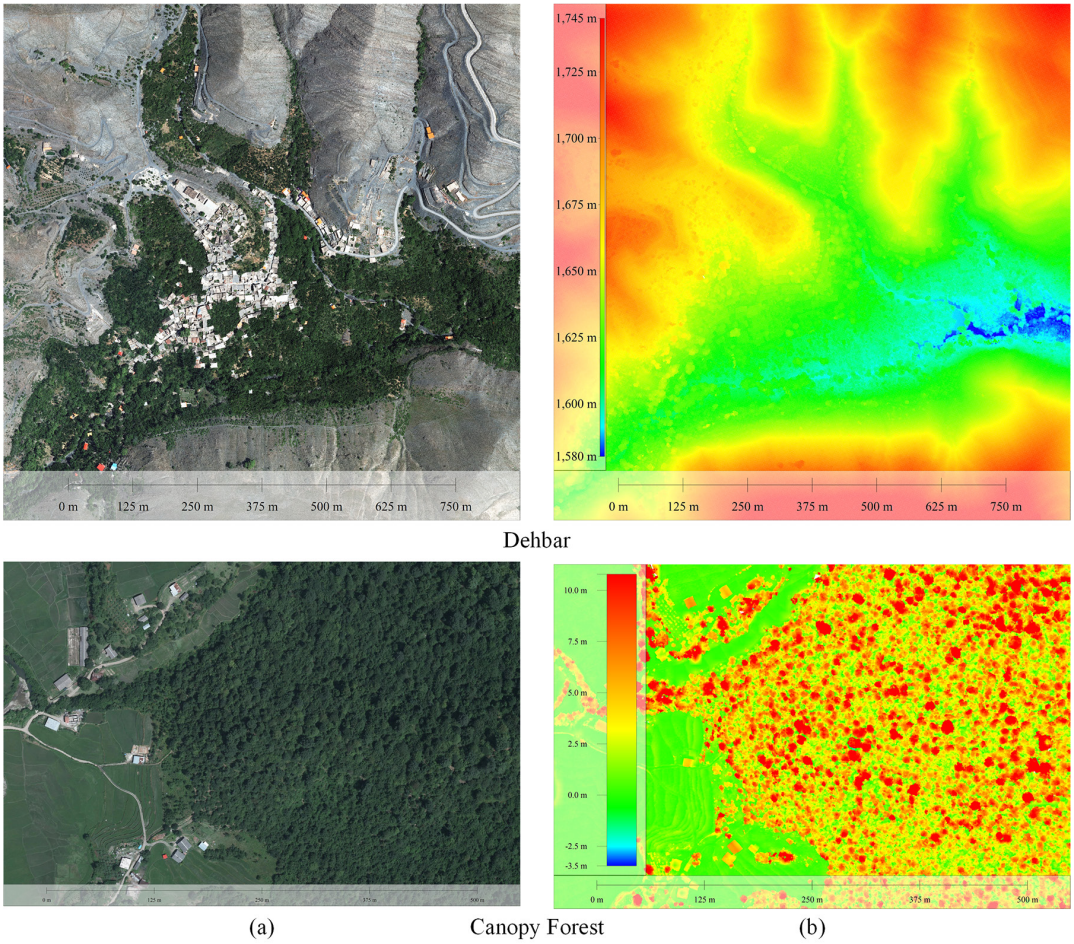

Figure 5. The experimental data sets: (a) the colored point cloud and (b) elevation.

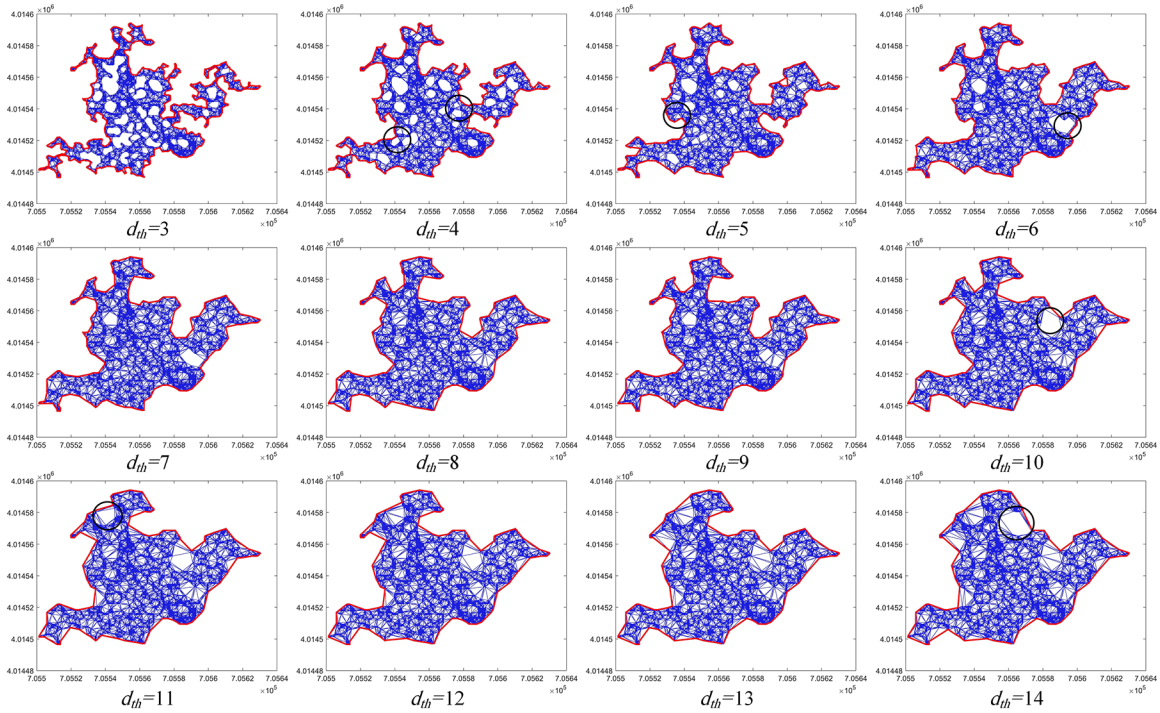

Figure 6. Effect of the distance d_{th} on the final extracted polygon.

polygons are extracted, the entire points within these polygons are selected as non-ground points. Since some non-ground points may have remained around the borders of polygons, the expert agent again manually selects those points as non-ground if their height meets two conditions: similarity with the height of the roof points of the constructed objects, and a height difference of more than 3 m from other points. This operation is done in Global Mapper software. For selecting reference non-ground points located on tree canopies, a vegetation mask is manually generated by thresholding on the normalized difference vegetation index (Rouse *et al.* 1973). This index is computed from the generated orthophoto by Inpho software. After the vegetation mask is generated, the entire points within the vegetation mask are labeled as suspected non-ground points. These points are located on tree canopies and low-level vegetation. Hence, points on tree canopies are labeled as non-ground and others are ruled out as ground points. Similar to the previous method for filtering the remaining points around the borders of constructed objects, the non-ground points on tree canopies are manually selected. Selecting the non-ground points on tree canopies is also done in Global Mapper. So all points are labeled as ground truth for ground and non-ground points.

Evaluation of the Proposed Method

Parameter Analysis

We previously mentioned that the window dimension w must be at least two times the maximum point-to-point distance d_{max}. To avoid missing any points from the window, we used $2.5d_{max}$. For the distance r, we used 2w, because object boundaries might not be fully extracted. In other words, there may be gaps within the boundaries. Thus, at the mask-extraction step, objects are fragmented into smaller ones. From the foregoing, we conclude that the density of the point cloud significantly affects the performance of the proposed method. Since the point cloud may have low density, large values are chosen for the parameters (w and r). As a result, objects that are far from each other will be combined into one segment and the ground points within them will be classified as non-ground points. Therefore, the proposed method is not recommended for low-density point clouds (less than 1 point/m^2). Hence, the d_{th} parameter should be quantitatively analyzed, because its effect on the results is significant.

For the qualitative analysis, the d_{th} parameter is analyzed for one segment to show its effect on the final generated polygon. As shown in Figure 6, selecting a greater d_{th} makes the generated polygons larger. Adding more areas gradually turns the polygon into a convex shape, where the black circles in the figure indicate that new areas have been added to the polygon. In other words, with a greater d_{th}, more points are classified as non-ground points, and vice versa. Also, selecting a very small distance (smaller than the region-growing distance r) splits the segment into smaller parts. Therefore, the distance d_{th} must be chosen greater than or equal to r. Moreover, the best d_{th} depends on the contents of the studied area. For rural areas with large forests, larger distances should be used, because there are many plants with low height whose boundaries have not been extracted. Often these plants are located around the extracted forest areas. Thus, choosing a greater distance will ensure that these plants are removed.

For quantitative evaluation, type I, type II, and total error metrics are used. The effect of the distance d_{th} is quantitatively evaluated in the Dehbar data set. As shown in Figure 7, the results illustrate that type I error is not affected much and has fluctuating values. This means that this error is not linearly related to this parameter. However, the results for type II error improve when the distance d_{th} is increased. This is due to the removal of the low-height vegetation that was mentioned earlier. The improvement in type II error is accompanied by improvement of the total error.

Also, as presented in Figures 6 and 7, choosing the best d_{th} is related to the contents of the studied area. Therefore, selecting a d_{th}

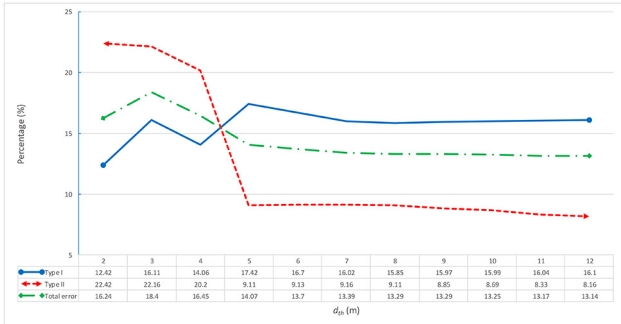

Figure 7. The effect of the distance d_{th} on type I, type II, and total errors.

value greater than 5 m is good for forest areas. Moreover, removing low-height vegetation improves the result for type II error. In addition, selecting a d_{th} value greater than 5 m does not convert polygons into convex shapes, and thus it maintains polygon shape.

Overall Results

The qualitative and quantitative results of the proposed method are shown in Figure 8 and Table 1, respectively. Figure 8 also presents some of the pros and cons of the proposed method on the Dehbar data set.

For the qualitative evaluation, we visually study the results to find the advantages and disadvantages of the proposed method. However, for the quantitative evaluation, type I, type II, and total error metrics (Sithole and Vosselman 2003) are computed for the results. Type I

Table 1. Ground-point filtering results.

Data Set	T_h (m)	d_{max} (m)	w (m)	r (m)	dth (m)	Type I error (%)	Type II error (%)	Total error (%)
Dehbar	1.5	0.53	$2d_{max}$	$2w$	10	13.74	8.75	11.9
Canopy Forest	1.5	0.31	$2d_{max}$	$2w$	5	11.93	3.35	6.02
Mean						12.84	6.05	8.96
Min						11.93	3.35	6.02
Max						13.74	8.75	11.9

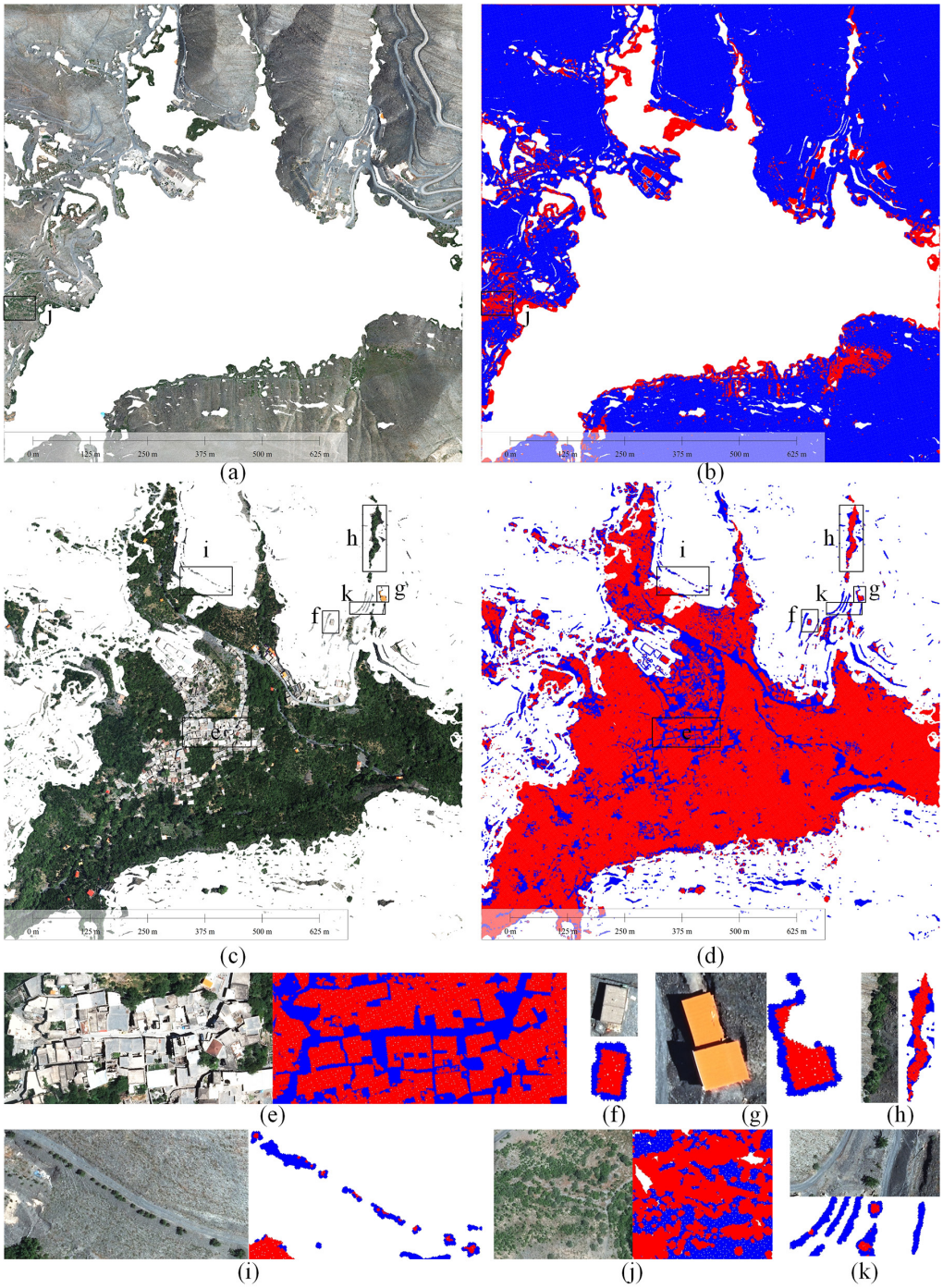

Figure 8. The results of the proposed method for the Dehbar data set. (a) and (b) The filtered ground points. (c) and (d) The non-ground points. Blue points are ground points and red points are non-ground points. (e to k) Some examples of the advantages and disadvantages of the proposed method. White areas represent no data.

error is the error percentage in classifying ground points (Equation 1). On the other hand, type II error refers to the error percentage in classifying non-ground points (Equation 2). The total error shows the total ratio of both type I and type II errors (Equation 3):

$$\text{Type I} = \frac{b}{a+b} \tag{1}$$

$$\text{Type II} = \frac{c}{c+d} \tag{2}$$

$$\text{Total} = \frac{b+c}{a+b+c+d} \tag{3}$$

where a is the number of the ground points that have been correctly classified as ground points, b is the number of the ground points that have been incorrectly classified as non-ground points, c is the number of non-ground points that have been incorrectly classified as ground points, and d is the number of non-ground points that have been correctly classified as non-ground points.

For the qualitative evaluation, we select the Dehbar data set to show the pros and cons of the proposed method because it contains all point-cloud filtering challenges. According to Figure 8a–d, large forest areas which are located on the hillsides have been removed. Also, the forests located in the valley area have been eliminated. Moreover, isolated and small trees have been successfully removed (Figure 8i), and trees located in the mountain cliff are excluded (Figure 8h). This is one of the strong advantages of the proposed method. These results demonstrate that the proposed method is not affected by the terrain type. The high elevation differences of the terrain do not affect the performance of the proposed method, because this method locally extracts boundaries as well as non-ground points. On the other hand, small and large buildings have also been eliminated, despite their small height (Figure 8e–f). Moreover, the other existing 3D objects around the tall building do not reduce the performance of the proposed method. As presented in Figure 8g, some buildings have been partially removed. This is because the building height is low from one side to the neighborhood objects or steep ground. Thus, the building roof is close to the ground from one side and its points are classified as ground points. Therefore, the buildings are not removed completely. Generally, the results presented in Figure 8 demonstrate that the shape type of the studied objects does not have a significant effect on the proposed method.

The disadvantages of the proposed method are also presented in Figure 8. As shown in Figure 8e, some ground points of road objects have been classified as non-ground points. This happens when a large distance r is chosen. It also might be because of the proximity of the different objects to each other (buildings and trees, among others). The low density of the point cloud also leads to selection of a large window size. These factors merge the boundaries of objects. Thus, the ground points located between them are identified as non-ground points. From Figure 8k, we find that the proposed method has another disadvantage. Roadsides in mountainous areas have high local height differences. Thus, their points will be identified as non-ground points. According to Figure 8j, for low-height vegetation, points will not be removed if their height is less than the height threshold.

For quantitative evaluation of the experimental data sets, the evaluation metrics (Equations 1–3) have been calculated (Table 1). The large type I error indicates that the ground points located between the buildings (road points) or trees (bare earth) have been classified as non-ground points. Since these points are located within the extracted object boundaries, they are selected as non-ground points (Figure 8e). Type I error will be low if the 3D objects are distinguishable. However, type II error is low for both data sets. In the Dehbar data set, it is about 8.75%, which is related to the low-height vegetation whose boundaries were not extracted (Figure 8j). Nevertheless, the corresponding result in the second data set is excellent because all the vegetation boundaries are extracted. In general, the results from the Dehbar data set are suitable when compared against the existing challenges.

Comparison, Discussion, and Limits

In this section, the performance of the proposed method is compared with that of other methods: CSF, MCC, and gLiDAR. It should be noted that the parameters of these methods have been fine-tuned to achieve the best results. These parameters are listed in Table 2.

Table 2. Tuned parameters of the compared methods.

		Data Set	
Method	**Parameter**	**Dehbar**	**Canopy Forest**
CSF	Cloth resolution (m)	0.5	1
	Max iteration	500	500
	Classification threshold	0.9	0.9
	Rigidness	Steep slope	Flat
MCC	Scale t	1	1.25
	Max curvature	0.3	0.1
gLiDAR	Max size value (m)	50	50
	k	0.03	0
	n	0.01	0.2
	b	0.1	0.25

CSF = cloth simulation filtering; MCC = multi-scale curvature classification.

The evaluation metrics are computed for all data sets in order to compare the selected methods with the proposed method. All the methods and their results are presented in Tables 3, 4, and 5. The point-cloud filtering results for the selected methods are also shown in Figures 9 and 10.

Table 3. Type I error results (%) for the different methods.[a]

	Data Set				
Method	**Dehbar**	**Canopy Forest**	**Mean**	**Min**	**Max**
CSF	4.46	10.65	7.56	4.46	**10.65**
MCC	9.66	19.67	14.67	9.66	19.67
gLiDAR	**3.94**	11.14	**7.54**	**3.94**	11.14
Proposed method	13.74	11.93	12.84	11.93	13.74

CSF = cloth simulation filtering; MCC = multi-scale curvature classification.
[a]Boldface indicates the best result in that column.

Table 4. Type II error results (%) of the different methods.[a]

	Data Set				
Method	**Dehbar**	**Canopy Forest**	**Mean**	**Min**	**Max**
CSF	37.31	8.12	22.72	8.12	37.31
MCC	35.05	11.97	23.51	11.97	35.05
gLiDAR	27.16	3.71	15.44	3.71	27.16
Proposed method	**8.75**	**3.35**	**6.05**	**3.35**	**8.75**

CSF = cloth simulation filtering; MCC = multi-scale curvature classification.
[a]Boldface indicates the best result in that column.

Table 5. Total error results (%) of the different methods.

	Data Set				
Method	**Dehbar**	**Canopy Forest**	**Mean**	**Min**	**Max**
CSF	16.55	8.99	12.77	8.99	16.55
MCC	19.01	14.61	16.81	14.61	19.01
gLiDAR	12.49	6.26	9.38	6.26	12.49
Proposed method	**11.9**	**6.02**	**8.96**	**6.02**	**11.9**

CSF = cloth simulation filtering; MCC = multi-scale curvature classification.
[a]Boldface indicates the best result in that column.

As presented in Table 5, the total error indicates that compared with the selected point-cloud filtering methods, the proposed method has better performance. In addition, this evaluation metric shows that the MCC method has the lowest accuracy for ground-point cloud filtering. Moreover, Table 4 demonstrates that the proposed method has better results for type II error, which indicates that most non-ground points have been correctly classified as non-ground points, whereas the other methods fail to achieve better results. This might be because of the

existing large forest areas or steep mountainous areas, challenges for which the selected methods were not developed. However, type I error indicates that the proposed method does not work well in the Dehbar data set. This is one of the disadvantages of the proposed method, which we have mentioned already. Since some ground points, such as road points and bare earth points, are densely surrounded by object points, they are classified as non-ground points. However, compared with other methods, the proposed method has better type I error in the second data set. Moreover, compared with the selected methods, Figure 9b illustrates that ground points on the mountains are well filtered by the proposed method. This result also demonstrates that the proposed method is not affected by the height differences in the mountainous areas. We can notice, as presented in Figure 9 and Table 4, that the results of the other methods are significantly affected by the area type, since these methods have different performances in different area types.

One of the challenging areas in photogrammetric point-cloud filtering is forest areas. In these areas, most ground points are hidden under tree canopies. In the proposed method, if bare land is surrounded by trees in leaf-on status, the ground points will be removed as non-ground points, because the trees in this case will be connected to each other. Therefore, anything inside the trees will be removed. In leaf-off status, the trees will not be connected to each other, and thus bare land within the forests will not be removed. Moreover, the point cloud is generated by the Semi-Global Matching algorithm (Hirschmüller 2008). Since this algorithm made the thin bare land have the same elevation as tree areas, the proposed method might fail in those areas. Hence focusing on stereo-matching algorithms to directly remove non-ground points could be considered in future studies.

As mentioned previously, we find that the proposed method yields promising results even in mountainous areas. The area type and the size of non-ground objects do not affect the performance of the proposed method. However, point-cloud filtering in dense 3D objects is a challenge that is not solved by the proposed method. Therefore, studies focusing on point-cloud filtering in complex landscapes could be conducted in the future.

Conclusion

In this article, a new boundary-based method is proposed for filtering ground points from a photogrammetric point cloud. The proposed

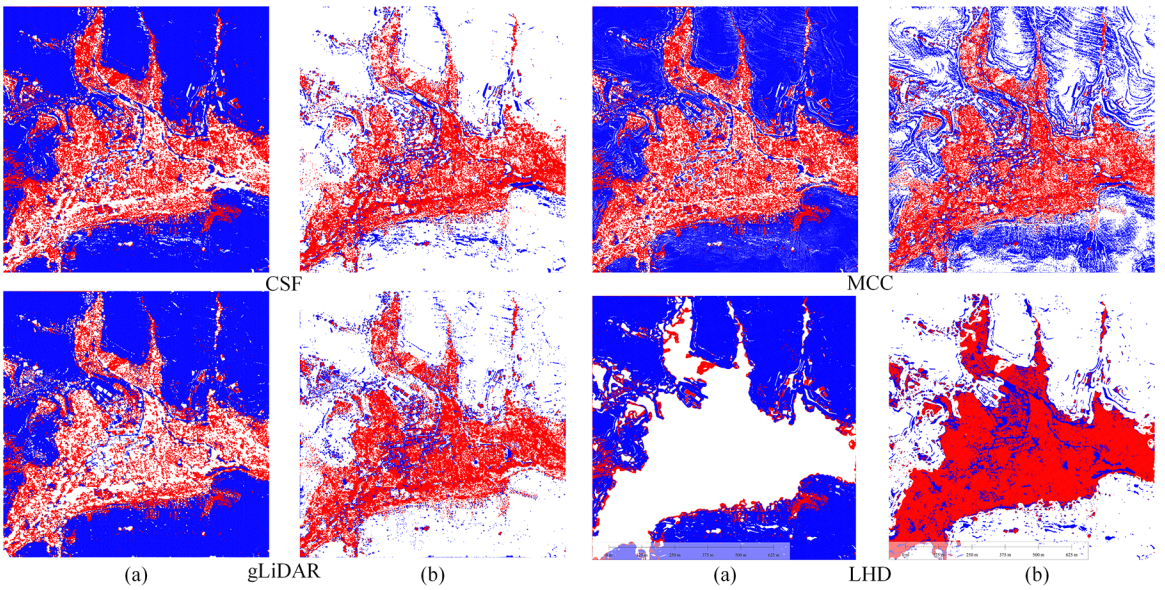

Figure 9. Visual comparison results by different point-cloud filtering methods on the Dehbar data set. (a) The results of the filtered ground points; (b) the results of the removed non-ground points. Blue points are ground points and red points are non-ground points. White areas represent no data.

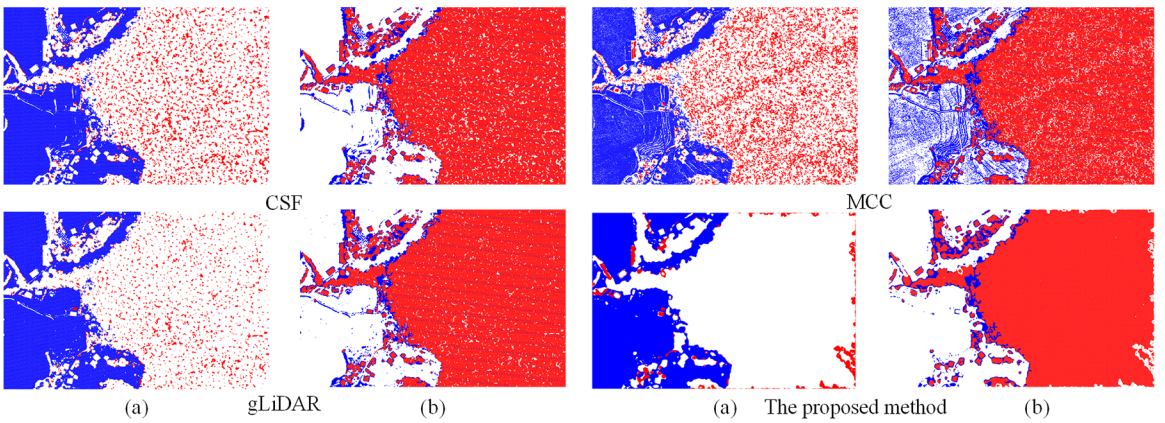

Figure 10. Visual comparison results by different point-cloud filtering methods on the Canopy Forest data set. (a) The results of the filtered ground points; (b) the results of the removed non-ground points. Blue points are ground points and red points are non-ground points. White areas represent no data.

method addresses the following challenges: mountainous areas, large forest areas, and the lack of the last pulse. The proposed method is examined in two different data sets with various area types, landscapes, and 3D object sizes. The results show that there are no problems with the sizes of objects (small or large buildings, large or small forest areas). Also, there is no problem if the studied area is mountainous. The results of the experiments demonstrate the superiority of the proposed method compared with CSF, MCC, and gLiDAR methods with respect to the total error metrics. However, problems for the proposed method are low-height objects and ground points surrounded by objects. In other cases, the quantitative results show that the proposed method is effective for other existing challenges. In the future, spatial and spectral features will be extracted to avoid the two problems mentioned.

References

Arefi, H. and M. Hahn. 2005. A morphological reconstruction algorithm for separating off-terrain points from terrain points in laser scanning data. International Archives of the Photogrammetry, Remote Sensing and Spatial Information Sciences 36 (3/W19), 120-125.

Awrangjeb, M. 2016. Using point cloud data to identify, trace, and regularize the outlines of buildings. *International Journal of Remote Sensing* 37:551–579.

Axelsson, P. 2000. DEM generation from laser scanner data using adaptive TIN models. *International Archives of Photogrammetry and Remote Sensing* 33:110–117.

Chehata, N., L. Guo and C. Mallet. 2009. Airborne lidar feature selection for urban classification using random forests. In Laserscanning Paris, France. hal-02384719

Chen, Q., P. Gong, D. Baldocchi and G. Xie. 2007. Filtering airborne laser scanning data with morphological methods. *Photogrammetric Engineering and Remote Sensing* 73:175–185.

Cheng, P., Z. Hui, Y. Xia, Y. Y. Ziggah, Y. Hu and J. Wu. 2019. An improved skewness balancing filtering algorithm based on thin plate spline interpolation. *Applied Sciences* 9:203.

CloudCompare. 2022. <http://www.danielgm.net/cc/release/> Accessed 17 July 2022

Elmqvist, M. 2002. Ground surface estimation from airborne laser scanner data using active shape models. *International Archives of the Photogrammetry, Remote Sensing and Spatial Information Sciences* 34:114–118.

Evans, J. S. and A. T. Hudak. 2007. A multiscale curvature algorithm for classifying discrete return LiDAR in forested environments. *IEEE Transactions on Geoscience and Remote Sensing* 45:1029–1038.

GeMMA Lab. 2013. gLiDAR. <https://gemma.feri.um.si/gLiDAR/download.html> Accessed 17 July 2022.

Gevaert, C. M., C. Persello, F. Nex and G. Vosselman. 2018. A deep learning approach to DTM extraction from imagery using rule-based training labels. *ISPRS Journal of Photogrammetry and Remote Sensing* 142:106–123.

Goodbody, T.R.H., N. C. Coops and J. C. White. 2019. Digital aerial photogrammetry for updating area-based forest inventories: A review of opportunities, challenges, and future directions. *Current Forestry Reports* 5:55–75.

Hirschmüller, H. 2008. Stereo processing by semiglobal matching and mutual information. *IEEE Transactions on Pattern Analysis and Machine Intelligence* 30:328–341.

Hu, X. and Y. Yuan. 2016. Deep-learning-based classification for DTM extraction from ALS point cloud. *Remote Sensing* 8:730.

Hudak, A., & Shrestha, R. 2013. MCC-LIDAR. <https://sourceforge.net/p/mcclidar/wiki/Home/> Accessed 17 July 2022.

Hui, Z., Y. Hu, Y. Z. Yevenyo and X. Yu. 2016. An improved morphological algorithm for filtering airborne LiDAR point cloud based on multi-level kriging interpolation. *Remote Sensing* 8:35.

Jin, S., Y. Su, X. Zhao, T. Hu and Q. Guo. 2020. A point-based fully convolutional neural network for airborne LiDAR ground point filtering in forested environments. *IEEE Journal of Selected Topics in Applied Earth Observations and Remote Sensing* 13:3958–3974.

Li, Y., H. Wu, H. Xu, R. An, J. Xu and Q. He. 2013. A gradient-constrained morphological filtering algorithm for airborne LiDAR. *Optics & Laser Technology* 54:288–296.

Melin, M., L. Korhonen, M. Kukkonen and P. Packalen. 2017. Assessing the performance of aerial image point cloud and spectral metrics in predicting boreal forest canopy cover. *ISPRS Journal of Photogrammetry and Remote Sensing* 129:77–85.

Meng, X., L. Wang, J. L. Silván-Cárdenas and N. Currit. 2009. A multi-directional ground filtering algorithm for airborne LIDAR. *ISPRS Journal of Photogrammetry and Remote Sensing* 64:117–124.

Niemeyer, J., F. Rottensteiner and U. Soergel. 2012. Conditional random fields for lidar point cloud classification in complex urban areas. *ISPRS Annals of the Photogrammetry, Remote Sensing and Spatial Information Sciences* 1:263–268.

Pingel, T. J., K. C. Clarke and W. A. McBride. 2013. An improved simple morphological filter for the terrain classification of airborne LIDAR data. *ISPRS Journal of Photogrammetry and Remote Sensing* 77:21–30.

Qin, L., W. Wu, Y. Tian and W. Xu. 2017. LiDAR filtering of urban areas with region growing based on moving-window weighted iterative least-squares fitting. *IEEE Geoscience and Remote Sensing Letters* 14:841–845.

Rizaldy, A., C. Persello, C. M. Gevaert and S. J. Oude Elberink. 2018. Fully convolutional networks for ground classification from lidar point clouds. *ISPRS Annals of the Photogrammetry, Remote Sensing and Spatial Information Sciences* 4:231–238.

Rouse Jr, J. W., R. H. Haas, J. A. Schell and D. W. Deering. 1973. Monitoring the vernal advancement and retrogradation (green wave effect) of natural vegetation. No. NASA-CR-132982.

Serifoglu Yilmaz, C., V. Yilmaz and O. Güngör. 2018. Investigating the performances of commercial and non-commercial software for ground filtering of UAV-based point clouds. *International Journal of Remote Sensing* 39:5016–5042.

Shan, J. and C. K. Toth, eds. 2018. *Topographic Laser Ranging and Scanning: Principles and Processing*, 2d ed. Boca Raton, Fla.: CRC Press.

Shi, X., H. Ma, Y. Chen, L. Zhang and W. Zhou. 2018. A parameter-free progressive TIN densification filtering algorithm for lidar point clouds. *International Journal of Remote Sensing* 39:6969–6982.

Sithole, G. 2001. Filtering of laser altimetry data using a slope adaptive filter. *International Archives of Photogrammetry and Remote Sensing* 34:203–210.

Sithole, G. and G. Vosselman. 2003. *Report: ISPRS Comparison of Filters*. Delft, Netherlands: ISPRS, Commission III, Working Group 3.

Vosselman, G. 2000. Slope based filtering of laser altimetry data. *International Archives of Photogrammetry and Remote Sensing* 33:935–942.

Zeybek, M. and İ. Şanlıoğlu. 2019. Point cloud filtering on UAV based point cloud. *Measurement* 133:99–111.

Zhang, J., X. Lin and X. Ning. 2013. SVM-based classification of segmented airborne LiDAR point clouds in urban areas. *Remote Sensing* 5:3749–3775.

Zhang, W., J. Qi, P. Wan, H. Wang, D. Xie, X. Wang and G. Yan. 2016. An easy-to-use airborne LiDAR data filtering method based on cloth simulation. *Remote Sensing* 8:501.

Call for *PE&RS* Special Issue Submissions

Innovative Methods for Geospatial Data using Remote Sensing and GIS

Internationally comparable data is a global need for managing resources, monitoring current trends and taking actions for sustainable living. Even though there has been a significant progress on geospatial data availability, extensive data gaps are still a major problem for general assessment and supervise the progress through the years. According to United Nations 2022 The Sustainable Development Goals Report, while health and energy sectors have the highest data available, limited data available for climate action.

The COVID-19 crisis has also shown that there are innovative data collection methods utilizing information and computer technologies. However, only 5% of the countries have benefit from remote sensing technologies to measure the impact of COVID-19. Additionally, novel approaches such as artificial intelligence should be used in conjunction with assessments to make sure they are put to use for critical situations.

The recent developments in remote sensing, geographic information systems and ICT have provided a wide accessibility to create geospatial data for various purposes. The proposed special issue focuses on *"Innovative Methods for Geospatial Data using Remote Sensing and GIS" for wide range of applications. This special issue aims to bring researchers to share knowledge and their expertise about innovative methods to contribute to fill data gaps around the world for a better future.*

The proposed special issue aims to contributes ASPRS's key mission on 'Simplify and promote the use of image-based geospatial technologies for the end-user', 'Promote collaboration between end users and geospatial experts to match data and technology to applications and solutions' and 'promote the transfer of geospatial data and information technology to developing nations' by providing innovative methods to create geospatial data using remote sensing and geographic information systems utilizing state-of-the-art developments and solutions.

Deadline for Manuscript Submission—July 1, 2023

Submit your Manuscript to http://asprs-pers.edmgr.com

Guest Editors

Dr. Tolga Bakirman, bakirman@yildiz.edu.tr , *Yildiz Technical University, Department of Geomatic Engineering*, Davutpasa Campus, 34220 Esenler-Istanbul/Turkey

Dr. George Arampatzis, garampatzis@pem.tuc.gr, *Technical University Crete, School of Production Engineering & Management*, 73100 Chania – Crete/Greece

Deep Learning–Based Monitoring Sustainable Decision Support System for Energy Building to Smart Cities with Remote Sensing Techniques

Wang Yue, Changgang Yu, A. Antonidoss, and Anbarasan M

Abstract

In modern society, energy conservation is an important consideration for sustainability. The availability of energy-efficient infrastructures and utilities depend on the sustainability of smart cities. The big streaming data generated and collected by smart building devices and systems contain useful information that needs to be used to make timely action and better decisions. The ultimate objective of these procedures is to enhance the city's sustainability and livability. The replacement of decades-old infrastructures, such as underground wiring, steam pipes, transportation tunnels, and high-speed Internet installation, is already a major problem for major urban regions. There are still certain regions in big cities where broadband wireless service is not available. The decision support system is recently acquiring increasing attention in the smart city context. In this article, a deep learning–based sustainable decision support system (DLSDSS) has been proposed for energy building in smart cities. This study proposes the integration of the Internet of Things into smart buildings for energy management, utilizing deep learning methods for sensor information decision making. Building a socially advanced environment aims to enhance city services and urban administration for residents in smart cities using remote sensing techniques. The proposed deep learning methods classify buildings based on energy efficiency. Data gathered from the sensor network to plan smart cities' development include a deep learning algorithm's structural assembly of data. The deep learning algorithm provides decision makers with a model for the big data stream. The numerical results show that the proposed method reduces energy consumption and enhances sensor data accuracy by 97.67% with better decision making in planning smart infrastructures and services. The experimental outcome of the DLSDSS enhances accuracy (97.67%), time complexity (98.7%), data distribution rate (97.1%), energy consumption rate (98.2%), load shedding ratio (95.8%), and energy efficiency (95.4%).

Introduction

The population in urban areas is currently increasing. Shifting from villages to cities raises the population by 2.5 billion in large cities (Mlecnik *et al.* 2020). One of the biggest challenges is the increasing demand for energy and the resulting strain on local services (Khan *et al.* 2017). For this reason, to achieve the goal of reducing environmental impacts and developing sustainable development, cities should adhere to such a new paradigm via the smart cities (Pournaras 2020) definition, improving people's standard of living. A smart city is a location that uses virtual and communications technology to make conventional networks and facilities more effective for its people and industry (Villamayor-Tomas *et al.* 2022). Digitization of the energy sector based on tracking via the Internet of Things (IoT) is needed (Kumar *et al.* 2020). Energy is one of society's key pillars, and administration is important to guarantee energy provision (Ahmed *et al.* 2020).

Sustainable energy is of increasing global interest because of heightened energy use, climate change, and the need for increased energy production (Hossein Motlagh *et al.* 2020; Mao *et al.* 2020). Because buildings are responsible for over one-third of the main global energy expenditure, the construction of smart cities is needed. Depending on the market growth and increased focus on inhabitants' lives, energy usage would remain high in the future (Guo *et al.* 2022). Energy services in building structures, such as heat, ventilation systems, and light services, are important energy users (Zhuang *et al.* 2020). They often experience system malfunctions, insufficient monitoring, and inadequate maintenance, leading to a significant waste of resources. Governments, institutions, and the rest of society all have a role in making sound decisions. More and more people are choosing to live ethical, environmentally friendly lives, and as a consequence, they are looking for corporations that match their beliefs.

Improvement of building energy technology's operating efficiency can dramatically minimize energy usage (Green *et al.* 2020). If energy systems increase operational efficiency, the correct provision of simple energy demands in buildings is necessary (Shu *et al.* 2020). Building design's energy needs can be revealed by expected cooling, warming loads, and power loads. They are helpful when energy generation services are optimally regulated (Li *et al.* 2020). Effective energy usage and utilization strategies guarantee a targeted use for industry and stable energy development in energy plants (Reddy *et al.* 2020). Smart building is important for both sides' energy balance to achieve sustainability in energy interaction between the supplier and the user (Roth *et al.* 2020). Techniques of energy prediction are incredibly beneficial; they can estimate the energy use of consumers in a building. Missing energy forecasts contributes to extra costs and the waste of energy (Riaño-Vargas *et al.* 2018). Methodologies of energy prediction are abundant in industries and household applications. The energy forecasting system of energy sources can broadly be classified into two groups: physical and data-driven approaches (Elavarasan *et al.* 2020).

Scientific methods use physical concepts to assess the energy flow model in the structural energy source. Even then, analytical methods for complex building energy sources are typically very complex and time consuming (Elavarasan *et al.* 2020). The construction of automated systems is very common, and large quantities of building data were stored (Liu *et al.* 2020). It gives the chance to incorporate data-driven approaches to predict building energy charges. Data-driven approaches are usually more versatile than physical processes (Liu *et al.* 2021). In several everyday applications, single charge prediction systems ensure

Wang Yue is with the School of Computer and Software, Nanyang Institute of Technology, Nanyang, Henan 473000, People's Republic of China (sophia07040815@163.com).

Changgang Yu is with Nanyang Puguang Electric Power Co., Ltd, Nanyang, Henan 473000, People's Republic of China.

A. Antonidoss is with the Hindustan Institute of Technology, India.

Anbarasan M is with the Sairam Institution of Technology, India.

Contributed by Priyan M K, January 18, 2022 (sent for review February 14, 2022; reviewed by Mohamed P S, Burhanuddin MA, Suseendran G).

Photogrammetric Engineering & Remote Sensing
Vol. 88, No. 9, September 2022, pp. 593–601.
0099-1112/22/593–601

doi: 10.14358/PERS.22-00010R2

sufficient energy requirements. The computer-smart methods used in predicting demand play a significant role in decreasing the energy shortage. To assess the limits and to produce better judgment, especially concerning resources, the value of data increases. Energy management plans are incorporated into the conventional techniques for cities and regions. Smart city current energy usage must be compared, ranked, and estimated to assess the existing situation. Smart cities need to assess retrofitting options for their building portfolio, including energy use, size, vintage, kind, ownership, and socioeconomic potential, to make informed decisions. Cities require quantitative decision analysis tools that combine measurable facts, physics, and data-driven models to make informed decisions. Such systems need active computer modeling and optimization that incorporates the many building systems, weather data, human behavior, and operation patterns through remote sensing technologies to design and run them effectively.

Modern technologies use sophisticated information technology in an intelligent framework to control various components. Intelligent buildings minimize energy usage and promote building efficiency and smart communications systems. Different system integration variables, such as measurements, lighting, and system integration methods, assess functional energy savings in the structure. In this article, a deep learning–based sustainable decision support system (DLSDSS) has been proposed for energy development in smart cities. SDSS proposes the incorporation of the IoT into smart energy management buildings, using profound training techniques to make decisions about sensor knowledge. The emerging deep learning approaches can be used for classifying energy efficiency–based buildings.

The main contributions of this article are the following:

- A long-term sustainable future is dependent on their existence. Sophisticated methods and solutions in smart cities help economic development and improve people's lives.
- In a smart city, DLSDSS is concerned primarily with employing smart technology and data analysis to optimize municipal activities and boost economic development while increasing the quality of life for people.
- The energy sector is expected to impact the IoT significantly. It is a cost-saving tool for monitoring a room's temperature with sensors to manage the energy use of a whole building with complicated applications.

The remaining work is given as follows. The next section provides insights into background studies. Then a DLSDSS for energy construction in smart cities is discussed, the results are validated, and the research is concluded.

Background Study on the SDSS for Energy Building to Smart Cities

Thermal comfort (heating or cooling) and air quality are the primary factors determining how much energy is utilized in a building (ventilation). Electric lighting, residential hot water, and other electrical devices are common energy uses. The correctness of this theory was confirmed by the study's findings, which were based on a thorough review of the literature. Research publications are the sole way to verify Google Scholars' accuracy. This section discusses several works that various researchers had carried out.

Zhuang *et al.* (2020) developed NARX-ANN (nonlinear autoregressive artificial neural network [ANN]). An HVAC-DHW (heating, ventilation, and air conditioning) system was used for sustainable solar and wind energy hybrid heating and cooling that measures energy usage by adaptive NARX-ANN and fuzzy controllers dependent on user requirements. The atmosphere and structure are sensed primarily through the sensor, and heating and cooling impacts are then loaded into deep learning NARX-ANN, which predicts internal building temperatures.

Rahman *et al.* (2020) proposed an intrusion detection system (IDS). The limiting of clustered IDS is explored for resource-controlled devices with two approaches: moderate and dispersed. Efficient collection and features integration was extracted, and possible fog-focused coordinated analysis was detected. This predicted weather was fed into a fluid system to optimize the user request–based production. Such collected data can be transmitted utilizing a digital energy-sensing device based on its needs.

Zekić-Sušac *et al.* (2021) introduced a machine learning–based system for managing energy efficiency (MLBS-EE). MLBS-EE aims to address how data-analytic platforms and machine learning can be integrated into an efficient public service energy efficiency model. A forecasting model was generated for real energy usage of Croatian government facilities, deep learning methods, and random forest with parameter reduction techniques.

Singh *et al.* (2020) discussed deep learning–based IoT-oriented infrastructure (DLB-IoT). The DLB-IoT framework is used for a safe, smart city where a cyber-physical system shared ecosystem was created by the company Blockchain and where standards for system data transmission have been built for software-defined networking. A profound network was used to address transmission delay and central control, usability, and the proposed infrastructure's physical layers.

Sztubecka *et al.* (2020) introduced a DSS and Geographic Information System (DGIS). The framework contains energy users with details on the position of areas for resource quality improvement. The opportunity for implementing low-energy structures and using sustainable power sources was recognized as such. The DGIS framework is used for the study to adjust to towns and preserve the environment.

Hajiabadi *et al.* (2020) proposed deep learning for solar power prediction (DL-SPP). The advanced innovations of DL for photovoltaic energy production suggest a new methodology for regression estimation for the photovoltaic device's performance based on specific data variables. The suggested loss function was, in particular, a collection of three well-known loss features, correntropy, exact, and square loss, that collectively promote robustness and generalization. The suggested target function is then implemented in a deep learning approach to evaluate a photovoltaic module's performance.

Strielkowski *et al.* (2020) discussed smart cities' economic efficiency and energy security (EEE-SC). EEE-SC includes a financial study of construction changes leading to a reduction of smart cities' need for energy as the automated light-emitting diode (LED) streetlight systems. The performance of LED street lighting was measured in intelligent cities with widely used sodium-based streetlights. The findings show that the LED street illumination model can dramatically decrease any new city's energy requirements.

Hafeez *et al.* (2020) proposed a novel hybrid electrical energy consumption forecasting (HECF) model. The HECF-based deep learning model utilizes an activating feature of the corrected linear unit and the multiple regression system. The proposed HECF allows for potential electric energy use for effective energy production in a smart grid. A modern hybrid architecture consisting of four units is the HECF model: (1) the signal collection and sorting system, (2) the predictive learning device, (3) the automated system optimization device, and (4) the user device.

Anthony Jnr *et al.* (2020) suggested the deployment of application programming interfaces (APIs). APIs were examined to manage resource information for residential housing and electric cars digitally and historically. Information and judgment on sustainable energy are provided, and local energy consumption can build an infrastructure with APIs to use big data.

Zhang *et al.* (2021) planned cities worldwide that are focusing their infrastructure strategies on sustainable mobility policies, building stock updates, increasing renewable energy production, improving waste management, and implementing ICT infrastructures in response to the massive social and environmental change around the world. IoT-based smart green energy has been suggested for smart cities in this article. Pervasive monitoring and secure communication were possible in smart cities with IoT adoption. In smart cities, IoT sensors can be used to monitor energy use, forecast demand, and save money.

As observed from the literature study, DLSDSS has been implemented to incorporate the IoT into smart energy management structures, using deep learning approaches to make decisions about sensor knowledge. It is the latest deep learning approach for classifying energy efficiency-based structures. Compared to the existing methods

NARX-ANN, IDS, MLBS-EE, DLB-IoT, DGIS, DL-SPP, EEE-SC, HECF, and APIs, the proposed method improves in a smart city.

Deep Learning–Based Sustainable DSS

The main objective of energy building to smart cities leads to urban transformation, and productive communities are to set up a highly flexible and repeatable solution. The model is focused on an integrated approach and implementing energy-saving steps while improving the effectiveness of sustainable energy on cities' key consumption markets. Remote sensing technology specifies two key levels, and the energy storing and monitoring situation is independently mentioned for energy building in smart cities. The first stage represents smart cities and industrial demand and supplies for energy management. The tools are used for grid stations dispersed among different user groups, mostly in the city areas. The energy services group is directly responsible for forecasting and controlling the energy usage, while a data owner serves as a third-party listener among customers and intelligent grids. The data owner includes domestic needs and sectors housed, evaluated, and transmitted to the service provider to the terminal building for energy supplies. The database platform comprises residential and industry requirements processed, analyzed, and distributed to their corresponding consumers for energy production at the terminal building.

Structural Assembly of Data

The estimation level of energy usage plays a crucial role in the model, in which consumers have a resource-restricted system for sustainable energy forecasting. Energy supplies and their associated information fall within the assets sufficiently to operate and monitor the system facility. A network is a protected position where users with different items, such as the consumption stage, can transmit renewable resources. A digital system with an adequate system for energy production protects energy usage and additional loss. Standard utilities provide challenging consumers with accessible electricity, lacking knowledge regarding consumption, changing climate, and several other conditions resulting in low energy use.

The architecture of the DLSDSS is shown in Figure 1. The data sources are collected from the building operation of data. The sustainable decision system has the correct stream of data flow between buildings, and the deep learning method allows the big stream of data to take part in buildings. In comparison, a smart building tracks and delivers energy requirements appropriately using remote sensing. However, systems typically display reduced productivity because they are crowded or do not conserve energy requirements associated with data. Hence, no framework is given to identify irregular building energy requirements. Developers deal with this problem through an intermediary system management model whereby inventory levels are handled in several analytical steps until they are moved onto the intelligent grids. The potential load prediction for building in response to its requirement distribution and energy collection shows a sample resource distribution situation with the suggested system:

$$Z(m)=P^{(m)}+(z^{(k)}-z^{T}h^{(k)})-\mathrm{T}_k(h)S_m(h)-(z^{(m)}-z^{m}h^{(k)}) \quad (1)$$

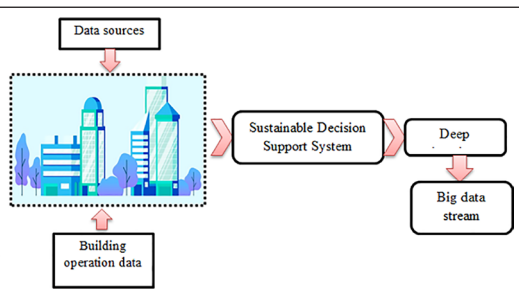

Figure 1. The architecture of the deep learning–based sustainable decision support system.

The resource data $Z(m)$ used in building $P^{(m)}$ with moments is an entry to the model parameters $z^{(k)}$, producing energy consumption $z^{T}h^{(k)}$ for the next few hours. The building has developed a resource-compact system $\mathrm{T}_k(h)$ of prediction. It gives the source data $S_m(h)$ for 3 hr and foresees a potential use of single data $z^{(m)}$. The building sends the data to the central server $h^{(k)}$, storing and analyzing the query for an irregular search with records. An unexpected variability of domestic or building production can lead to a disorder. The power panel addresses the demand and delivers energy in all sectors with easy deployment over the central server and spins easily. The remote sensing technology consequences include the energy generation forecast using a limited energy system with lower failure rates and optimized estimation. The final training set, usable in real-life scenarios, requires several phases. As stated below, the initial step is to prepare fresh data from an acquired data set and achieve the optimum solution with the deep learning mechanism.

Data Gathering from the Sensor

Actual energy data include many sampling variables, such as dates, time, real and reactive strength, energy, and so on. The digital meter works in a unified official list to link the cables of various devices or machines. Usually, a week or a year is obtained because it is subject to various problems, including consistency, lack of attributes, lengthy conditions, and so on. Such failures are caused by system failures, resource depletion, calculation issues, and accidents of persons. Therefore, the electrical energy data require remote sensing techniques for cleaning and data uniformity to improve refining and performance. Several preprocessing strategies are used for testing practices to sterilize the data. The incomplete data are deleted, and the intentional data are retrieved. The main benefit is that extraordinary odd numbers are disgraded, impacting the variety of regular variables and shifting the specifications toward a maximum or minimum range. Normalization would be the next significant preprocessing step. The best normal transformation collection is implemented for several procedures. These standardization methods involve centroid data type, regular data type, scalar, transforming quantities, and transformers of energy:

$$w_s^t(f)=\sqrt{(H[(X_r-f(z)+G[X_r+f]\sqrt{M_r})]+G[X_r+f(z)])} \quad (2)$$

Many data points $w_s^t(f)$ lie among one in standard data X_r and can play an important role in the accurate training stage H. Finally, simple charge modeling $f(z)$ is concerned with transforming the initial (buildings and industrial) data collection M_r into small durations G. Data preprocessing strategies over actual data formats improve estimation efficiency for both databases. The ANN can be considered a growth-based classification system. ANNs recognize only one input, and in comparison, ANN inputs and analyzes the sequence of trends at numerous times, as shown in Equations 3–5:

$$j_s=\delta(u_s[g_{s-1},\mathrm{y}_s]+d_s) \quad (3)$$

$$e_s=\delta(u_e[g_{s-1},\mathrm{y}_s]+d_e) \quad (4)$$

$$v_s=\delta(u_v[g_{s-1},\mathrm{y}_s]+d_v) \quad (5)$$

The ANN input j_s, e_s, v_s and analysis of the sequence of trends at numerous times g_{s-1} is obtained from Equations 3–5. An artificial input layer of a neural network is responsible for bringing in the initial data, which are then processed by successive artificial neurons. The ANN's input layer is the first step in the process. When high-frequency fluctuations have been filtered out of a time series, only low-frequency changes contribute to the trend. δ represents the data sharing parameter, u_s, u_e, u_v represent the actual contribution of the data formats, and d_s, d_e, d_v represent the efficiency of both databases. The data sharing format distribution is shown in Figure 2.

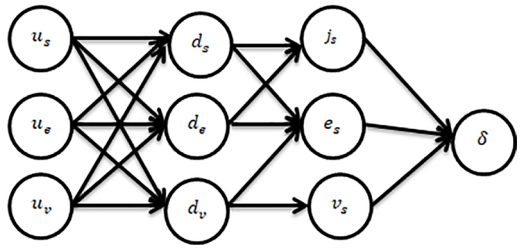

Figure 2. The data sharing format.

The ANN accepts data and outputs when the differential issue disappears and forgets the long results. In real term sequence data, the ANNs still experience tough times though communicating information through previous documents. For example, producing a long series of pure energy data can lose valuable data. This analysis incorporates two key assumptions. The first assumptions have calculations based on a nonlinear effect on building energy demands, and its effects on energy consumption rely on time delays. As per this statement, ANNs and their derivatives must be suitable for building a simple energy load forecast. A further concept of a projected situation is from established training environments. The more unreliable energy data focus on this proposed hypothesis to evaluate template precision improvements with the calculated separation adjustments. Data are gathered regarding building activities and environmental weather data. First, the gathered data are used to build a hybrid charge forecasting model. In the ANNs or versions thereof, the time interval with time lags smaller than indicated are implemented to retrieve new functions.

The parameter characteristics are used to train an ANN for the energy prediction of buildings. The ANN algorithm for the production of timing sequence data is an extremely successful deep learning algorithm. It is an enhanced model to solve the issue of the disappearance or explosion of the ridges. It can transform the set series into hidden units in an integral active appearance process. Specifically, ANN is implemented with multiple layers to prevent increased energy demands from being calculated, utilizing the essential characteristics of hidden states.

A more complicated neural network is used with the architectures to optimize the derived characteristics for more exact loading. ANN is one of the more effective forms of learning complicated ties between variables guided by data. The identical enhanced services of ANN are incorporated as a hybrid system. ANN shall replace the linear relation, and it has more efficient learning links among the properties derived from and the energy consumption associated with a thick layer. A dynamic forecasting system needs to be developed until determining the perceived maximum lag time.

Observations with periods less than an inherent duration can be chosen as the input of a template for energy-efficiency load estimation in a regular pattern. Temporary quantities that duration delays are smaller than an absolute duration can be chosen as contributions of a building energy charge predictive model's time sequence. This analysis thus requires the use of computation to determine the maximum time delay. A continuous series can be transformed into a spatial domain to a spatial frequency series of the equivalent main group and is shown in Equation 6:

$$Y(l) = \sum_{m=0}^{(M-1)} y(m)\left[cos(\frac{2\pi}{M}lm) - j.sin(\frac{2\pi}{M}lm)\right](l = 0,1,\ldots M-1) \quad (6)$$

$$Y(l) = \sum_{m=0}^{(M-1)} y(m)\left[cos(\frac{2\pi}{M}lm) - j.sin(\frac{2\pi}{M}lm)\right] \quad (7)$$

The spatial transformation domain to a spatial frequency series $Y(l)$ is obtained from Equations 6 and 7 and is explained in Figure 3. The most influential time M is determined based on the formula $M = 1/f$ with frequent f of peak distance.

The study considers the most influential duration the maximum significant delay M–1 for time series analysis. Then $y(m)$is the mth amount in the transfer function series, and $Y(l)$ represents the lth variable in the spatial frequency series of M values. Frequency-domain charts indicate exactly how much of a signal is contained within each band of frequencies, whereas a time-domain chart depicts how the signal evolves. Networking, geology, remote sensing, and image processing require frequency-domain analysis. In contrast to time-domain analysis, frequency-domain analysis focuses on how a signal's energy is spread throughout various frequencies. In particular, the complex nature, not specifically stated, can be the framework of the established information-driven load estimation method. Response testing is a highly efficient methodology to measure the influences on the predicted results of variables. It has been used in many ways, such as in operations management, renewable energy development, and processing.

An approximate solution can calculate the dependency of an estimation method on input data. The approximate solution of large systems is difficult to measure, and countable derivative approximations are an effective solution for replacing the conditional component. The effect of input data on expected energy charges is measured using

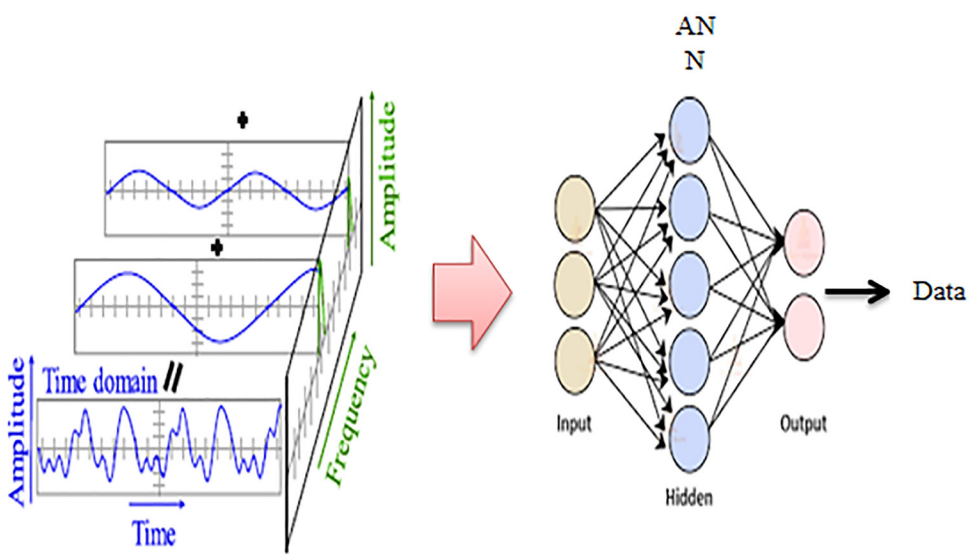

Figure 3. The time domain and frequency domain for data distribution.

a dimensional response spectrum table shown in Equation 8. The larger the input figure's intensity function, the more the input effect increases:

$$R(Y_j) = \frac{1}{2M}\sum_{L=1}^{l}\left|\frac{g(Y_1,\ldots(1+L\times\Delta)\times(Y_j,\ldots,Y_m)-g(Y_1,\ldots,Y_j,\ldots,Y_m)}{L\times\Delta\times g(Y_1,\ldots,Y_j,\ldots,Y_m)}\right|(L\neq 0) \quad (8)$$

The effect of input data on expected energy charges $R(Y_j)$ is measured using a dimensional response spectrum table obtained from Equation 8. Thus, $R(Yj)$ represents the measure of the dimensional resistance of the input. Here $(Y_1,\ldots.Y_j,\ldots\ldots Y_m)$ represents the performance of all inputs that have a starting point. The training of the data method is illustrated in Figure 4. Ym represents the output if Y_j is increased by L and other parameters are kept constant.

We conjecture that the only data relevant to forecasting in the training data comes from remote sensing information. . In building control, energy systems do not work continuously because of the deterioration of the device/efficiency, construction user changes, and external environment adjustments. Under such circumstances, data-guided systems cannot be applicable. While there is widespread agreement on construction, the empirical explanation of template observation often lacks an efficient tool. One of the main factors is that there are no approximate empirical indices for the discrepancy between a forecast situation and defined standard situations. The distance between two buildings is a popular chart for mathematical estimations, the calculation for which is specified in Equations 9 and 10:

$$b(Y_1, Y_2)=\sum_{(p=1)}^{m}(Y_{1p}-Y_{2p}) \quad (9)$$

$$B(a,b) = (1-u_x)\sum_{(p=1)}^{m}\left(\frac{R(y_p)}{\sum_{(l=1)}^{m}R(y_p)}\times|Y_{ap}-Y_{bp}|+u_x\times(X_a-X_b)\right) \quad (10)$$

The distance between the two buildings is obtained from Equations 9 and 10; Y_1,Y_2 represents the distance between two building locations. It misleads clients, as any feedback is believed to get the same value.

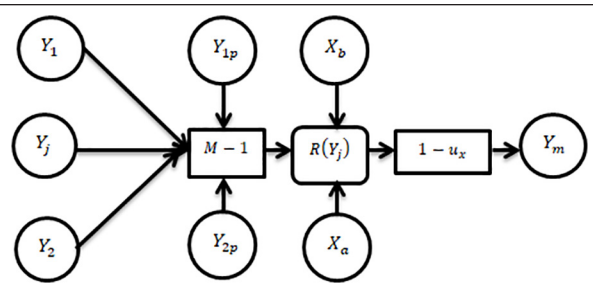

Figure 4. The training of the data method.

For example, suppose that an entry has a tiny effect on the developed model and has different preferences in two groups and that some other input data in the two situations are quite close. $B(a,b)$ represent the empirical indices for the discrepancy between a forecast situation, Y_{1p}-Y_{2p} represent the standard situations, u_x represents the widespread agreement on the construction, and Y_{ap},Y_{bp} represent the external environment adjustments. Here, $b(Y_1,Y_2)$ is the range from Y_1 to Y_2 measured as the building resources set, p represents the tolerance of model input, and y_p represents the position of the energy load. The input data and distance between buildings is shown in Figure 5.

The data center of such an analysis is a public building and contains many rooms, including meeting rooms, office buildings, libraries, and restaurants. A flask obtains weights in the season with a sample duration based on building refrigeration. Historical information is collected through two main environmental parameters: ambient air temperature and outdoor air moisture. Such data are used to determine the efficiency of the methods proposed. Values measured are those supplied by an instrument or equipment that measures the measurand's value. As a product of the numerical value and unit, it is employed in metrology applications and provided in percentages.

The actual significant delay measures for correlations, namely, the subject information approach, and the quantitative tests have three of the most common function extraction strategies. Actual significant delay calculations are often incorporated directly into forecasting, lacking extracting the features as control units. However, traditional techniques of processing characteristics are not acceptable. The remote sensing data set can be transformed into a collection of hidden units to practice underlying period series mechanics machine learning removal. In addition, two specific empirical approaches are chosen as two benchmarks and the above data-led prediction approaches.

The template inputs for the prediction of chilling duties are chosen for three types of variables. It helps clarify the effect on building refrigerant loads from indoor occupation trends. There is an effect on constructing passive cooling on certain outdoor conditions, such as wind and solar output. The traditional building refreshment cargos, which represent radiant fatigue factors, are represented with the current method. Such data are usually standardized by regularization to ensure that parameters with original wide scales with originally limited quantities are not overweighted. The analyzed data consist of selected features, such as raw data, field data, and quantitative training data. The raw function set is designed as a comparison group. There is already increasing importance given to the usability of data-driven systems.

Figure 6 shows the energy building with remote sensing technology. Local energy production and consumption should be integrated into the energy transition that has been launched by the government policy and the rising influence of renewable energy consumption in the building. There can be no successful energy management system without an efficient, dependable, and cost-effective system in place. Electrical energy and heat energy used to heat and to heat water in buildings must be sourced from sources that emit less carbon dioxide.

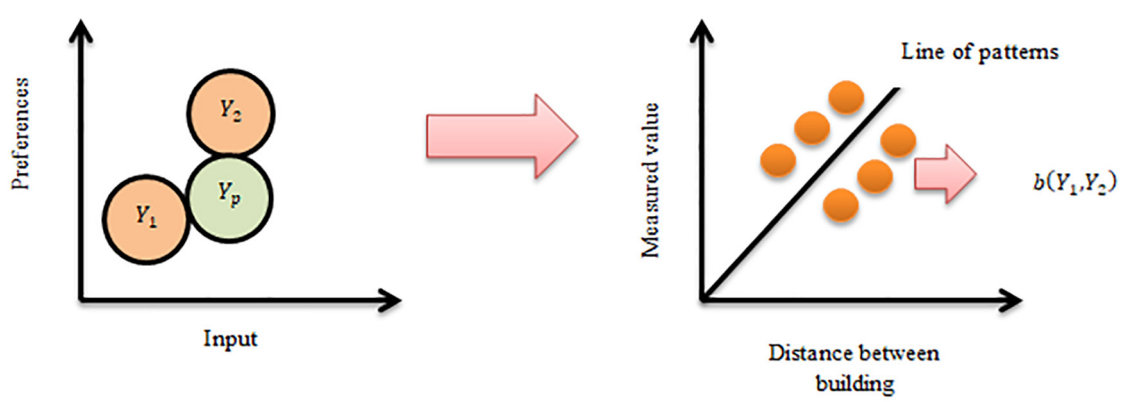

Figure 5. The input data and distance between buildings.

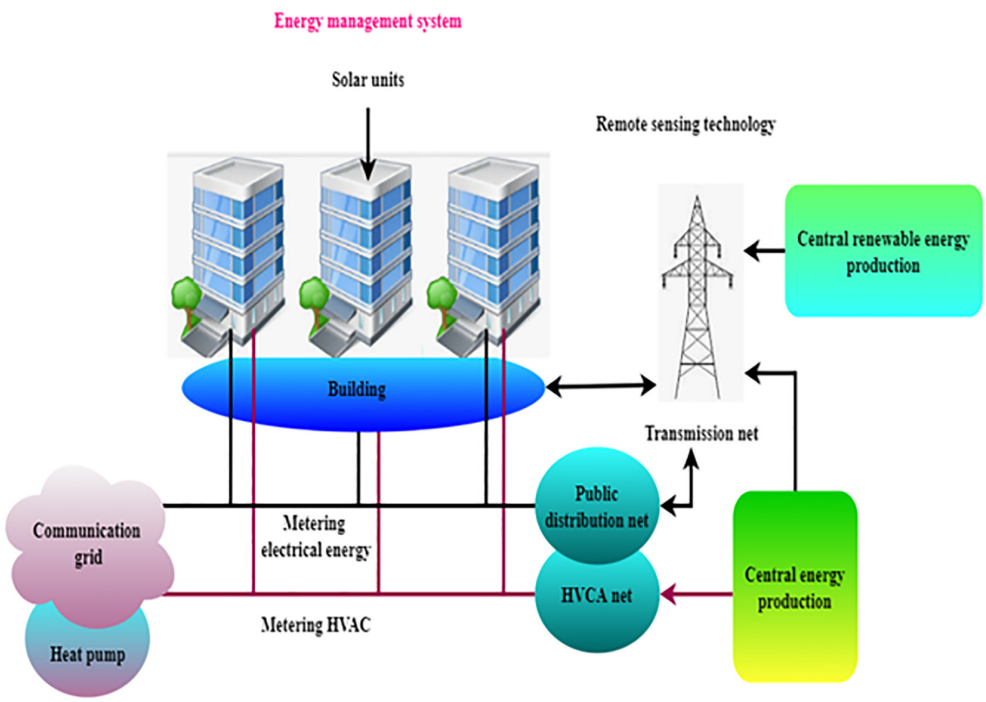

Figure 6. Energy building with remote sensing technology.

Other tasks in a contemporary property must be digitally solvable and cost effectively accomplished. Radio technology generates local data in smart buildings and smart cities via distant sensors, actuators, and meters. Application server and Internet deployment should be handled by central transmission through gateways for data transfer. It is possible to control local date production using software platforms connected to various remote sensing technologies.

Creating genuine value for inhabitants and administrations with innovative applications is at the heart of the digitalization of buildings. The green energy source is supplemented by large-scale wind and solar projects. District heating networks, which use the combined heat and electricity of many facilities, can distribute heat to nearby properties. Today, solar panels on rooftops combined with heat and power units in basements are the most common decentralized energy sources. Heat pumps and hydrogen synthesis using fuel cells are other essential local power-generating methods. Increasing self-sufficiency is made possible by electrical storage devices, which dissociate energy generation from consumption. It is necessary to utilize energy management systems to manage both the purchase and the feed-in of electricity from and into the public distribution grid to monitor both distributed and centrally supplied power.

Due to the sophistication of current models and deep learning training techniques, the connections among building energy burdens and dependent factors can be very complicated. It makes the subject information very hard to describe. It also raises the risks of incorrect choices relying on estimation techniques based on research in several sectors, such as public administration and electricity delivery. Very minimal solutions were suggested in the construction industry to allow consumers to recognize data-driven modeling.

Results and Discussion

The proposed DLSDSS has been validated based on data accuracy and energy consumption rates to better plan smart infrastructures and services. First, the sophistication of building energy sources and the existence of data-predictive models make uncertainty inevitable. These insecurities can lead to an incorrect forecast of energy consumption. The uncertainties of building energy load forecasting are quantified and clarified. Second, efficient and effective maintenance for energy building is useful for energy efficiency and emissions reduction. DLSDSS accomplishes a more efficient and successful management of energy sources, such as optimization techniques and energy-saving methods. The test and training data are determined to describe the decline in model efficiency experimentally. Residually projected building models depend primarily on two dependent variable energy loads experienced and energy loads projected. The energy loads measured in each building and the weighted difference among testing conditions and the learning environment create the data transfer rate. The data accuracy rate is shown in Figure 7.

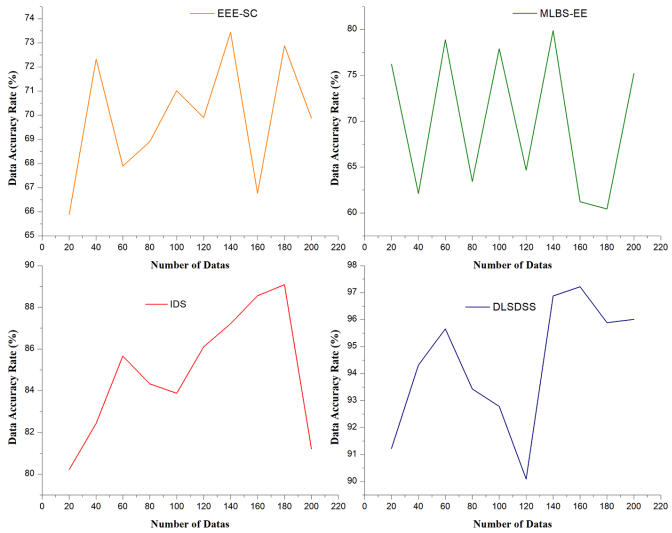

Figure 7. Data accuracy rate.

Accurate time sophistication of a qualified system is a difficult and complex activity and requires great accuracy, especially when a concept is introduced over resource-constrained machines. Consequently, a thorough time complexity evaluation is carried out with significant emphasis on the model performance and its implementation period. The suggested management approach, as well as other considerations, require contemplation. Since the worked energy prediction discourse fails to concentrate on energy instruments, to make a valid assessment,

the time complexity of DLSDSS is shown in Figure 7. DLSDSS has incorporated and measured the time complexity of these temporal prediction models. DLSDSS would absorb minimal time from all the available alternatives and have the lowest model complexity with accurate performance. The time complexity analysis rate of DLSDSS is shown in Figure 8.

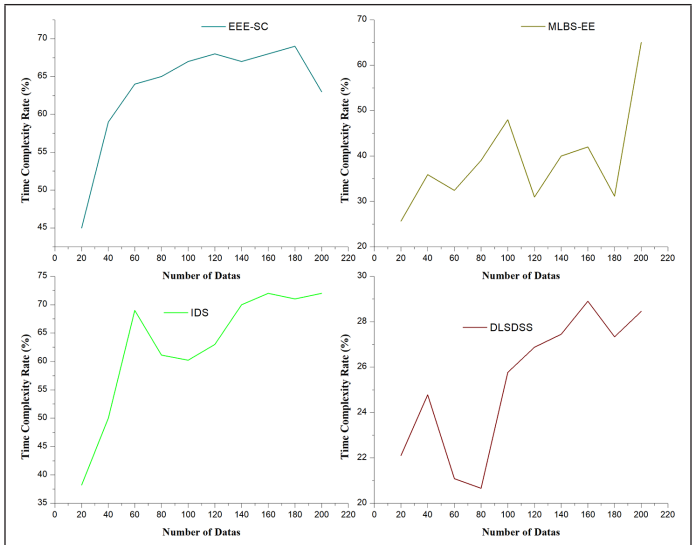

Figure 8. The time complexity analysis rate of the deep learning–based sustainable decision support system.

The data distribution framework is approved for a well-known industrial data set with the experimental analysis to approve the proposed structure for business and residential buildings. By studying the program's statements, one can estimate the program's time complexity. It is important, though, that people pay attention to how the assertions are ordered. Let us pretend they are in a loop, making function calls or even going backward. The building structure is the local data distribution in the DSS of the smart cities' buildings. It is essential for energy to be distributed to different locations. Data gathered among the cities are calculated daily. The DSS calculates the data distribution rate for all buildings. The DLSDSS model's predictive performance against real-life testing data is observed on these given data, where a small gap of 40 to 80 minutes can be observed. The majority of the attributes are strongly conflicting, which indicates that the proposed model is more accurate. The data distribution rate is shown in Figure 9.

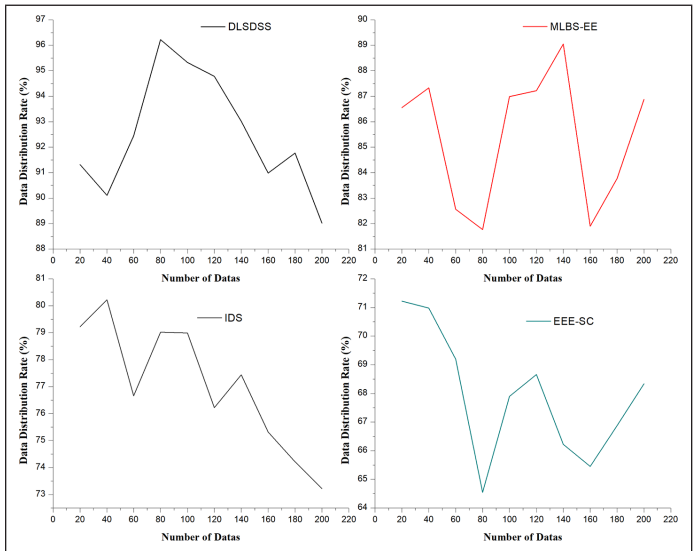

Figure 9. The data distribution rate.

The efficient and accurate utilization of energy capital, especially local energy materials, is becoming a critical feature of the latest smart city model in the modern setting of smart cities. In that context, preparing the energy supply could help make cities increasingly efficient. Data distribution is a function or a list of all the potential values (or intervals) of the data found, and it informs users about how often each value happens. Energy is better suited to specific requirements, stressing that potential energy demand would rise due to population expansion. Requirements including energy data distribution were taken into account. Following many experiments, the outcomes have been proved best when all the parameters are used simultaneously. The outcome is satisfactory, and a slight change in event exposure is essential, which does not mean a large increase in the design's difficulty. The energy consumption rate is shown in Figure 10.

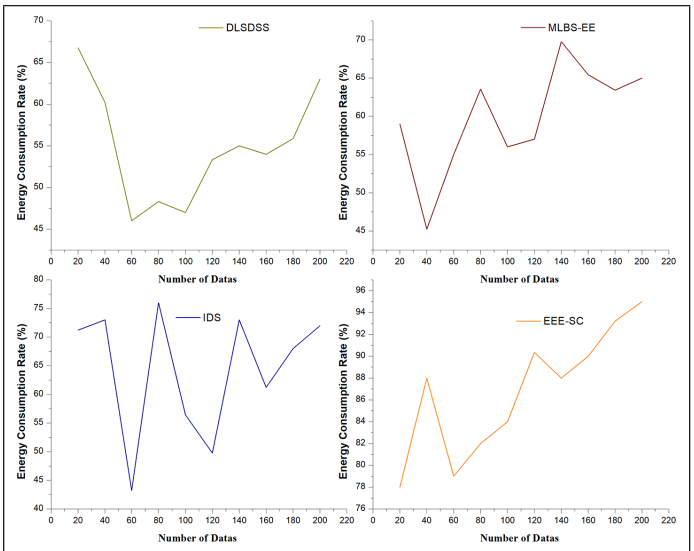

Figure 10. The energy consumption rate.

Switching the energy to several customers makes the whole supply vulnerable, leading to some load shedding. This can perhaps lead to a shortage of electricity or avoid overloading the transmission and distribution networks with remote sensing. Short circuits, substation failure, or damage to the distribution network can cause a power outage. In addition to payment, outage management is a top priority in the use of smart meter data analysis. Detailed information on where to find the notice and proof of the restoration are supplied. Consideration has been given to outage management applications, data requirements, and system integration difficulties. The DLSDSS method improves load shedding management by 95.8% over the existing system. Smart meters have made it simpler to predict where power outages can occur. Figure 11 shows the load shedding ratio.

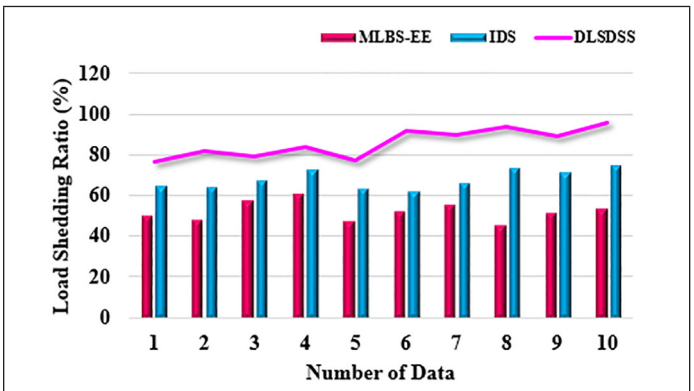

Figure 11. The load shedding ratio.

The energy charging devices are manageable and provided at the edge nodes of smart buildings and apartments with a usable algorithm to the forecast. In the DLSDSS, the pretrained short load prevision system is equipped with a manageable resource-constricted unit. The model received is equipped with established data sets utilizing a

multi-layered support system with effective and accurate performance. The resource-constrained system forecasts the intelligent source's future energy consumption as a connectivity canal using public buildings in smart cities. DLSDSS delivers the energy requested by the server to a particular residential building and business. The energy efficiency of DLSDSS is shown in Figure 12.

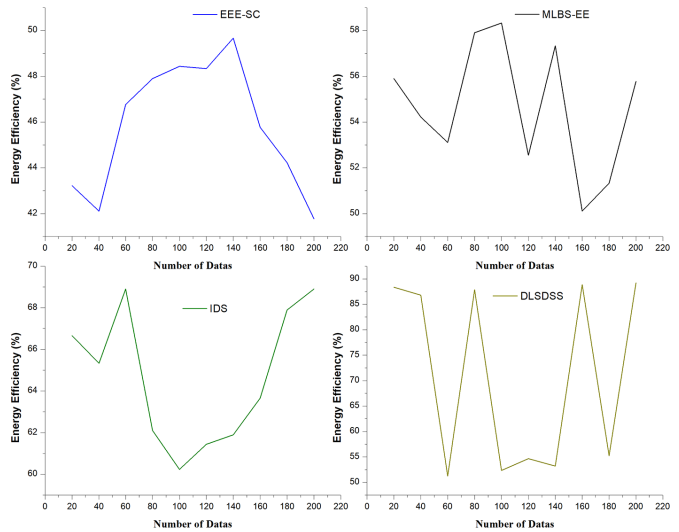

Figure 12. Energy efficiency of the deep learning–based sustainable decision support system.

The proposed DLSDSS achieves the highest data transfer and accuracy rate and less energy consumption rate when compared to the existing economic efficiency and energy security of smart cities, machine learning–based systems for managing energy efficiency, and intrusion detection systems. In the simplest terms, energy efficiency uses less energy to do the same work, thus avoiding waste. Reduced greenhouse gas emissions, reduced need for imported energy, and lower household and economic expenditures are all advantages of improving energy efficiency.

Conclusion

This article presents DLSDSS for energy construction in new technologies in smart cities. DLSDSS proposes incorporating deep learning methods to make decisions about sensor knowledge of the IoT into smart energy houses in energy management. The proposed in-depth learning strategies are used for the energy efficiency classification of buildings. Buildings, particularly those already standing still, emit much carbon dioxide. Using remote sensing services to digitize buildings and generate green energy on-site could be a massive boon to the local economy and the environment. The data obtained from the sensor nodes are used to create smart cities and provide a systematic compilation of information using a deep study method. The profound information algorithm provides a large data stream template for decision makers. The quantitative results reveal that the improved approach decreases energy usage and improves sensor data accuracy by 97.67% with better planning, smart building, and service decisions. The experimental outcome of the proposed method enhances the accuracy (97.67%), time complexity (98.7%), data distribution rate (97.1%), energy consumption rate (98.2%), load shedding ratio (95.8%), and energy efficiency (95.4%).

Table 1. Tabulation of variable declaration.

Symbols	Description
j_s, e_s, v_s	ANN input
g_{s-1}	sequence of trends at numerous times
δ	data sharing
u_s, u_e, u_v	actual contribution of data formats
d_s, d_e, d_v	efficiency of both database
$Y(l)$	spatial frequency series
M	the most influential time
$y(m)$	mth amount in the transfer function series
$R(Y_j)$	measure of the dimensional resistance
$(Y_1,\ldots Y_j,\ldots\ldots Y_m)$	performance of all inputs
Y_m	output
Y_1,Y_2	distance between two building locations
$B(a,b)$	empirical indices for the discrepancy
$Y_{1p}-Y_{2p}$	standard situations
u_x	widespread agreement on the construction
Y_{ap},Y_{bp}	external environment adjustments
$b(Y_1,Y_2)$	range from to
p	tolerance of model input
y_p	position of the energy load
$w_s^t(f)$	data points
X_r	standard data
H	accurate training stage
$f(z)$	simple charge modeling
M_r	data collection
G	small durations
$Z(m)$	resource data
$P^{(m)}$	building with moments
$z^{(k)}$	model parameters
$z^T h^{(k)}$	producing energy consumption
$T_k(h)$	resource-compact system
$S_m(h)$	source data
$z^{(m)}$	potential use of single data
$h^{(k)}$	central server

References

Ahmed, S. H., J. Lloret, D. B. Rawat, M. Guizani and W. Guibene. 2020. Future networking research plethora for smart cities. *Future Generation Computer Systems* 107:863–864. https://doi.org/10.1016/j.future.2019.07.055.

Anthony Jnr, B., S. Abbas Petersen, D. Ahlers and J. Krogstie. 2020. API deployment for big data management towards sustainable energy prosumption in smart cities—A layered architecture perspective. *International Journal of Sustainable Energy* 39(3):263–289. https://doi.org/10.1080/14786451.2019.1684287.

Elavarasan, R. M., S. Afridhis, R. R. Vijayaraghavan, U. Subramaniam and M. Nurunnabi. 2020. SWOT analysis: A framework for comprehensive evaluation of drivers and barriers for renewable energy development in significant countries. *Energy Reports* 6:1838–1864. https://doi.org/10.1016/j.egyr.2020.07.007.

Green, S., A. M. Grant and J. Rynsaardt. 2020. Evidence-based life coaching for senior high school students: Building hardiness and hope. In *Coaching Researched: A Coaching Psychology Reader*, edited by Jonathan Passmore and David Tee, 257–268. New York: John Wiley & Sons. https://doi.org/10.1002/9781119656913.ch13.

Guo, B., J. Chen, Z. Wang, Y. Su, H. Li, H. Ye and J. Huang. 2022. In situ TEM studies of electrochemistry of high temperature lithium-selenium all-solid-state batteries. *Electrochimica Acta* 404:139773. https://doi.org/10.1016/j.electacta.2021.139773.

Hafeez, G., K. S. Alimgeer, Z. Wadud, Z. Shafiq, M. U. Ali Khan, I. Khan, F. A. Khan and A. Derhab. 2020. A novel accurate and fast converging deep learning-based model for electrical energy consumption forecasting in a smart grid. *Energies* 13(9):2244. https://doi.org/10.3390/en13092244.

Hajiabadi, M., M. Farhadi, V. Babaiyan and A. Estebsari. 2020. Deep learning with loss ensembles for solar Power prediction in smart cities. *Smart Cities* 3(3):842–852. https://doi.org/10.3390/smartcities3030043.

Hossein Motlagh, N., M. Mohammadrezaei, J. Hunt and B. Zakeri. 2020. Internet of Things (IoT) and the energy sector. *Energies* 13(2):494. https://doi.org/10.3390/en13020494.

Khan, M., M. Babar, S. H. Ahmed, S. C. Shah and K. Han. 2017. Smart city designing and planning based on big data analytics. *Sustainable Cities and Society* 35:271–279. https://doi.org/10.1016/j.scs.2017.07.012.

Kumar, H., M. K. Singh, M. P. Gupta and J. Madaan. 2020. Moving towards smart cities: Solutions that lead to the Smart City Transformation Framework. *Technological Forecasting and Social Change 153*:119281. https://doi.org/10.1016/j.techfore.2018.04.024.

Li, H., T. Hong, S. H. Lee and M. Sofos. 2020. System-level key performance indicators for building performance evaluation. *Energy and Buildings* 209:109703. https://doi.org/10.1016/j.enbuild.2019.109703.

Liu, T., Z. Tan, C. Xu, H. Chen and Z. Li. 2020. Study on deep reinforcement learning techniques for building energy consumption forecasting. *Energy and Buildings* 208:109675. https://doi.org/10.1016/j.enbuild.2019.109675.

Liu, X., J. Zhang, J. Yin, S. Bi, M. Eisenbach and Y. Wang. 2021. Monte Carlo simulation of order-disorder transition in refractory high entropy alloys: A data-driven approach. *Computational Materials Science* 187:110135. https://doi.org/10.1016/j.commatsci.2020.110135.

Mao, J., Q. Sun, X. Wang, B. Muthu and S. Krishnamoorthy. 2020. The importance of public support in the implementation of green transportation in the smart cities. *Computational Intelligence*. https://doi.org/10.1111/coin.12326.

Mlecnik, E., J. Parker, Z. Ma, C. Corchero, A. Knotzer and R. Pernetti. 2020. Policy challenges for the development of energy flexibility services. *Energy Policy* 137:111147. https://doi.org/10.1016/j.enpol.2019.111147.

Pournaras, E. 2020. Proof of witness presence: Blockchain consensus for augmented democracy in smart cities. *Journal of Parallel and Distributed Computing* 145:160-175. https://doi.org/10.1016/j.jpdc.2020.06.015.

Rahman, M. A., A. T. Asyhari, L. S. Leong, G. B. Satrya, M. H. Tao and M. F. Zolkipli. 2020. Scalable machine learning-based intrusion detection system for IoT-enabled smart cities. *Sustainable Cities and Society* 61:102324. https://doi.org/10.1016/j.scs.2020.102324.

Reddy, K. H. K., A. K. Luhach, B. Pradhan, J. K. Dash and D. S. Roy. 2020. A genetic algorithm for energy efficient fog layer resource management in context-aware smart cities. *Sustainable Cities and Society* 63:102428. https://doi.org/10.1016/j.scs.2020.102428.

Riaño-Vargas, K. A., J. I. Alonso-Echeverri, P. A. Gaona-Garcia and C. E. Montenegro-Marin. 2018. Fuzzy logic-based model for the prevention of structural fires on urban buildings using mobile devices and IoT technologies. Pages 216–221 in *2018 IEEE International Conference on Smart Internet of Things (SmartIoT)*, held in Xi`an, Shaanxi, China. New York: IEEE. https://doi.org/10.1109/SmartIoT.2018.00046.

Roth, J., B. Lim, R. K. Jain and D. Grueneich. 2020. Examining the feasibility of using open data to benchmark building energy usage in cities: A data science and policy perspective. *Energy Policy* 139:111327. https://doi.org/10.1016/j.enpol.2020.111327.

Shu, M., S. Wu, T. Wu, Z. Qiao, N. Wang, F. Xu, S. Arumugam and B. A. Muthu. 2020. Efficient energy consumption system using heuristic renewable demand energy optimization in smart city. *Computational Intelligence*. https://doi.org/10.1111/coin.12412.

Singh, S. K., Y. S. Jeong and J. H. Park. 2020. A deep learning-based IoT-oriented infrastructure for secure smart city. *Sustainable Cities and Society* 60:102252. https://doi.org/10.1016/j.scs.2020.102252.

Strielkowski, W., T. Veinbender, M. Tvaronavičienė and N. Lace. 2020. Economic efficiency and energy security of smart cities. *Economic Research–Ekonomska Istraživanja* 33(1):788–803. https://doi.org/10.1080/1331677X.2020.1734854.

Sztubecka, M., M. Skiba, M. Mrówczyńska and A. Bazan-Krzywoszańska. 2020. An innovative decision support system to improve the energy efficiency of buildings in urban Areas. *Remote Sensing* 12(2):259. https://doi.org/10.3390/rs12020259.

Villamayor-Tomas, S., G. García-López and G. D'Alisa. 2022. Social movements and commons: In theory and in practice. *Ecological Economics* 194:107328. https://doi.org/10.1016/j.ecolecon.2021.107328.

Zekić-Sušac, M., S. Mitrović and A. Has. 2021. Machine learning based system for managing energy efficiency of public sector as an approach towards smart cities. *International Journal of Information Management* 58:102074. https://doi.org/10.1016/j.ijinfomgt.2020.102074.

Zhang, X., G. Manogaran and B. Muthu. 2021. IoT enabled integrated system for green energy into smart cities. *Sustainable Energy Technologies and Assessments* 46:101208. https://doi.org/10.1016/j.seta.2021.101208.

Zhuang, H., J. Zhang, Sivaparthipan CB and B. A. Muthu. 2020. Sustainable smart city building construction methods. *Sustainability* 12(12):4947. https://doi.org/10.3390/su12124947.

WHO'S WHO IN ASPRS

Founded in 1934, the American Society for Photogrammetry and Remote Sensing (ASPRS) is a scientific association serving thousands of professional members around the world. Our mission is to advance knowledge and improve understanding of mapping sciences to promote the responsible applications of photogrammetry, remote sensing, geographic information systems (GIS) and supporting technologies.

BOARD OF DIRECTORS

BOARD OFFICERS

President
Christopher Parrish, Ph.D
Oregon State University

President-Elect
Lorraine B. Amenda, PLS, CP
Towill, Inc.

Vice President
Bandana Kar
Oak Ridge National Lab

Past President
Jason M. Stoker, Ph.D,
U.S. Geological Survey

Treasurer
John McCombs
NOAA

Secretary
Harold Rempel
ESP Associates, Inc.

COUNCIL OFFICERS

ASPRS has six councils. To learn more, visit https://www.asprs.org/Councils.html.

Sustaining Members Council
Chair: Ryan Bowe
Deputy Chair: Melissa Martin

Technical Division Directors Council
Chair: Bill Swope
Deputy Chair: Hope Morgan

Standing Committee Chairs Council
Chair: David Stolarz
Deputy Chair: TBA

Early-Career Professionals Council
Chair: Madeline Stewart
Deputy Chair: Kyle Knapp

Region Officers Council
Chair: Demetrio Zourarakis
Deputy Chair: Jason Krueger

Student Advisory Council
Chair: Lauren McKinney-Wise
Deputy Chair: Oscar Duran

TECHNICAL DIVISION OFFICERS

ASPRS has seven professional divisions. To learn more, visit https://www.asprs.org/Divisions.html.

Geographic Information Systems Division
Director: Denise Theunissen
Assistant Director: Jin Lee

Lidar Division
Director: Ajit Sampath
Assistant Director: Mat Bethel

Photogrammetric Applications Division
Director: Ben Wilkinson
Assistant Director: Hank Theiss

Primary Data Acquisition Division
Director: Greg Stensaas
Assistant Director: Srini Dharmapuri

Professional Practice Division
Director: Bill Swope
Assistant Director: Hope Morgan

Remote Sensing Applications Division
Director: Amr Abd-Ehrahman
Assistant Director: Tao Liu

Unmanned Autonomous Systems (UAS)
Director: Jacob Lopez
Assistant Director: Bahram Salehi

REGION PRESIDENTS

ASPRS has 13 regions to serve the United States. To learn more, visit https://www.asprs.org/regions.html.

Alaska Region

Cascadia Region
Robert Hariston-Porter

Eastern Great Lakes Region
Michael Joos, CP, GISP

Florida Region
Xan Fredericks

Heartland Region
Whit Lynn

Intermountain Region
Robert T. Pack

Mid-South Region
David Hughes

Northeast Region

North Atlantic Region

Pacific Southwest Region
John Erickson, PLS, CP

Potomac Region
Dave Lasko

Rocky Mountain Region

Western Great Lakes Region
Adam Smith

Transformer for the Building Segmentation of Urban Remote Sensing

Heqing Zhang, Zhenxin Wang, Jun-feng Song, and Xueyan Li

Abstract

The automatic extraction of urban buildings based on remote sensing images is important for urban dynamic monitoring, planning, and management. The deep learning has significantly helped improve the accuracy of building extraction. Most remote sensing image segmentation methods are based on convolution neural networks, which comprise encoding and decoding structures. However, the convolution operation cannot learn the remote spatial correlation. Herein we propose the Shift Window Attention of building SWAB-net based on the transformer model to solve the semantic segmentation of building objects. Moreover, the shift window strategy was adopted to determine buildings using urban satellite images with 4 m resolution to extract the features of sequence images efficiently and accurately. We evaluated the proposed network on SpaceNet 7, and the results of comprehensive analysis showed that the network is conducive for efficient remote sensing image research.

Introduction

In recent years, the rapid development of remote sensing technology has significantly improved the spatial, temporal, and spectral resolutions of remote sensing images. As a basic data source for urban planning management and infrastructure construction, remote sensing images objectively and accurately record the comprehensive features of the landscape and the individual features of ground objects. Remote sensing images have been widely used in the evaluation, standardization, decision-making, simulation, and prediction of the future of urban development, thereby providing a true, reliable, and detailed data basis for urban planning and urban construction (Cheng and Han 2016).

The segmentation of buildings based on remote sensing images plays a significant role in urban planning, population estimation, and topographic map production and updating (Erdem and Avdan 2020). Although the accuracy of extracting building information using manual surveying and mapping methods is high, it exhibits low efficiency and is expensive, and the current situation cannot meet the application requirements. Urban expansion and urban environmental assessment and monitoring are hot research topics worldwide. Owing to issues like dense urban buildings, complex urban background environments, and a large amount of remote sensing image data, the traditional feature extraction methods have not been automated yet. The semantic segmentation of urban buildings has been a challenging task (Mahabir *et al.* 2018). High-resolution remote sensing images can clearly express the texture details and spatial structural characteristics of ground objects. Therefore, the automatic extraction of building information based on high-resolution remote sensing images has become a research hotspot.

Heqing Zhang, Jun-feng Song, and Xueyan Li are with the State Key Laboratory on Integrated Optoelectronics, College of Electronic Science and Engineering, Jilin University, 130012 Changchun, China (leexy@jlu.edu.cn).

Jun-feng Song and Xueyan Li are also with Peng Cheng Laboratory, No.2, Xingke 1st Street, Nanshan, Shenzhen, China.

Zhenxin Wang is with Jilin Xiangyun Information & Technology Co., Ltd.

Contributed by Sidike Paheding, October 5, 2021 (sent for review January 25, 2022; reviewed by Cary Cox, Abel Andres Reyes-Angulo).

With the successful application of deep learning methods to the field of computer vision, excellent analytical capabilities have been demonstrated with regard to remote sensing image analysis. This study focuses on a precise semantic segmentation model for urban remote sensing building images. The contributions of this study are as follows:

(1) Inspirited by Liu *et al.* (2021), we developed a building segmentation network based on a remote sensing image using Swin Transformer.
(2) Based on the model, the semantic segmentation of buildings and dynamic analysis of urban buildings were realized.

Related Work

As the convolution neural networks (CNN) architecture achieved significant results in image classification tasks (Krizhevsky *et al.* 2012), the classification network was developed as a fully convolutional neural network (FCN) (Long *et al.* 2015) for semantic segmentation. The FCN model, which is the mainstream method in the field of computer vision, is widely used for remote sensing image segmentation. The semantic segmentation of remote sensing images helps group pixels according to the semantic information expressed in the image to obtain segmented images with pixel-by-pixel semantic annotations; this is one of the key tasks associated with remote sensing image analysis. Semantic segmentation models include SegNet (Badrinarayanan *et al.* 2017), U-Net (Ronneberger *et al.* 2015), and other variants (Zhou *et al.* 2018; Çiçek *et al.* 2016). The urban building extraction method (Pan *et al.* 2020; Soni *et al.* 2020) has gradually developed into a network model based on the U-Net network codec (encoding and decoding structure), which is a research mode in the field of deep learning, with various application scenarios. Figure 1 shows the most abstract representation of the codec framework used in the field of image processing.

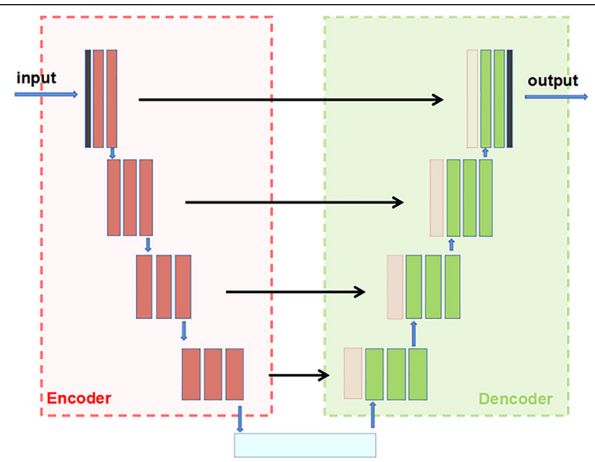

Figure 1. Encode-decode codec structure for semantic segmentation.

Photogrammetric Engineering & Remote Sensing
Vol. 88, No. 9, September 2022, pp. 603–609.
0099-1112/22/603–609

doi: 10.14358/PERS.21-00076R2

In the neural network backpropagation, the gradient will continue to decrease and eventually tend to zero when the gradient is passed from the back to the front. As a result, the weights of the shallow neural network cannot be updated, and the learning rate of the previous hidden layer is lower than that of the subsequent hidden layer. That is, as the depth of the network increases, the accuracy decreases, a phenomenon called vanishing gradients. To solve this issue, a deep residual framework (ResNet) (He *et al.* 2016) was proposed to ensure that the gradient is propagated from the top to the bottom of the network during the backward propagation process. Yi *et al.* (2019) compared the DeepResUnet model to other architectures. Moreover, multitasking in machine learning is used for building segmentation; for example, Hui *et al.* (2018) used a multitask deep neural network to extract the unique features of buildings. Since the attention mechanism has achieved remarkable results in computer vision tasks, this type of network is gradually being adopted in the field of remote sensing image intelligent analysis. Pan *et al.* (2019) used a generative adversarial network model with spatial and channel attention mechanisms to select useful features. Pan *et al.* (2019) and Zhou *et al.* (2020) combined U-Net and the attention mechanism to realize high-precision building segmentation. Encoding and decoding structures have been highly effective in image segmentation tasks in various fields, where the encoder plays an important role by learning the global context representation, which will be further used by the decoder for semantic output prediction. Despite its success, the limitations of the convolution layer, the main building block of CNNs, limit the ability to learn remote spatial correlations in such networks. The pictures in the SpaceNet 7 data set have high similarity and few samples, and it is easy to appear that the overfitting on the training data is much higher than that of the test data. In this study, we used a vision transformer (Vaswani *et al.* 2017; Dosovitskiy *et al.* 2020) as an encoder to learn the sequence representation of the input and effectively capture global multiscale information. The transformer encoder was connected to the decoder through the skip connections of different resolutions to calculate the final semantic segmentation output.

The use of transformers in the field of computer vision has two issues. First, based on the transformer model, the length of the token is fixed (in natural language processing (NLP)). There is no issue with NLP words; however, the proportion of visual elements is different in the field of computer vision. Second, image pixels require higher resolution than words in text. The computational complexity of traditional self-attention is the square of the image size, which leads to the problem of pixel-level dense prediction. Since the emergence of Vision Transformer (ViT) (Dosovitskiy *et al.* 2020), although various visual transformers are being constantly developed, most models face the issues of complex training and low efficiency. Swin Transformer (Liu *et al.* 2021) drastically reduces computational complexity. In this study, we process the building segmentation of remote sensing images by combining the aforementioned methods. Inspired by Liu *et al.* (2021), a shifted window has been used to segregate the regional image, aiming to solve the problem of window boundary discontinuity caused by the feature map division. We have extensively validated the proposed model using open-source remote sensing image data sets. Experimental data based on the open-source data sets show that the proposed method is comparable to the leading methods.

Materials and Methods

SpaceNet 7 Data Set

The SpaceNet 7 data set (Van Etten and Hogan. 2021) (additional data can be found at https://spacenet.ai/sn7-challenge/) includes high-definition remote sensing images and annotations of ~101 locations worldwide and provides a sufficient and reliable data source for the rapid spatiotemporal dynamic monitoring of urban construction land. Each location provides 24 images for two years (one per month). The imagery in the SpaceNet 7 data set comprises red, green, blue, alpha color at medium resolution (~4 m). SpaceNet 7 is an open-source data set that is free to download. Within two years, each geographic area experiences significant urban changes. It provides a sufficient and reliable data source for the rapid spatiotemporal dynamic monitoring of urban construction land. SpaceNet 7 contains images whose total combined area is >40 000 km2. Moreover, the data set includes images with detailed polygon labels of the outlines of buildings, amounting to

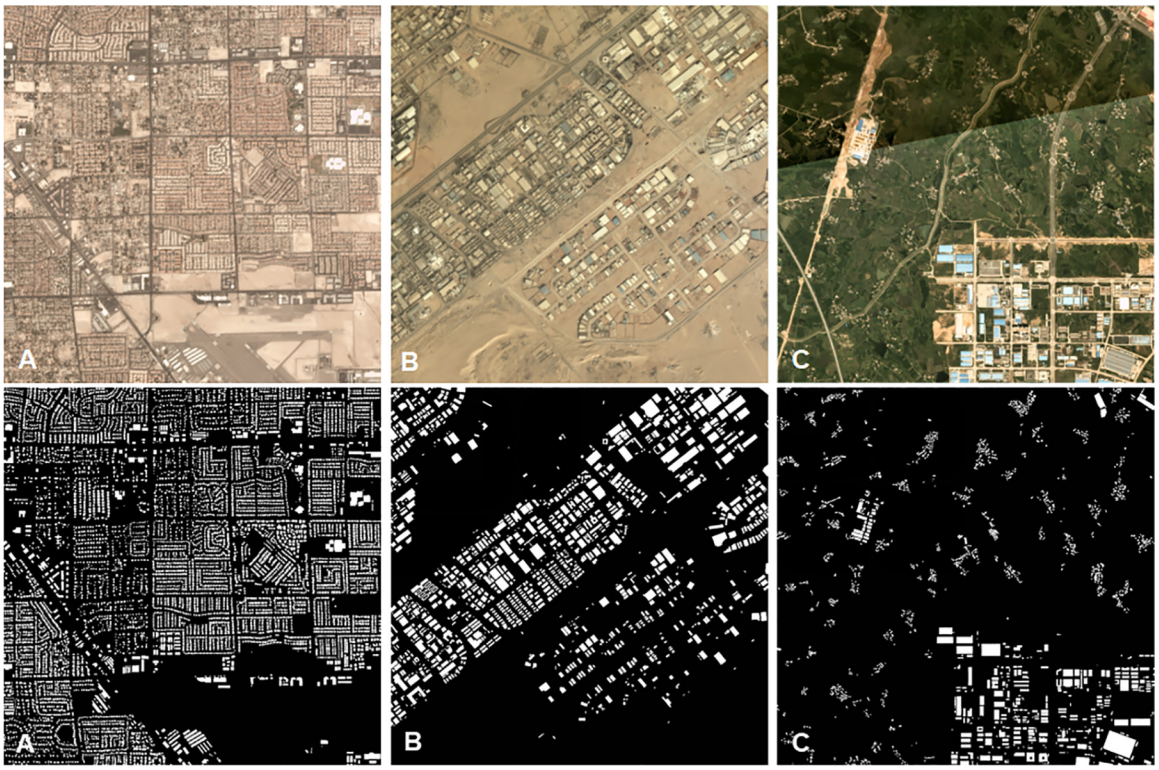

Figure 2. (a), (b), and (c) are the original images (top) and their annotations (bottom) of SpaceNet 7.

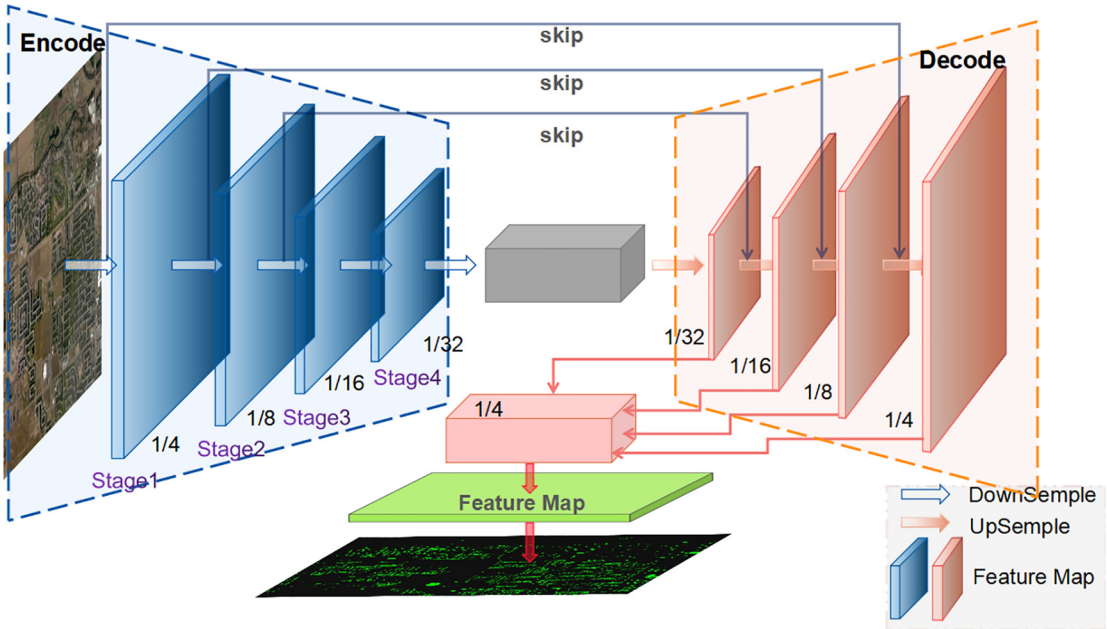

Figure 3. ***SWAB-Net*** architecture.

more than 10 million individual annotations. This represents a much higher label density compared with that of natural scene data sets, e.g., Common Objects in Context (COCO), or overhead drone video data sets (Van Etten and Hogan 2021). The open-source data set-SpaceNet 7 used in this study well compensates the following shortcomings: (1) individual researchers will spend a lot of energy on collecting experimental data, and (2) the use of various non–open-source databases have limited the quantitative comparison of theory and methods, thus hindering the rapid development of remote sensing deep learning. To better observe the labeling situation, we visualize the original images and their annotations, white buildings, and black background, as shown in Figure 2.

Methods

This study proposed the shift window attention of building ***SWAB-Net*** model, which includes the benefits of the transformer (Lin *et al.* 2017; Singh and Davis 2018) and codec (Ronneberger *et al.* 2015) structure and is a powerful alternative to remote sensing image segmentation. Figure 3 shows the end-to-end segmentation network of ***SWAB-Net*** with SpaceNet 7 images as the input and the segmentation prediction as the output.

The encoder is based on the self-attention of shift windows to complete the hierarchical extraction of image features, and the decoder is based on the multi-feature layer fusion of the spatial pyramid model to complete the semantic segmentation task.

Encoder

The encoder part is similar to the reverse operation of the Pixel Shuffle (Shi *et al.* 2016). The detailed parameters of the encoder are listed in Table 1. For example, downsampling is used to reduce the resolution, adjust the number of channels, and form a hierarchical design, while saving a certain amount of calculation. Each down sampling is performed twice so that interval 2 selects elements in row and column directions, concatenates them into a tensor, and finally expands. At this time, the channel dimension will be four times the original size (height and width are reduced by two times), and then the channel dimension will be adjusted to twice the original structure size by a fully connected layer (Figure 4).

In contrast to the traditional multi-head self-attention (MSA) module, ***SWAB-Net*** is constructed based on the translation window. Two consecutive ***SWAB-Net*** blocks are shown in Figure 5. Each block includes a LayerNorm (LN) layer, multi-head self-attention, residual

Table 1. Detailed architecture specifications.

	Stage1	Stage2	Stage3	Stage4
DownSample.r	4×	8×	16×	32×
Output Size	56×56	28×28	14×14	7×7
Concat, dim	4×4, 128	2×2, 256	2×2, 512	2×2, 1024
LN, Win.size	×2, 7×7	×2, 7×7	×18, 7×7	×2, 7×7

Note: "DownSample.r" = downsampling times; "Output Size" = size of the output of each stage; "Concat, dim" = size of downsampling and dimension; "LN" = the number of times LayerNorm is performed; "Win.size" = the size of the window.

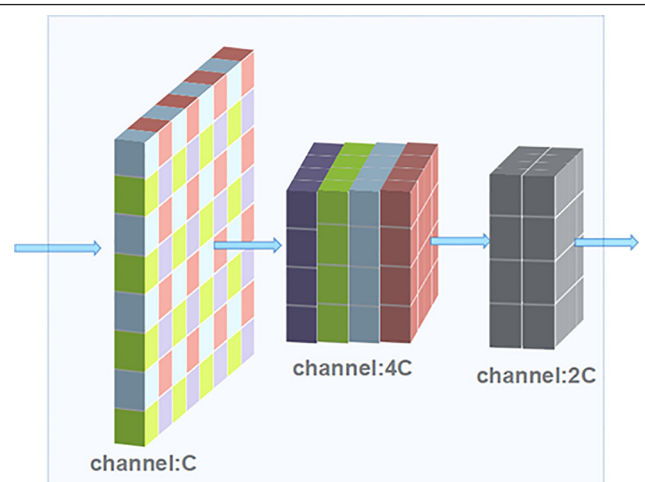

Figure 4. Downsampling of each stage.

connection (Zhang *et al.* 2020), and two Multilayer Perceptrons (MLPs). The window-based MSA (W-MSA) and shifted window-based MSA (SW-MSA) modules are used for transformers.

The local window adopts the nonoverlapping dicing, which adopts the method of cooperation between the shift and local windows, overcoming two significant issues: first, image cutting will cause the loss of information between the windows, and the shift window contains the information lost by the cut in the local window; second, the calculation complexity is reduced from the exponential multiple of the pixel value

to a linear multiple. At the same time, the shift window introduces a new problem, i.e., the number of windows has roughly doubled from the original four windows to nine windows of various sizes. Therefore, a solution has been proposed; it is realized indirectly by shifting the feature map and setting the mask for attention, which can maintain the original number of windows, and the final calculation result is the same (Figure 6).

As shown in Figure 6, the first module uses a regular window to divide the policy. Starting with the upper left pixel, the 8 × 8 feature map is evenly cut into four 4 × 4 windows. At this point, the local window size M is four, as indicated by the purple box. Then, the next module adopts the window configuration shifted from the previous layer, i.e., the regular division window is cyclically shifted to the bottom right by ($M/2 \times M/2$) pixels, as indicated by the change in the position of the purple box in the figure. By adopting the shift window division method, the two consecutive Swin Transformer Blocks, as shown in Figure 6, can be calculated as Equation 1.

$$\begin{aligned} \hat{Z}^{L} &= \text{W-MSA}\left(\text{LN}\left(Z^{L-1}\right)\right) + Z^{L-1}, \\ Z^{L-1} &= \text{MLP}\left(\text{LN}\left(\hat{Z}^{L}\right)\right) + \hat{Z}^{L}, \\ \hat{Z}^{L+1} &= \text{SW-MSA}\left(\text{LN}\left(Z^{L}\right)\right) + Z^{L}, \end{aligned} \tag{1}$$

where, $\hat{Z}^{L}$ and Z^{L}, respectively the output characteristics of the SW-MSA module and the output characteristics of the MLP module of the Lth block (Figure 5). The shift window division method introduces a connection among previous non-overlapping adjacent windows.

Pyramid Pooling Module

The pyramid pooling module (PPM) (Zhao *et al.* 2017) is a four-layer structure with bin sizes of 1 × 1, 2 × 2, 3 × 3, and 6 × 6. A block diagram of PPM is shown in Figure 7. To further reduce the loss of contextual information among subregions, we propose a hierarchical global prior structure that contains information of different scales and subregions. The global scene prior information can be obtained on the final layer feature map of the deep neural network (Lin *et al.* 2017).

The output of a single global pooling bin at the coarsest level (Yu *et al.* 2018). The pyramid branch divides the feature map into different subregions and collectively represents different locations. The output of the different levels in the pyramid pooling module contains feature maps of different sizes. To maintain the weight of the global characteristics, if there are N levels in the pyramid, a 1 × 1 convolution layer is used after each level to reduce the number of channels of the corresponding level to $1/N$ of the original number. Then, the low-dimensional feature map is directly upsampled through bilinear interpolation, and a feature map with the same size as the original feature map is obtained. Finally, the features of the different levels were concatenated as the final global feature of pyramid pooling.

Decoder

The decoder module is used to gradually restore the spatial information of the feature map. The network structure designed in this study is based only on the feature pyramid network (FPN) architecture. After four downsampling iterations, the smallest feature map has a scale of 1/32 of the original image; therefore, it can retain more local details of the road. Under a relatively shallow network structure, the high-level, medium-level, and low-level semantic features are merged through the jump operation, so that the final output feature map can express the semantic information and detailed information of the building. There are still problems with the FPN architecture, although the theoretical receptive field is large, the actual receptive field is much smaller than the theoretical receptive field. Therefore, the PPM is introduced in the last layer of the backbone network and sent to the branch of the FPN to overcome the limitation of the receptive field.

The feature map output by each stage in the network (Lin *et al.* 2017) is recorded as (C2, C3, C4, C5), and the feature maps output by FPN are (P2, P3, P4, P5), where P5 is the feature map directly generated after PPM. The downsampling rate is (4, 8, 16, 32), the feature map of each stage has entities drawn in the network structure, and the

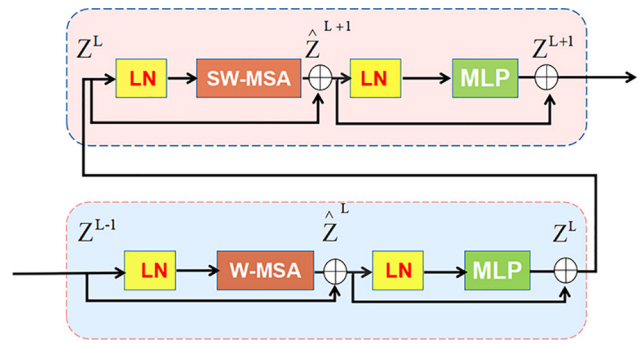

Figure 5. Self-attention blocks based on the shifted window.

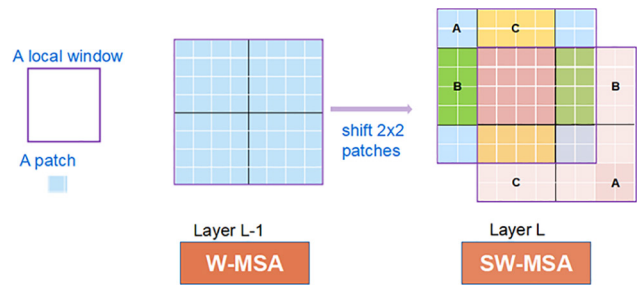

Figure 6. Feature map shift operation.

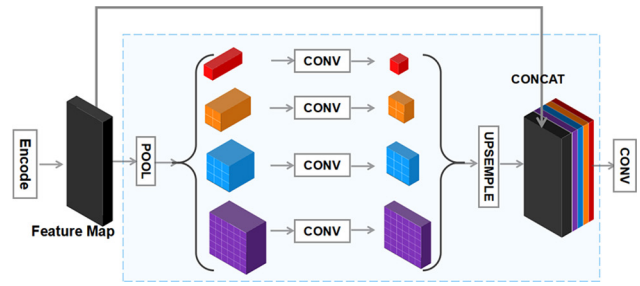

Figure 7. Pyramid pooling module architecture (the blue dotted box).

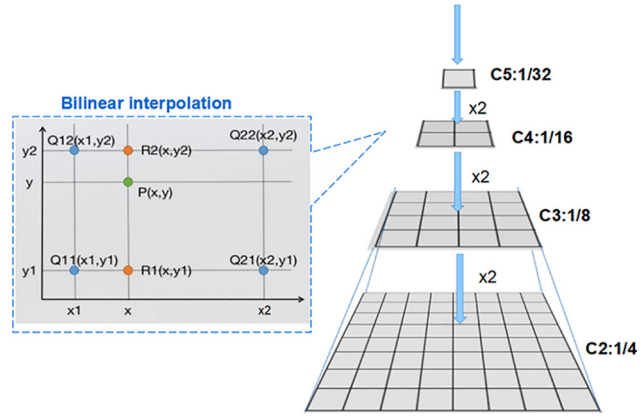

Figure 8. Hierarchical structure of upsampling and bilinear interpolation.

corresponding sampling ratio is marked. The feature map of the semantic segmentation task is a fusion of all the layers of the FPN. There are four decoding blocks in which bilinear interpolation is used for the upsampling. Common upsampling methods in this algorithm include bilinear interpolation and transposed convolution (Figure 8).

Mathematically, bilinear interpolation is the expansion of linear interpolation on a two-dimensional right-angled grid, which is used to interpolate bivariate functions (e.g., x and y). The core concept is to perform linear interpolation along two directions. Suppose we want to obtain the value of the unknown function f at the point $P = (x, y)$ and

we know the function F at $Q_{11} = (x_1, y_1)$, $Q_{12} = (x_1, y_2)$, $Q_{21} = (x_2, y_1)$, and $Q_{22} = (x_2, y_2)$, the value of the four points, the linear interpolation along the x direction would be Equation 2.

$$\begin{aligned} F(R_1) &\approx \frac{x_2 - x}{x_2 - x_1} F(Q_{11}) + \frac{x - x_1}{x_2 - x_1} F(Q_{21}), \qquad \text{where } R_1 = (x, y_1) \\ F(R_2) &\approx \frac{x_2 - x}{x_2 - x_1} F(Q_{12}) + \frac{x - x_1}{x_2 - x_1} F(Q_{22}), \qquad \text{where } R_2 = (x, y_2) \end{aligned} \tag{2}$$

The linear interpolation along the y direction would be Equation 3.

$$F(P) \approx \frac{y_2 - y}{y_2 - y_1} F(R_1) + \frac{y - y_1}{y_2 - y_1} F(R_2) \tag{3}$$

The result $f(x, y)$ is obtained using Equation 4.

$$\begin{aligned} F(x,y) \approx & \frac{F(Q_{11})}{(x_2 - x_1)(y_2 - y_1)}(x_2 - x)(y_2 - y) + \frac{F(Q_{21})}{(x_2 - x_1)(y_2 - y_1)}(x - x_1)(y_2 - y) \\ & + \frac{F(Q_{12})}{(x_2 - x_1)(y_2 - y_1)}(x_2 - x)(y - y_1) + \frac{F(Q_{22})}{(x_2 - x_1)(y_2 - y_1)}(x - x_1)(y - y_1) \end{aligned} \tag{4}$$

Experiments and Results

Experimental Setup

The operating system used in this study is Linux. The experiment has been implemented in Docker (20.10.2) using the PyTorch (1.7.0) framework and Python (3.7.8). The hardware platform is equipped with an Intel Core i7-8700 K graphics processing unit (GPU) and an NVIDIA GeForce GTX 1080Ti processor with 16 GB of RAM. For training, we use the AdamW optimizer; the initial learning rate is 6×10^{-5}, the weight decay is 0.01, and a scheduler with linear learning rate decay and 1500 linear warm-ups have been considered. The model is trained on one GPU; each GPU has two images and is iterated 80 000 times. For enhancement, we use the default settings in mm segmentation with random horizontal flipping, random rescaling within the ratio range of [0.5, 2.0], and random luminosity distortion. The random depth ratio of Swin Transformer is 0.2. In inference, multi-scale testing with training resolutions of [0.5, 0.75, 1.0, 1.25, 1.5, 1.75] is used. When reporting test scores, both training and validation images are used for training, following common practices (Carion *et al.* 2020).

Preprocessing

The first step in our pipeline is image preprocessing. To improve the generalization ability of the model and exploit the potential of the data set, this study performs the following data enhancement operations: (1) random cropping of the original image and label, (2) random flipping of the original image and label, and (3) photometrically distorting the original image, adjusting the brightness, chroma, contrast, and saturation of the image and adding noise.

Evaluation Index

The mean intersection over union (IoU) is a standard indicator for segmentation tasks. IoU quantifies the percentage of overlap between the target and prediction masks. Specifically, it refers to the ratio of the number of pixels in the common area of the target and prediction masks to the total number of pixels in both masks. mIoU denotes the average IoU for each category. Its calculation is divided into two steps. For each category, it calculates the ratio of an intersection to a union. The numerator of this ratio is the number of correct predictions of a specific category, and the denominator is the sum of predictions of the aforementioned category and other categories. We obtain the mean of the calculation results of all the categories.

The experiment includes only one type of building and its background. The IoU calculation method is as follows Equation 5: $i = 1$, and p_{11} represents true positives, i.e., it belongs to category 1. Moreover, the prediction is category 1; $\Sigma_{j=0}^{k} p_{1j}$ represents Class 1 and is predicted to be the number of pixels of other classes (included p_{11}); $\Sigma_{j=0}^{k} p_{j1}$ represents the number of pixels that belong to other classes but are predicted to be class 1 (including p_{11}). In p_{11}, the denominator is calculated twice, therefore, one value of must be subtracted.

$$\text{mIoU} = \frac{1}{k+1} \sum_{i=0}^{k} \frac{P_{ii}}{\sum_{j=0}^{k} P_{ij} + \sum_{j=0}^{k} P_{ji} - P_{ii}} \tag{5}$$

Note: k denotes target classes and 1 denotes background class.

Cross-entropy is defined as a measure of the difference between two probability distributions for a given random variable or a set of events. It is widely used for classification tasks, and as segmentation is a pixel-level classification, it performs very well. In multi-classification tasks, the softmax activation function adds a cross-entropy loss function, which is often used, because cross-entropy describes the difference between the two probability distributions; however, the output of the neural network is a vector and not the form of a probability distribution. Therefore, a softmax activation function is needed to "normalize" a vector into a probability distribution, and then the cross-entropy loss function would be used to calculate loss. As there are positive and negative examples, and the sum of their probabilities is one, there is no need to predict a vector, and only one probability is needed. The loss function is defined as follows:

$$L = -[y \log \hat{y} + (1 - y) \log (1 - \hat{y})] \tag{6}$$

where, L represents the value of the loss function, $\hat{y}$ is the probability that the model predicts that the sample is positive and y is the sample label. If the sample is positive, the value is 1; otherwise, it is 0.

Results

We compared our experimental results with those of several advanced deep learning algorithms based on the data sets U-Net and Baseline net. Based on the comparison between the results of the deep learning model prediction and the Dice coefficient of the ground truth, the Dice values of U-Net and our proposed network were 0.5647 and 0.7950. The details are listed in Table 2.

The Dice coefficient of the model in the test set was stable at 0.795, and mIoU reached 65.9% (Table 4).The accuracy of the model training and test sets was high and close(see Figure 9 and Figure 10), which implies that the model can better identify buildings in the city(see Figure 11), and the overall performance of the training results is good (Table 3).

Table 2. Comparison between intersection over union and loss based on U-Net and ***SWAB-Net*** model verification sets.

Index	U-Net	SWAB-Net
Loss	0.4353	0.2473
IoU	0.2782	0.6034

Table 3. Test results of the proposed network model.

Class	Accuracy	mIoU
Background	36.72	42.30
Building	98.94	95.09

mIoU = average intersection over union (IoU) per category.

Table 4. Global accuracy of ***SWAB-Net*** of the proposed network model.

Scope	mAcc	mIoU	Acc
Global	70.62	65.90	95.23

mAcc = mean accuracy; mIoU = average intersection over union (IoU) per category; Acc = accuracy.

Conclusion

This study proposed a novel semantic segmentation method of the attention module, which is a supervised method known as the shifted window-pyramid self-attention network, ***SWAB-Net***. The receptive field size of the CNN model is fixed so that global semantic information cannot be obtained. Vision Transformer achieves excellent results in image processing, but the model requires a large data set to train. The proposed method overcomes the drawbacks of the limited input size of CNN models and the need for large data sets. The shift window is used to retain information lost due to window slicing. The structure is very simple as it contains only two parts: one is the shift window self-attention backbone network, which is used to learn buildings based on the local features of the images (short-distance context information around pixels). The other part is the feature pyramid module, which is used to obtain global features (long-distance context information of other pixels in the image) and comprehensive features (including color, texture, geometry, and high-level semantic features).

In addition, this study provides a building identification module to assign a unique identification to the same building in each region data set (one image per region is collected every month for two years, a total of 24 images). In this way, the change detection of urban buildings can be realized, and more intuitive data can be provided for the dynamic monitoring, planning and management of the city.

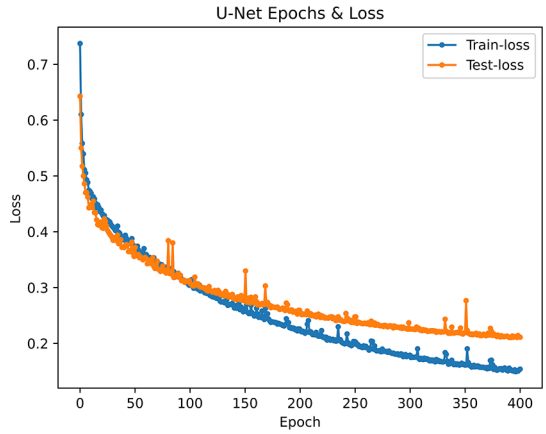

Figure 9. Training loss and test loss of the U-Net.

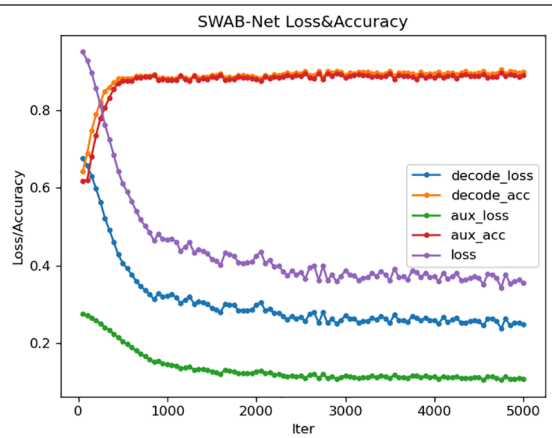

Figure 10. Training loss and accuracy 5000 iter on SWTB-Net.

Acknowledgments

National Natural Science Foundation of China under Grants No. 62090054 and 61934003; Jilin Province Development and Reform Commission No. 2019C054-1 and 2020C019-2; Jilin Scientific and Technological Development Program 20200501007GX; Program for JLU Science and Technology Innovative Research Team (JLUSTIRT, 2021TD-39).

References

Badrinarayanan, V., A. Kendall and R. Cipolla. 2017. Segnet: A deep convolutional encoder-decoder architecture for image segmentation. *IEEE Transactions on Pattern Analysis and Machine Intelligence* 39(12):2481–2495.

Carion, N., F. Massa, G. Synnaeve, N. Usunier, A. Kirillov and S. Zagoruyko. 2020. End-to-end object detection with transformers. Pages 213–229 in *Proceedings of the European Conference on Computer Vision*, held in Glasgow, United Kingdom, 23–28 August 2020.

Çiçek, Ö., A. Abdulkadir, S. S. Lienkamp, T. Brox and O. Ronneberger. 2016. 3D U-Net: Learning dense volumetric segmentation from sparse annotation. Pages 424–432 in *Proceedings of the International Conference on Medical Image Computing and Computer-Assisted Intervention*, held in Athens, Greece, 17–21 October 2016.

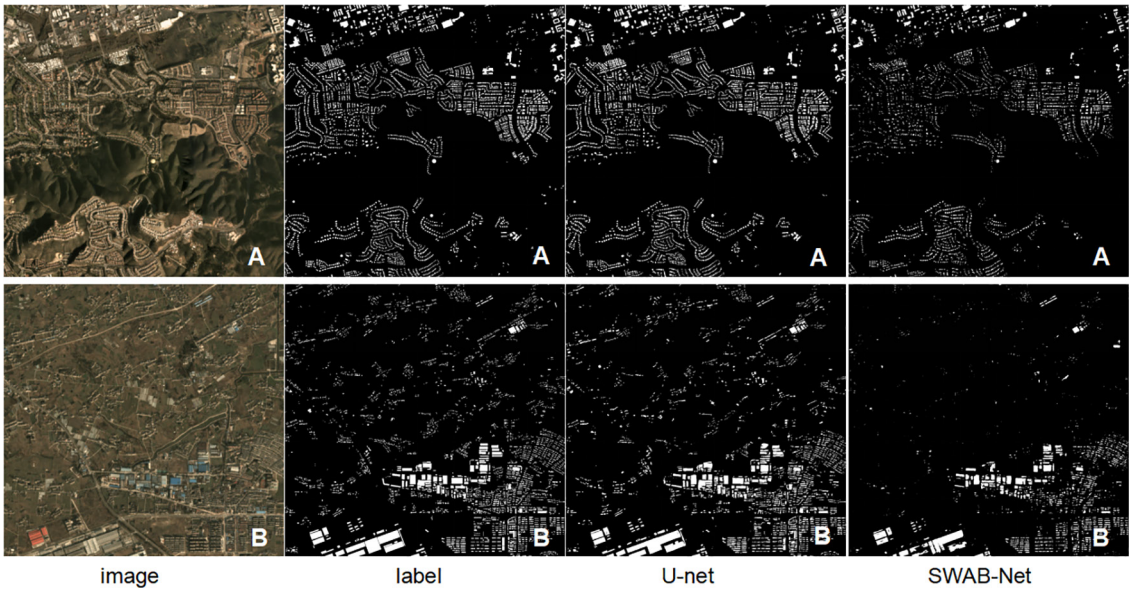

Figure 11. Original images, labels, U-Net, and ***SWAB-Net*** results.

Cheng, G. and J. Han. 2016. A survey on object detection in optical remote sensing images. *ISPRS Journal of Photogrammetry and Remote Sensing* 117:11–28.

Dosovitskiy, A., L. Beyer, A. Kolesnikov, D. Weissenborn, X. Zhai, T. Unterthiner, M. Dehghani, M. Minderer, G. Heigold and S. Gelly. 2020. An image is worth 16x16 words: Transformers for image recognition at scale. *arXiv preprint* arXiv:2010.11929.

Erdem, F. and U. Avdan. 2020. Comparison of different U-net models for building extraction from high-resolution aerial imagery. *International Journal of Environment and Geoinformatics* 7(3):221–227.

He, K., X. Zhang, S. Ren and J. Sun. 2016. Deep residual learning for image recognition. Pages 770–778 in *Proceedings of the IEEE conference on Computer Vision and Pattern Recognition*, held in Las Vegas, NV, 26 June–1 July 2016.

Hui, J., M. Du, X. Ye, Q. Qin and J. Sui. 2018. Effective building extraction from high-resolution remote sensing images with multitask driven deep neural network. *IEEE Geoscience and Remote Sensing Letters* 16(5):786–790.

Krizhevsky, A., I. Sutskever and G. E. Hinton. 2012. Imagenet classification with deep convolutional neural networks. *Advances in Neural Information Processing Systems* 25:1097–1105.

Lin, T.-Y., P. Dollár, R. Girshick, K. He, B. Hariharan and S. Belongie. 2017. Feature pyramid networks for object detection. Pages 2117–2125 in *Proceedings of the IEEE Conference on Computer Vision and Pattern Recognition*, held in Honolulu, HI, 21–26 July, 2017.

Liu, Z., Y. Lin, Y. Cao, H. Hu, Y. Wei, Z. Zhang, S. Lin and B. Guo. 2021. Swin transformer: Hierarchical vision transformer using shifted windows. *arXiv preprint* arXiv:2103.14030.

Long, J., E. Shelhamer and T. Darrell. 2015. Fully convolutional networks for semantic segmentation. Pages 3431–3440 in *Proceedings of the IEEE Conference on Computer Vision and Pattern Recognition*, held in Boston, MA, 7–12 June 2015.

Mahabir, R., A. Croitoru, A. T. Crooks, P. Agouris and A. Stefanidis. 2018. A critical review of high and very high-resolution remote sensing approaches for detecting and mapping slums: Trends, challenges and emerging opportunities. *Urban Science* 2(1):8.

Pan, X., F. Yang, L. Gao, Z. Chen, B. Zhang, H. Fan and J. Ren. 2019. Building extraction from high-resolution aerial imagery using a generative adversarial network with spatial and channel attention mechanisms. *Remote Sensing* 11(8):917.

Pan, Z., J. Xu, Y. Guo, Y. Hu and G. Wang. 2020. Deep learning segmentation and classification for urban village using a worldview satellite image based on U-Net. *Remote Sensing* 12(10):1574.

Ronneberger, O., P. Fischer and T. Brox. 2015. U-net: Convolutional networks for biomedical image segmentation. Pages 234–241 in *Proceedings of the International Conference on Medical Image Computing and Computer-Assisted Intervention*, held in Munich, Germany, 5–9 October 2015.

Shi, W., J. Caballero, F. Huszár, J. Totz, A. P. Aitken, R. Bishop, D. Rueckert and Z. Wang. 2016. Real-time single image and video super-resolution using an efficient sub-pixel convolutional neural network. Pages 1874–1883 in *Proceedings of the IEEE Conference on Computer Vision and Pattern Recognition*, held in Las Vegas, NV, 27–30 June 2015.

Singh, B. and L. S. Davis. 2018. An analysis of scale invariance in object detection snip. Pages 3578–3587 in *Proceedings of the IEEE Conference on Computer Vision and Pattern Recognition*, held in Salt Lake City, UT, 18–22 June 2018.

Soni, A., R. Koner and V.G.K. Villuri. 2020. M-unet: Modified u-net segmentation framework with satellite imagery. Pages 47–59 in *Proceedings of the Global AI Congress 2019*, held in Kolkata, India, 12–14 September 2019.

Vaswani, A., N. Shazeer, N. Parmar, J. Uszkoreit, L. Jones, A. N. Gomez, Ł. Kaiser and I. Polosukhin. 2017. Attention is all you need. Pages 5998–6008 in *Proceedings of the Advances in Neural Information Processing Systems*, held in Long Beach, CA, 4–9 December 2017.

Van Etten, A. and D. Hogan. 2021. The SpaceNet multi-temporal urban development challenge. *arXiv preprint* arXiv:2102.11958.

Van Etten, A., D. Hogan, J. M. Manso, J. Shermeyer, N. Weir and R. Lewis. 2021. The multi-temporal urban development SpaceNet dataset. Pages 6398–6407 in *Proceedings of the IEEE/CVF Conference on Computer Vision and Pattern Recognition*, held online, 19–25 June 2021.

Yi, Y., Z. Zhang, W. Zhang, C. Zhang, W. Li and T. Zhao. 2019. Semantic segmentation of urban buildings from VHR remote sensing imagery using a deep convolutional neural network. *Remote Sensing* 11(15):1774.

Yu, B., L. Yang and F. Chen. 2018. Semantic segmentation for high spatial resolution remote sensing images based on convolution neural network and pyramid pooling module. *IEEE Journal of Selected Topics in Applied Earth Observations and Remote Sensing* 11(9):3252–3261.

Zhang, H., C. Wu, Z. Zhang, Y. Zhu, H. Lin, Z. Zhang, Y. Sun, T. He, J. Mueller and R. Manmatha. 2020. Resnest: Split-attention networks. *arXiv preprint* arXiv:2004.08955.

Zhao, H., J. Shi, X. Qi, X. Wang and J. Jia. 2017. Pyramid scene parsing network. Pages 2881–2890 in *Proceedings of the IEEE Conference on Computer Vision and Pattern Recognition*, held in Honolulu, HI, 22–25 July, 2017.

Zhou, D., G. Wang, G. He, T. Long, R. Yin, Z. Zhang, S. Chen and B. Luo. 2020. Robust building extraction for high spatial resolution remote sensing images with self-attention network. *Sensors* 20(24):7241.

Zhou, Z., M.M.R. Siddiquee, N. Tajbakhsh and J. Liang. 2018. Unet++: A nested U-net architecture for medical image segmentation. *Deep Learning in Medical Image Analysis and Multimodal Learning for Clinical Decision Support*:3–11.

SUSTAININGMEMBERS

ACI USA Inc.
Weston, Florida
https://acicorporation.com/
Member Since: 2/2018

Aerial Services, Inc.
Cedar Falls, Iowa
www.AerialServicesInc.com
Member Since: 5/2001

Airworks Solutions Inc.
Boston, Massachusetts
Member Since: 3/2022

Applanix
Richmond Hill, Ontario, Canada
http://www.applanix.com
Member Since: 7/1997

Ayres Associates
Madison, Wisconsin
www.AyresAssociates.com
Member Since: 1/1953

CT Consultants
Mentor, Ohio
Member Since: 3/2022

Dewberry
Fairfax, Virginia
www.dewberry.com
Member Since: 1/1985

Esri
Redlands, California
www.esri.com
Member Since: 1/1987

GeoCue Group
Madison, Alabama
http://www.geocue.com
Member Since: 10/2003

Geographic Imperatives LLC
Centennial, Colorado
Member Since: 12/2020

GeoWing Mapping, Inc.
Richmond, California
www.geowingmapping.com
Member Since: 12/2016

Halff Associates, Inc.
Richardson, Texas
www.halff.com
Member Since: 8/2021

Keystone Aerial Surveys, Inc.
Philadelphia, Pennsylvania
www.kasurveys.com
Member Since: 1/1985

Kucera International
Willoughby, Ohio
www.kucerainternational.com
Member Since: 1/1992

L3Harris Technologies
Broomfield, Colorado
www.l3harris.com
Member Since: 6/2008

Merrick & Company
Greenwood Village, Colorado
www.merrick.com/gis
Member Since: 4/1995

Nearmap
South Jordan, Utah
www.nearmap.com
Member Since: 6/2023

NV5 Geospatial
Sheboygan Falls, Wisconsin
www.quantumspatial.com
Member Since: 1/1974

Pickett and Associates, Inc.
Bartow, Florida
www.pickettusa.com
Member Since: 4/2007

Riegl USA, Inc.
Orlando, Florida
www.rieglusa.com
Member Since: 11/2004

Robinson Aerial Surveys, Inc.(RAS)
Hackettstown, New Jersey
www.robinsonaerial.com
Member Since: 1/1954

Sanborn Map Company
Colorado Springs, Colorado
www.sanborn.com
Member Since: 10/1984

Surdex Corporation
Chesterfield, Missouri
www.surdex.com
Member Since: 12/2011

Surveying And Mapping, LLC (SAM)
Austin, Texas
www.sam.biz
Member Since: 12/2005

T3 Global Strategies, Inc.
Bridgeville, Pennsylvania
https://t3gs.com/
Member Since: 6/2020

Terra Remote Sensing (USA) Inc.
Bellevue, Washington
www.terraremote.com
Member Since: 11/2016

Towill, Inc.
San Francisco, California
www.towill.com
Member Since: 1/1952

Woolpert LLP
Dayton, Ohio
www.woolpert.com
Member Since: 1/1985

SUSTAININGMEMBER**BENEFITS**

Membership

- ✓ Provides a means for dissemination of new information
- ✓ Encourages an exchange of ideas and communication
- ✓ Offers prime exposure for companies

Benefits of an ASPRS Membership

- Complimentary and discounted Employee Membership*
- E-mail blast to full ASPRS membership*
- Professional Certification Application fee discount for any employee
- Member price for ASPRS publications
- Discount on group registration to ASPRS virtual conferences
- Sustaining Member company listing in ASPRS directory/website
- Hot link to company website from Sustaining Member company listing page on ASPRS website
- Press Release Priority Listing in *PE&RS* Industry News
- Priority publishing of Highlight Articles in *PE&RS* plus, 20% discount off cover fee
- Discount on *PE&RS* advertising
- Exhibit discounts at ASPRS sponsored conferences (exception ASPRS/ILMF)
- Free training webinar registrations per year*
- Discount on additional training webinar registrations for employees
- Discount for each new SMC member brought on board (Discount for first year only)

*quantity depends on membership level

PE&RS 2022 Advertising Rates & Specs

THE MORE YOU ADVERTISE THE MORE YOU SAVE! *PE&RS* offers frequency discounts. Invest in a three-times per year advertising package and receive a 5% discount, six-times per year and receive a 10% discount, 12-times per year and receive a 15% discount off the cost of the package.

	Sustaining Member Exhibiting at a 2022 ASPRS Conference	**Sustaining Member**	**Exhibitor**	**Non Member**
All rates below are for four-color advertisments				
Cover 1	$1,850	$2,000	$2,350	$2,500
In addition to the cover image, the cover sponsor receives a half-page area to include a description of the cover (maximum 500 words). The cover sponsor also has the opportunity to write a highlight article for the journal. Highlight articles are scientific articles designed to appeal to a broad audience and are subject to editorial review before publishing. The cover sponsor fee includes 50 copies of the journal for distribution to their clients. More copies can be ordered at cost.				
Cover 2	$1,500	$1,850	$2,000	$2,350
Cover 3	$1,500	$1,850	$2,000	$2,350
Cover 4	$1,850	$2,000	$2,350	$2,500
Advertorial	1 Complimentary Per Year	1 Complimentary Per Year	$2,150	$2,500
Full Page	$1,000	$1,175	$2,000	$2,350
2 page spread	$1,500	$1,800	$3,200	$3,600
2/3 Page	$1,100	$1,160	$1,450	$1,450
1/2 Page	$900	$960	$1,200	$1,200
1/3 Page	$800	$800	$1,000	$1,000
1/4 Page	$600	$600	$750	$750
1/6 Page	$400	$400	$500	$500
1/8 Page	$200	$200	$250	$250
Other Advertising Opportunities (see page 5 for full descriptions)				
Employment Promotion	$500 (30 day web + 1 email) $300 (30 day web)	$500 (30 day web + 1 email) $300 (30 day web)	$500 (30 day web + 1 email) $300 (30 day web)	$500 (30 day web + 1 email) $300 (30 day web)
Dedicated Content Email blast	$3000	$3000	$3000	$3000
Newsletter Display Advertising	1 Complimentary Per Year	1 Complimentary Per Year	$500	$500
PE&RS Digital Edition Announcement E-Mail	$1000	$1000	$1000	$1000

A 15% commission is allowed to recognized advertising agencies

Ad Size	Width	Height
Cover (bleed only)	8.625"	11.25"
Full Page (bleed)	8.625"	11.25"
Full Page (trim)	8.375"	10.875"
2/3 Page Horizontal	7.125"	6.25"
2/3 Page Vertical	4.58"	9.625"
1/2 Page Horizontal	7.125"	4.6875"
1/2 Page Vertical	3.4375"	9.625"
1/3 Page Horizontal	7.125"	3.125"
1/3 Page Vertical	2.29"	9.625"
1/4 Page Horizontal	7.125"	2.34"
1/4 Page Vertical	3.4375"	4.6875"
1/8 Page Horizontal	7.125"	1.17"
1/8 Page Vertical	1.71875"	4.6875"

- Publication Size: 8.375" × 10.875" (W x H)
- Live area: 1/2" from gutter and 3/8" from all other edges
- No partial page bleeds.
- Publication Style: Perfect bound
- Printing Method: Web offset press
- Software Used: PC InDesign
- Supported formats:
  TIFF, EPS, BMP, JPEG, PDF, PNG
  PC InDesign, Illustrator, and Photoshop

ASPRS ADVERTISING & EXHIBIT SALES:

Bill Spilman
ASPRS Advertising, Exhibit Sales & Sponsorships
320 W. Chestnut St., P.O. Box 399
Oneida, IL 61467
(877) 878-3260 toll-free
(309) 483-6467 direct
(309) 483-2371 fax
bill@innovativemediasolutions.com

For more information, contact Bill Spilman at bill@innovativemediasolutions.com | (877) 878-3260 toll-free | (309) 483-6467 direct | (309) 483-2371 fax

Special Advertising Opportunities

FRONT COVER SPONSORSHIP

A *PE&RS* cover sponsorship is a unique opportunity to capture the undivided attention of your target market through three premium points of contact.

1— *PE&RS* FRONT COVER

(Only twelve available, first-come, first-served)
PE&RS is world-renowned for the outstanding imagery displayed monthly on its front cover—and readers have told us they eagerly anticipate every issue. This is a premium opportunity for any company, government agency, university or non-profit organization to provide a strong image that demonstrates their expertise in the geospatial information industry.

2— FREE ACCOMPANYING "HIGHLIGHT" ARTICLE

A detailed article to enhance your cover image is welcome but not a condition of placing an image. Many readers have asked for more information about the covers and your article is a highly visible way to tell your story in more depth for an audience keenly interested in your products and services. No article is guaranteed publication, as it must pass ASPRS editorial review. For more information, contact Rae Kelley at rkelley@asprs.org.

3— FREE TABLE OF CONTENTS COVER DESCRIPTION

Use this highly visible position to showcase your organization by featuring highlights of the technology used in capturing the front cover imagery. Limit 200-word description.

Terms: Fifty percent nonrefundable deposit with space reservation and payment of balance on or before materials closing deadline.

Cover Specifications: Bleed size: 8 5/8" × 11 1/4", Trim: 8 3/8" × 10 7/8"

PRICING

	Sustaining Member Exhibiting at a 2022 ASPRS Conference	**Sustaining Member**	**Exhibitor**	**Non Member**
Cover 1	$1,850	$2,000	$2,350	$2,500

Belly Bands, Inserts, Outserts & More!

Make your material the first impression readers have when they get their copy of *PE&RS*. Contact Bill Spilman at bill@innovativemediasolutions.com

VENDOR SEMINARS

ASPRS Sustaining Members now have the opportunity to hold a 1-hour informational session as a Virtual Vendor Seminar that will be free to all ASPRS Members wishing to attend. There will be one opportunity per month to reach out to all ASPRS Members with a demonstration of a new product, service, or other information. ASPRS will promote the Seminar through a blast email to all members, a notice on the ASPRS web site home page, and ads in the print and digital editions of *PE&RS*.

The Virtual Seminar will be hosted by ASPRS through its Zoom capability and has the capacity to accommodate 500 attendees.

Vendor Seminars	
Fee	$2,500 (no discounts)

DIGITAL ADVERTISING OPPORTUNITIES

EMPLOYMENT PROMOTION

When you need to fill a position right away, use this direct, right-to-the-desktop approach to announce your employment opportunity. The employment opportunity will be sent once to all ASPRS members in our regular Wednesday email newsletter to members, and will be posted on the ASPRS Web site for one month. This type of advertising gets results when you provide a web link with your text.

Employment Opportunity	**Net Rate**
30-Day Web + 1 email	$500/opportunity
Web-only (no email)	$300/opportunity

Do you have multiple vacancies that need to be filled? Contact us for pricing details for multiple listings.

NEWSLETTER DISPLAY ADVERTISING

Your vertical ad will show up in the right hand column of our weekly newsletter, which is sent to more than 3,000 people, including our membership and interested parties. **Open Rate: 32.9%**

Newsletter vertical banner ad	**Net Rate**
180 pixels x 240 pixels max	$500/opportunity

DEDICATED CONTENT EMAIL BLAST

Send a dedicated email blast to the ASPRS email list. Advertiser supplies HTML (including images). Lead time: 14 days.

Materials	**Net Rate**
Advertiser supplies HTML, including images.	$3000/ opportunity

PE&RS Digital Edition

Digital Edition Announcement E-Mail: 5,800+

PE&RS is available online in both a public version that is available to anyone but does not include the peer-reviewed articles, and a full version that is available to ASPRS members only upon login.

The enhanced version of *PE&RS* contains hot links for all ASPRS Sustaining Member Companies, as well as hot links on advertisements, ASPRS Who's Who, and internet references.

Become a sponsor today!

The e-mail blast sponsorship opportunity includes a **180 x 240 pixel ad** in the email announcement that goes out to our membership announcing the availability of the electronic issue.

Digital Edition Opportunities	**Net Rate**
E-mail Blast Sponsorship*	$1,000

For more information, contact Bill Spilman at bill@innovativemediasolutions.com | (877) 878-3260 toll-free | (309) 483-6467 direct | (309) 483-2371 fax

The 4th Edition of the *Manual of Remote Sensing!*

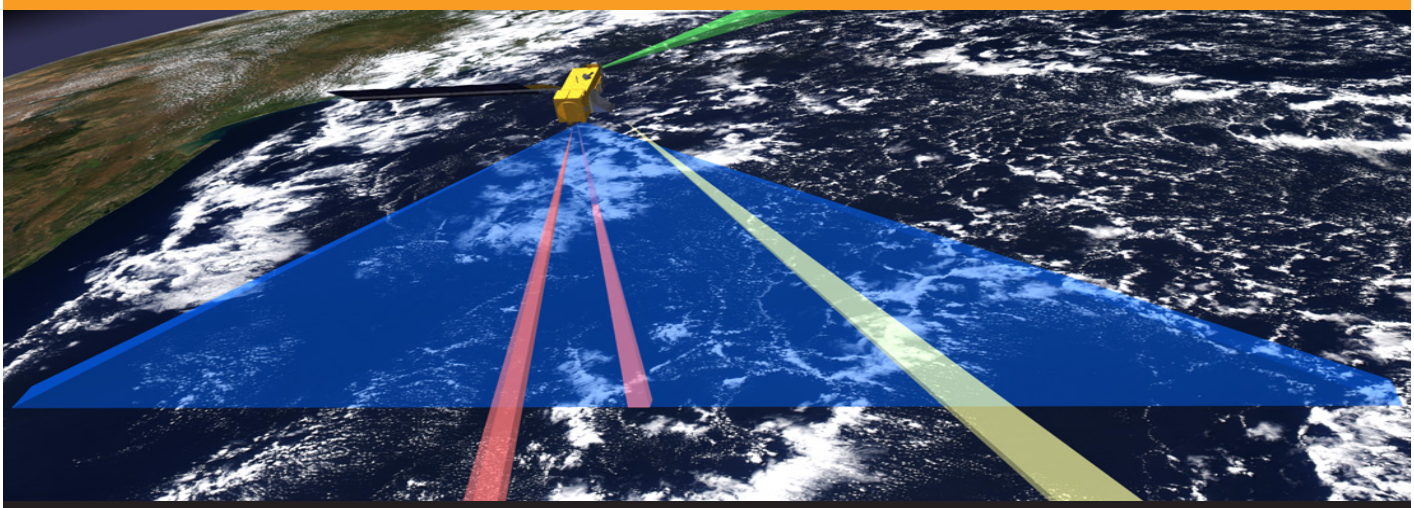

MANUAL OF REMOTE SENSING

Fourth Edition

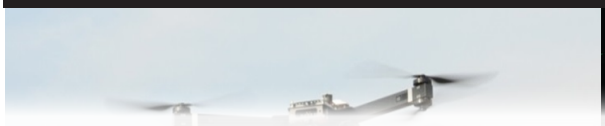

The *Manual of Remote Sensing, 4th Ed.* (MRS-4) is an "enhanced" electronic publication available online from ASPRS. This edition expands its scope from previous editions, focusing on new and updated material since the turn of the 21st Century. Stanley Morain (Editor-in-Chief), and co-editors Michael Renslow and Amelia Budge have compiled material provided by numerous contributors who are experts in various aspects of remote sensing technologies, data preservation practices, data access mechanisms, data processing and modeling techniques, societal benefits, and legal aspects such as space policies and space law. These topics are organized into nine chapters. MRS4 is unique from previous editions in that it is a "living" document that can be updated easily in years to come as new technologies and practices evolve. It also is designed to include animated illustrations and videos to further enhance the reader's experience.

MRS-4 is available to ASPRS Members as a member benefit or can be purchased by non-members. To access MRS-4, visit https://my.asprs.org/mrs4.

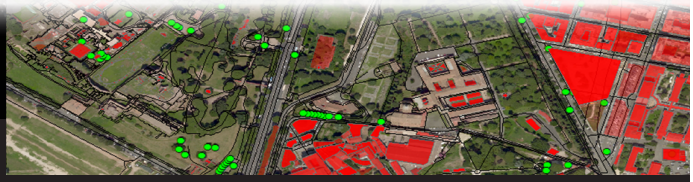

edited by: Stanley A. Morain,
Michael S. Renslow and Amelia M. Budge